NEW MEXICO DEPARTMENT OF TRANSPORTATION

RESEARCH BUREAU

Innovation in Transportation

Study and Evaluation of Material Response in Hot Mix Asphalt based on Field Instrumentation (Phase II)

Final Report

Prepared by:
University of New Mexico
Department of Civil Engineering
Albuquerque, NM 87131

Prepared for:
New Mexico Department of Transportation
Research Bureau
7500B Pan American Freeway NE
Albuquerque, NM 87109

In Cooperation with:
The US Department of Transportation
Federal Highway Administration

Report NM11MSC-03

JUNE 2019

USDOT FHWA SUMMARY PAGE

1. Report No. NM11MSC-03	2. Recipient's Catalog No.
3. Title and Subtitle Study and Evaluation of Material Response in Hot Mix Asphalt based on Field Instrumentation (Phase II)	4. Report Date June 2019
5. Author(s): Rafiqul A. Tarefder and Zafrul H Khan	6. Performing Organization Report No. NM11MSC-03
7. Performing Organization Name and Address University of New Mexico Department of Civil Engineering MSC01 1070 1 University of New Mexico Albuquerque, NM 87131	8. Performing Organization Code 456A 9. Contract/Grant No. 456-470
10. Sponsoring Agency Name and Address Research Bureau New Mexico Department of Transportation (NMDOT) 7500B Pan American Freeway PO Box 94690 Albuquerque, NM 87199-4690	11. Type of Report and Period Covered Final Report June 2015 – June 2019 12. Sponsoring Agency Code NMDOT
13. Supplementary Notes The research project is funded by the NMDOT in cooperation with the FHWA	

14. Abstract

This report presents the results of a research study conducted to observe the variations in mechanistic responses, e.g. stress-strain, of a flexible pavement through embedded sensors. The research program was divided into two phases. During the first phase, an instrumentation section was constructed at I-40 near Albuquerque, New Mexico with an array of 32 sensors. Data collection and analysis were continued until the end of the second phase. Pavement responses were collected in various climatic conditions under actual traffic loads and routine Falling Weight Deflectometer (FWD) test loads. Field distress data were collected at regular intervals. Field cored Asphalt Concrete (AC) samples were also collected for laboratory testing and comparing with the field sensor data. From the results, it is observed that pavement responses initially increased immediately after the construction, but they started to decrease with time. AC backcalculated modulus is also observed to be decreasing with time. The reason for this decrease is damage. By combining sensor data with FWD modulus and Weigh-In-Motion (WIM) data, damage in pavement layers were quantified. Pavement response frequency from sensor data under traffic loadings is compared with the AASHTOWare ME predicted loading frequency. It is observed that the AASHTOWare ME always overpredicts loading frequency, which in turn overpredicts the dynamic modulus value of the AC layer; leading to over design of the AC layer. A good agreement is observed between the viscoelastic parameters of the AC layer obtained directly from field sensor data and laboratory tested data. No major distresses, such as cracking and rutting, were observed in the driving lane but delamination between the AC lifts is observed. Thus, to have a meaningful calibration of the distress models and to study the pavement performance variations under various distresses, a continuation of the data collection is recommended.

15. Key Words Hot-Mix Asphalt, Stress, Strain, Temperature, Frequency, Cracking		16. Distribution Statement Available from NMDOT Research Bureau	
17. Security Classi. of the Report None	18. Security Classi. of this page None	19. Number of Pages 145	20. Price N/A

THIS PAGE LEFT BLANK INTENTIONALLY

PROJECT NO. NM11MSC-03

Study and Evaluation of Material Response in Hot Mix Asphalt based on Field Instrumentation (Phase II)

FINAL REPORT

June 2015 – June 2019

A Report on Research Sponsored by:

Research Bureau
New Mexico Department of Transportation
7500B Pan American Freeway NE,
PO Box 94690
Albuquerque, NM 87199-4690
(505)-841-9145
Research.bureau@state.nm.us
http://NMDOTRearch.com

Prepared by:
Rafiqul A. Tarefder and Zafrul H Khan
Department of Civil Engineering
University of New Mexico
MSC01 1070, 1 University of New Mexico
Albuquerque, NM 87131

PREFACE

This report describes the pavement responses obtained through an instrumented pavement section on Interstate 40 (I-40). It presents the stress-strain under real time traffic conditions, stiffness, moisture, and temperature variations at different depths of pavement at the instrumentation section. It discusses the traffic and performances data collected so far.

NOTICE

The United States Government and the State of New Mexico do not endorse products or manufacturers. Trade or manufactures' names appear herein solely because they are considered essential to the object of this report. This information is available in alternative accessible formats. To obtain an alternative format, contact the NMDOT Research Bureau, 7500B Pan American Freeway NE, PO Box 94690, Albuquerque, NM 87199-4690, (505) 841-9145.

DISCLAIMER

This report presents the results of research conducted by the authors and does not necessarily reflect the views of the New Mexico Department of Transportation. This report does not constitute a standard or specification.

ABSTRACT

This report presents the results of a research study conducted to observe the variations in mechanistic responses, e.g. stress-strain, of a flexible pavement through embedded sensors. The research program was divided into two phases. During the first phase, an instrumentation section was constructed at I-40 near Albuquerque, New Mexico with an array of 32 sensors. Data collection and analysis were continued until the end of the second phase. Pavement responses were collected in various climatic conditions under actual traffic loads and routine Falling Weight Deflectometer (FWD) test loads. Field distress data were collected at regular intervals. Field cored Asphalt Concrete (AC) samples were also collected for laboratory testing and comparing with the field sensor data. From the results, it is observed that pavement responses initially increased immediately after the construction, but they started to decrease with time. AC backcalculated modulus is also observed to be decreasing with time. The reason for this decrease is damage. By combining sensor data with FWD modulus and Weigh-In-Motion (WIM) data, damage in pavement layers were quantified. Pavement response frequency from sensor data under traffic loadings is compared with the AASHTOWare ME predicted loading frequency. It is observed that the AASHTOWare ME always overpredicts loading frequency, which in turn overpredicts the dynamic modulus value of the AC layer; leading to over design of the AC layer. A good agreement is observed between the viscoelastic parameters of the AC layer obtained directly from field sensor data and laboratory tested data. No major distresses, such as cracking and rutting, were observed in the driving lane but delamination between the AC lifts is observed. Thus, to have a meaningful calibration of the distress models and to study the pavement performance variations under various distresses, a continuation of the data collection is recommended.

ACKNOWLEDGEMENTS

This project was funded by the New Mexico Department of Transportation's Research Bureau. The University of New Mexico's (UNM) research team would like to express their sincere gratitude and appreciation to Mr. Jeff Mann, Pavement Management and Design Bureau Chief, NMDOT, for being the advocate of this project and for his regular support, sponsorship, long-term vision, and suggestions. The UNM research team appreciates the valuable service and time of the Project Manager, Mr. Virgil Valdez. Mr. Valdez's kind help in field work, material collection, constant communication with traffic control, District 3, exploration team, panel members, and so on, were crucial for this project and are greatly appreciated.

The UNM research team would also like to express their sincere gratitude and appreciation to Mr. James Gallegos, Materials Bureau Chief, NMDOT for his generous support, ideas, valuable time, and suggestions. The authors also express their special gratitude and appreciation to Ms. Kelly Montoya, Mr. Ben Martinez and everyone in the NMDOT field exploration team for their constant support and help during testing and sample collection.

The UNM research team would like to thank the other Project Technical panel members for their valuable suggestions during the quarterly meetings. Thanks go to Mr. Ray Chavez with NMDOT research Bureau, Mr. Jeremy Rocha of Materials Bureau, and Mr. Parveez Anwar former NMDOT's State Asphalt Engineer for their assistance and suggestions for this project.

The authors would like to thank several members and personnel at the NMDOT's District 3 and UNM for their support.

TABLE OF CONTENTS

LIST OF FIGURES

LIST OF TABLES

THIS PAGE LEFT BLANK INTENTIONALLY

INTRODUCTION

RESEARCH NEED AND SIGNIFICANCE

One of the most important assets of the NMDOT is its pavement system. A major portion of this investment goes to maintain and rehabilitation of the old pavements. Among different pavement types, asphalt pavement is most widely used in NM. Flexible or Asphalt Concrete (AC) pavement gets deteriorated over time mainly due to environmental and traffic loadings. To design a better pavement, the reasons for deterioration must be understood and considered during the design phase and, also, into the maintenance schedule. However, understanding the combined effect of pavement damage due to environment and traffic loadings is not a trivial task. It is extremely difficult, if not impossible, to accurately represent the effects of these two factors on pavement performance through laboratory testing alone. For example, the effect of a single factor among these two can be well studied in the controlled environment of a laboratory, such as the effect of aging on pavement damage. However, in the field, damage due to aging does not take place alone; along with aging, there are damages due to moisture, freeze-thaw cycle and continuous repeated movement of traffic. A conversation or calibration factor is generally used to convert between the laboratory and field observed values. Thus, it is important to characterize the pavement performance, consequently, the materials directly at the field and from the field itself. Non-destructive testing can be used in this regard, but the non-destructive test alone only provides a partial understanding. For a comprehensive evaluation of the complex phenomenon of pavement damage in the field, both instrumented pavement section and non-destructive test such as Falling Weight Deflectometer (FWD) are essential.

Furthermore, pavements were previously designed using the empirical method, i.e., based on the engineering judgment. Now, pavement design has shifted more toward a mechanistic based approach. Today, most of the state transportation agencies across the United States use AASHTOWare Mechanistic-Empirical (ME) design guide for pavement design. It is a mechanistic-empirical design approach where the pavement responses are measured using classical mechanics and distress are predicted using the empirical equations. For proper implementation of the AASHTOWare ME across New Mexico, it is important to study the pavement responses obtained directly from the field and ME software, and make appropriate adjustments in the global distress models through calibration study. Thus, field instrumentation is essential in this regard.

OBJECTIVES

The main goal of this study is to evaluate the pavement performance over time under traffic and environmental conditions in New Mexico. Pavement theoretical models are used to evaluate the pavement performances such as the stresses, strains, and deflections generated by different types of loadings, and subsequently used to calculate distresses. However, it is very difficult to accurately develop a theoretical pavement response model without any prior knowledge of the pavement performance under local traffic and environment conditions. It creates a circular problem: without pavement performance information, an accurate pavement theoretical model cannot be developed, and subsequently, an accurate theoretical model is required for determination

of pavement performance data, which in turn is required for distress evaluation. Thus, this study aims to find out how the pavement performance such as stress, strain, and deflection changes over time under traffic and environmental conditions in New Mexico. To facilitate this, pavement performance data were collected from the instrumented pavement section on Interstate 40 (I-40) near Albuquerque, New Mexico. Specific objectives can be found below:

1) Collect stress-strain data from embedded sensors at different pavement layers under traffic and FWD test loads.
2) Perform FWD test on the instrumented pavement section at designated locations to obtain layer modulus and observe the variations over time.
3) Document different distress types, such as thermal and fatigue cracking and rutting observed in the instrumented section over time.
4) Collect and analyze the environmental data, such as temperature and moisture inside the pavement layers.
5) Collect and analyze the Weigh-In-Motion (WIM) data to determine the traffic pattern and distribution factors required for the ME design analysis.
6) Review the best practices for enhancing the ME's Integrated Climate Model (ICM) and determine the strategic locations for new weather stations across New Mexico.
7) Collect materials from the instrumented pavement section at regular interval for laboratory testing and comparison with the field embedded sensor obtained values.

REPORT ORGANIZATIONS

This report is comprised of five sections. They can be summarized below:

- Section 1 Introduction: Describes the research need and objectives of this research.
- Section 2 Literature Review: This section briefly describes the best practices for enhancing ME's ICM model and the theories related to the analysis of the instrumentation data.
- Section 3 Field Characterization of Materials: This section characterizes the pavement materials based on field sensor obtained data. This section describes the variations of stresses and strains in pavement layers and its implications.
- Section 4 Laboratory Characterization of Materials: This section characterizes the pavement based on the samples collected from the instrumentation section.
- Section 5 Conclusions and Recommendations: This section concludes with the findings of the report and provides recommendations for future studies.

THIS PAGE LEFT BLANK INTENTIONALLY

LITERATURE REVIEW

Although most of the literature review for the instrumentation project was conducted in Phase I of the project, but the University of New Mexico (UNM) research team has performed a comprehensive review of the state-of-the-art research topics to develop a sound understanding relevant to the processing and analyzing of the field instrumentation and non-destructive test data.

REVIEW ON BEST PRACTICES FOR ENHANCING ME'S ICM DATA

Performances of both flexible and rigid pavement are susceptible to temperature and moisture content of the pavement layers. Temperature has a significant effect on the stiffness of pavement materials as well as stresses developed in pavement layers. Strength of pavement drops significantly due to the freeze-thaw effect due to the formation of ice lenses at a temperature below the freezing temperature. Moisture content affects the resilient moduli of unbound layers which eventually affects the structural integrity of bound layers *(1)*. The pavement ME design adopted a climatic model, named ICM, to determine depth-temperature profile, and modulus adjustment factors due to moisture as well as climatic factors such as air temperature, percentage of sunshine, precipitation, wind speed, relative humidity and location of groundwater table *(2, 3)*.

The ICM is a sophisticated climatic model which accounts for the change in temperature and moisture over the pavement service life. It also predicts the temperature-modulus adjustment factors, pore-water pressure, moisture content, freeze-thaw depth, and drainage performance for the pavement layers. The ICM has three major components and these are:

- The Climatic-Materials-Structural Model (CMS Model)
- The Frost Heave and Thaw Settlement Model (CRREL Model)
- The Infiltration and Drainage Model (ID Model)

CMS Model

The CMS model was developed at the University of Illinois in 1985. It predicts the temperatures throughout the pavement layers from atmospheric condition using one-dimensional, forward finite difference heat transfer analysis *(4)*. It also determines the frost penetration. The CMS model is illustrated in Figure 1. The energy balance at the pavement surface used in this model can be described as:

$$Q_i - Q_r + Q_a - Q_e \pm Q_c \pm Q_h \pm Q_g = 0 \quad (1)$$

where $Q_i =$ incoming short wave radiation, $Q_r =$ reflected short wave radiation, $Q_a =$ incoming longwave radiation, $Q_e =$ outgoing shortwave radiation, $Q_c =$ convective heat transfer, $Q_h =$ effects of transpiration, condensation, evaporation and sublimation, and $Q_g =$ energy absorbed by the ground. Now, the net all-wave length radiation at the surface (Q_n) is:

$$Q_n = Q_s - Q_l \quad (2)$$

where Q_s = net short wave radiation, and Q_l = net longwave radiation. Again,

$$Q_s = Q_i - Q_r \tag{3}$$

$$Q_l = Q_a - Q_e \tag{4}$$

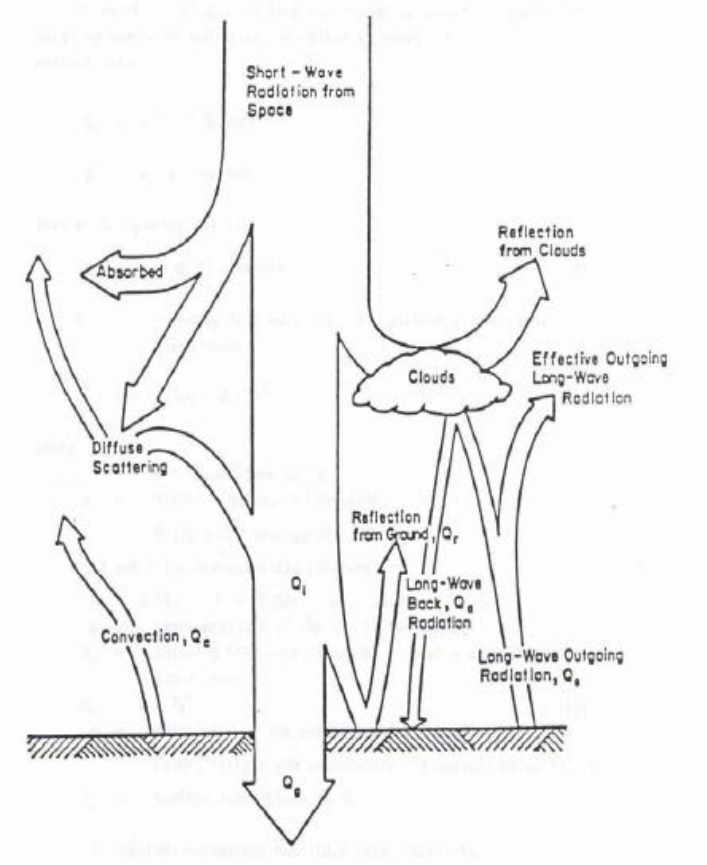

FIGURE 1 Heat transfer process between pavement surface and air *(5)*

Alternatively, Q_n can be determined from the surface shortwave absorptivity, and percent cloud cover as follows:

$$Q_s = a_s R^* \left(A + B \frac{S_c}{100} \right) \tag{5}$$

where a_s = surface shortwave absorptivity of pavement surface, R^* = extraterrestrial radiation incident on a horizontal surface at the outer atmosphere which depends on the latitude of the site and the solar declination of the sun, A, B = constants accounting for diffuse scattering and

adsorption by the atmosphere (= 0.202 and 0.539 respectively), and S_c = percentage of sunshine which accounts for the influence of cloud cover. Now,

$$Q_a = Q_z\left(1-\frac{NW}{100}\right) \tag{6}$$

$$Q_e = Q_x\left(1-\frac{NW}{100}\right) \tag{7}$$

Therefore, Eq. (4) can be modified as follows:

$$Q_l = \left(Q_z - Q_x\right)\left(1-\frac{NW}{100}\right) \tag{8}$$

where N = cloud base factor (0.9 to 0.8 for cloud heights of 1000 ft to 6000 ft), and W = average cloud cover during day or night. The incoming longwave radiation without a correction for cloud cover (Q_z) is:

$$Q_z = a_{sb}T_{air}\left(G-\frac{J}{10^{\rho p}}\right) \tag{9}$$

where σ_{sb} = Stefan-Boltzmann constant, 0.172 x 10^{-8} Btu/(hr-ft^2-^{0}R^4), T_{air} = air temperature (^{0}R), and p = vapor pressure of the air. Now, the outgoing longwave radiation without a correction for cloud cover (Q_x) is:

$$Q_x = \sigma_{sb}\varepsilon T_s^4 \tag{10}$$

where ε = emissivity of the pavement which depends on the pavement color, texture and temperature, and T_s = surface temperature (^{0}R).

The rate of heat transfer by convection (Q_c) is determined as follows:

$$Q_c = H\left(T_{air} - T_s\right) \tag{11}$$

where H = convection heat transfer coefficient $= 112.93\left[0.001T_m^{0.3}U^{0.7} + 0.00097\left(T_s - T_{air}\right)^{0.3}\right]$, T_s = surface temperature (^{0}C), T_{air} = air temperature (^{0}C), T_m = Average of surface and air temperature (^{0}K), and U = average daily wind speed (m/s).

Finally, the above calculations determine the surface temperature and thus, control the temperature throughout the underlying materials. The depth of frost penetration is established by comparing the computed temperatures with the freezing temperatures of the soil. The depth of frost

penetration is identified as the position of the 30 ^{0}F isotherm. Finite difference approach is used to determine the nodal temperature based on the following relationship:

$$\frac{dT}{dz} = \frac{1}{\alpha}\frac{d^2T}{dz^2} \tag{12}$$

where $T =$ temperature at depth 'z', $\alpha =$ thermal diffusivity $\left(= \frac{KQ}{\gamma_d} \right)$, $K =$ thermal conductivity, $Q =$ heat capacity, and $\gamma_d =$ dry unit weight of soil.

CRREL Model

The CRREL model was developed at the United States Army Cold Regions Research and Engineering Laboratory in 1986. Unlike the other models, the CRREL model uses a finite element solution to the governing equations for water and temperature flow to calculate the changes in temperature and water content with time and space. The governing equation for water flow in unsaturated subgrade soils is referred to as the Richards equation, while the governing equation for temperature flow in soils is referred to as the Fourier equation. Based on this mathematical model that couples heat and moisture flow in the soil the volumetric ice content and volumetric unfrozen water content are computed. Then comparing the sum of the ice and water volumes with the porosity of the soil, the model can compute the frost heave or thaw settlement. The CRREL model uses the temperature profiles in a pavement system established by the CMS model as input.

The governing heat and soil-water flow equations can be written in Eq. (13):

$$\frac{d}{dz}\left(k_1 \frac{dT}{dz}\right) - \frac{dT}{dz}\left(k_2 T\right) - k_3 \frac{dT}{dt} = 0 \tag{13}$$

where $k_1 =$ thermal conductivity, $k_2 =$ heat capacity of water multiplied by velocity, $k_3 =$ heat capacity of soil, and $T =$ temperature.

ID Model

The ID model was developed at Texas A&M University by Liu and Lytton in 1985 *(6)*. There are three major tasks in the ID model and these are the drainage analysis, pavement evaluation analysis and infiltration analysis. It uses an analytical relationship to calculate the degree of drainage (via lateral drainage) versus time of an initially saturated granular base course layer overlying a permeable or impermeable subgrade. The geometry of this layer can be input by the user. This analysis assumes that the base course is a free draining material, and that water cannot enter the subgrade. Further, this simplified analysis does not account for drainage or hydraulic barriers in the pavement system.

There are two options for calculating the degree of saturation in the base course: Ridgeway's model, and Dempsey-Robnett model *(7)*. Both of these programs use historic weather records

including precipitation and duration. The Ridgeway's model is activated in the program by assigning a number for linear cracks in a pavement. This model indicated that cracks and joints of pavements are the main path for free water. In addition, rainfall duration is more important than rainfall intensity in determining amount of free water that will enter the pavement structure. The Ridgeway's model assumes water to infiltrate into the base course layer at a rate of 0.1 cft/hr (asphalt pavement), and 0.03 cft/hr (Portland Cement Concrete (PCC) pavement). This model calculates the amount of water in the base course based on the volume of rainfall entering the base layer.

The Dempsey-Robnett model does not require a length of cracks in order to estimate the increase in the volume of water in the base layer. In order to use this model, the user must input '0' for length of cracks on a pavement. Dempsey and Robnett (1979) developed empirical equations by measuring the volume of flow through drainage layers for rainfall events having a different intensity and duration. The volume of water entering the base course is estimated using this model as shown in Eq. (14):

$$R = 0.48PV + 0.32 \tag{14}$$

where $R =$ outflow volume in inches, and $PV =$ precipitation volume in inches. The amount of drainage in the base course is calculated from the degree of saturation. The degree of saturation is represented as follows:

$$S = 1 - PD \times U \tag{15}$$

where $S =$ degree of saturation, $PD =$ index representing the ability of a certain base course to drain water, and $U =$ decrease in the degree of saturation due to drainage. The ID model uses the information in Table 1 to estimate the value of *PD* for a given soil.

TABLE 1 *PD* value for different types of soil

Amount of Fines	< 2.5%			5%			10%		
Type	Inert filler	Silt	Clay	Inert filler	Silt	Clay	Inert filler	Silt	Clay
Gravel	70	60	40	60	40	20	40	30	10
Sand	57	50	35	50	35	15	25	18	8

Unfortunately, this model does not account for how the pavement becomes fully saturated in the first place, so it may be an over-conservative situation to use in design. Although it may be a simple conceptual model useful for preliminary design, the ID model does not permit simulation of the actual hydraulic interaction between a pavement system and the atmosphere.

There are two other models which are briefly discussed below:

Soil Water Characteristic Curve

The ICM used Soil Water Characteristic Curve (SWCC) model developed by Fredlund and Xing (1994). It needs the percentage retained on #200 sieve (P_{200}) and (D_{60}) will be found. Plasticity Index (PI) can be determined from the grain size distribution based on the Atterberg limit test. Using these values specific gravity (G_s), optimum gravimetric moisture content (ω_{opt}), maximum dry unit weight $(\gamma_{d,\max})$, dry unit weight (γ_d), optimum degree of saturation (S_{opt}), optimum volumetric water content (θ_{opt}), saturated volumetric water content (θ_{sat}) can be calculated by following Eq. (16):

$$
\begin{aligned}
& G_s = 0.041\left(P_{200} \times PI\right)^{0.29} + 2.65 \\
& \text{If } \left(P_{200} \times PI\right) > 0, \qquad \omega_{opt} = 1.3\left(P_{200} \times PI\right)^{0.73} + 11 \\
& \text{If } \left(P_{200} \times PI\right) = 0, \qquad \omega_{opt} = 8.6452 D_{60}^{-0.1038} \\
& \gamma_{d,\max} = \frac{G_s \gamma_w}{1 + \frac{\omega_{opt} G_s}{S_{opt}}} \\
& \theta_{opt} = \frac{\omega_{opt} \gamma_{d,\max}}{\gamma_w} \\
& S_{opt} = \frac{\theta_{opt}}{1 - \frac{\gamma_{d,\max}}{G_s \gamma_w}} \\
& \theta_{sat} = \frac{\theta_{opt}}{S_{opt}}
\end{aligned}
\tag{16}
$$

Then, the SWCC model regression parameters (a_f, b_f, c_f, h_r) can be calculated from following Eq. (17).

$$
\text{If } \left(P_{200} \times PI\right) > 0 \tag{17}
$$

$$a_f = \frac{0.00364(P_{200} \times PI)^{3.35} + 4(P_{200} \times PI) + 11}{6.895}$$

$$\frac{b_f}{c_f} = -2.313(P_{200} \times PI)^{0.14} + 5$$

$$c_f = 0.0514(P_{200} \times PI)^{0.14} + 5$$

$$\frac{h_r}{a_f} = 32.44e^{0.0186(P_{200} \times PI)}$$

If $(P_{200} \times PI) = 0$, $a_f = \frac{0.8627 D_{60}^{-0.751}}{6.895}, b_f = 7.5$

$$c_f = 0.1772 \ln(D_{60}) + 0.7734$$

$$\frac{h_r}{a_f} = \frac{1}{D_{60} + 9.7e^{-4}}$$

Finally, the volumetric water content (θ_v) and suction $(C(h))$ can be determined as follows:

$$\theta_v = \frac{C(h)\theta_{sat}}{\left[\ln\left\{e + \left(\frac{h_r}{a_f}\right)^{b_f}\right\}\right]^{c_f}} \tag{18}$$

$$C(h) = 1 - \frac{\ln\left(1 + \frac{h}{h_r}\right)}{\ln\left(1 + \frac{1.45 \times 10^5}{h_r}\right)} \tag{19}$$

Resilient modulus as a Function of Soil Moisture

The soil moisture-resilient modulus relationship is developed by Witczak et al. (2000b). The model is as Eq. (20).

$$\log\left(\frac{M_R}{M_{R,opt}}\right) = a + \frac{b-a}{1+e^{\left\{\ln\left(-b/a\right)+k_m\left(S-S_{opt}\right)\right\}}} \quad (20)$$

where M_R = resilient modulus with at a given time, $M_{R,opt}$ = resilient modulus at a reference condition, a = minimum of $\log\left(M_R/M_{R,opt}\right)$, b = maximum of $\log\left(M_R/M_{R,opt}\right)$, k_m = regression parameter, and $S - S_{opt}$ = variation in the degree of Saturation expressed in decimal.

Inputs and outputs of the ICM are shown in Figure 2. Inputs are sub-divided in five major categories and these are general information, structural and material data, drainage and surface property, weather data, and depth to groundwater table. Attributes under these categories are fed into the ICM as input. The resulting outputs are environmental adjustment factor, depth-temperature profile, moisture content, freeze-thaw cycle, and relative humidity.

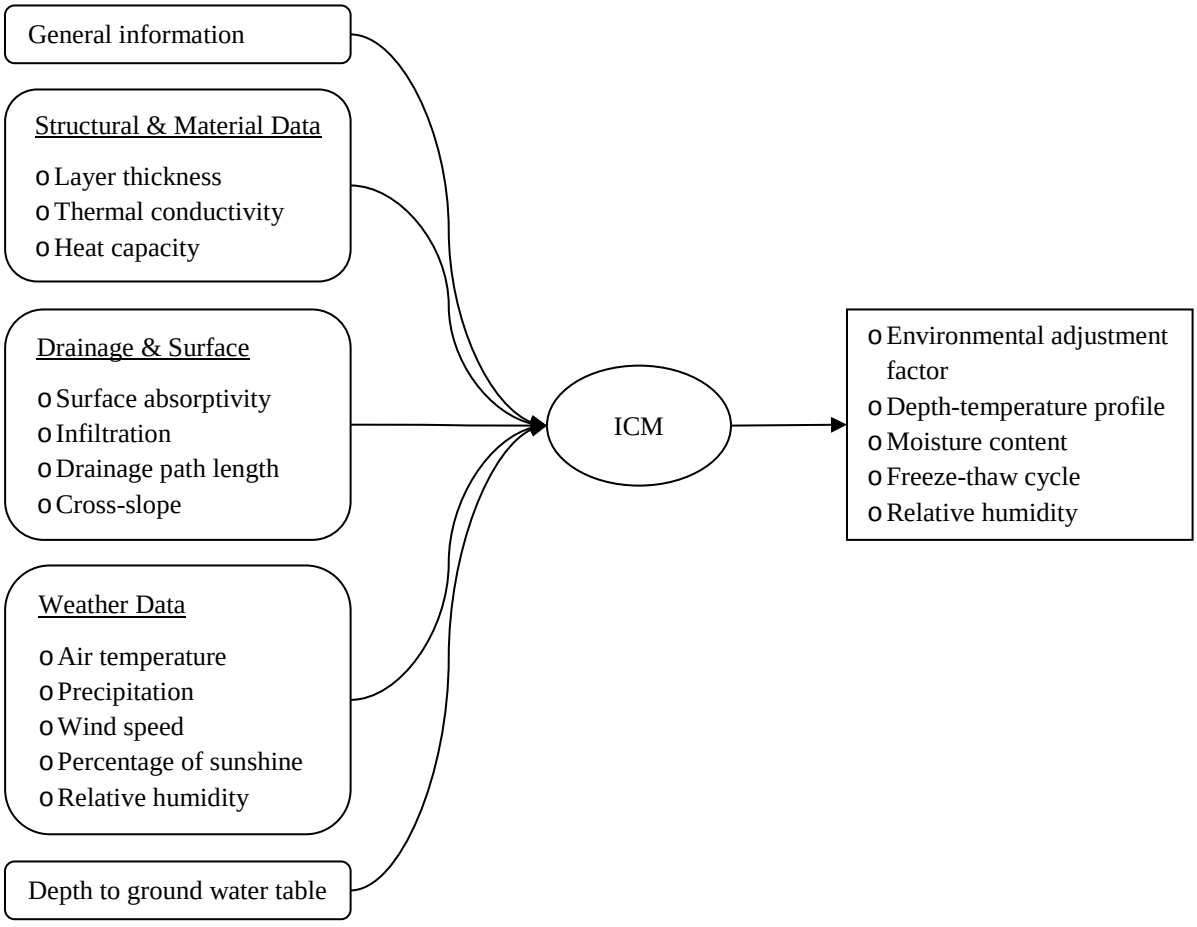

FIGURE 2 Input & Output of the ICM model

Pavement Response Frequency from Embedded Sensor

Due to the viscoelastic nature of the Hot Mix Asphalt (HMA) materials, its mechanical properties are largely dependent on temperature and loading frequency. Previous studies have shown that asphalt materials show linear elastic behavior at low temperature and high loading frequency, however, at high temperature and lower loading frequency, its viscous behavior becomes more dominant *(11)*. In the laboratory, dynamic modulus testing is conducted to determine the $|E^*|$. This test is conducted in the frequency domain at various temperatures to develop the master curve. In the field, the pavement is subjected to loading in the time domain. These loadings can from either vehicle or controlled test truck, such as FWD. Researchers have developed several methods to convert between time and frequency domain. Mechanistic Empirical Pavement Design Guide (MEPDG) uses Odemark's method to calculate the load pulse time duration (t) and then uses $f = 1/t$ to calculate frequency (f).

$$
\begin{aligned}
t &= \frac{L_{eff}}{17.6V} \\
L_{eff} &= 2(a_c + Z_{eff}) \\
Z_{eff} &= \sum_{i=1}^{n-1}\left(h_i \sqrt[3]{\frac{E_i}{E_{SG}}} \right) + h_n \sqrt[3]{\frac{E_n}{E_{SG}}} \\
f &= \frac{1}{t} \\
a_c &= \sqrt{\frac{P}{p\pi}}
\end{aligned}
\qquad (21)
$$

where t = loading time (s)
L_{eff} = Effective length (in)
V = speed (mph)
a_c = radius of contact area (in)
E_{SG}= modulus of subgrade
n = number of layers
h_n = thickness of the layer of interest (in)
E_n = modulus of the layer of interest (psi)
f = loading frequency (Hz)
P = Wheel Load
p = contact pressure

However, recent studies showed that this method of frequency calculation using Eq. (21) may not be accurate *(12, 13)***.** Many researchers have used instrumented pavement section to determine the predominant pavement loading frequency. They have used a vehicle with controlled speed to determine the pavement response through the embedded stress-strain gages. FWD also applies transient loading on the pavement. Therefore, if the pavement response is obtained through embedded sensors then predominant loading frequency under the FWD can also be obtained. There are several ways to obtain the predominant loading frequency under any loadings. In this report, the UNM research team have used Fast Fourier Transformation (FFT) on the pavement response data from embedded field sensors under the FWD test load and traffic load.

Wave Propagation Method for AC Young's Modulus

I-40 instrumentation section has an array of different kind of sensors installed. It has sensors installed at different depths and various sensors at the same depth. Therefore, if a load is applied on top of the pavement surface, the response of the pavement structure can be observed through the installed sensors. When an FWD load is applied on the pavement surface, it creates an impact. This impact produces seismic waves which are detected through the installed accelerometers also known as FWD sensors on the surface, located at a certain distance. This response can be used to deduce many important features about the medium through which the wave travels and about the source that creates these waves. In this study, FWD sensors response under the 9-kip FWD test load is used to determine the elastic properties of the AC.
A seismic event occurring at any place of the earth typically creates an array of energy. These radiated energies are known as seismic waves. These waves can be classified in two ways: depending on the media they are traveling through and based on the particle motion.

Based on the traveling media seismic waves are classified into the following two waves (Figure 3):

- Body wave: seismic wave motion moving through the earth's interior.
- Surface wave: seismic wave moving through surface of the earth.

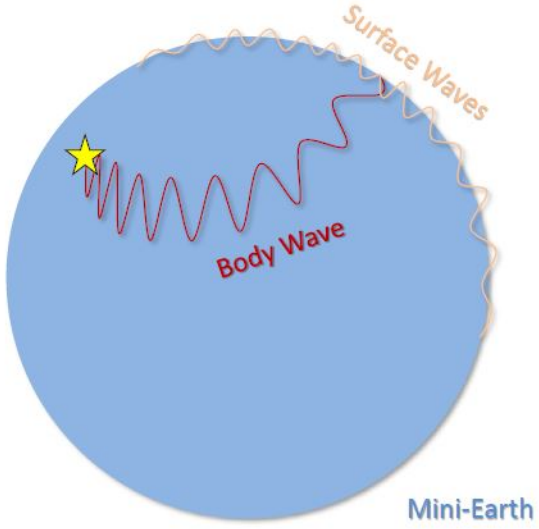

FIGURE 3 Seismic waves traveling through the earth

Based on the particle motion seismic waves are classified into:

- Compressional Wave: when the particles in the material expand or contract in the same direction as in the direction of the wave propagation then it is called a compressional wave.
- Shear wave: when the particles in the medium moves in the perpendicular direction to the wave propagation direction then it is called a shear wave. It causes shear in the medium.

Body waves are p-waves (compression) and s-waves (shear). Rayleigh waves and Love waves are surface waves. Surface waves are produced as a combination of compression and shear waves and they are elliptical in nature.

Seismic waves radiate energy in every direction from the point of origin. These are known as wavefronts. However, for this study wave propagation in a single direction is being considered. Therefore, instead of wavefronts, seismic ray is considered, as shown in Figure 4.

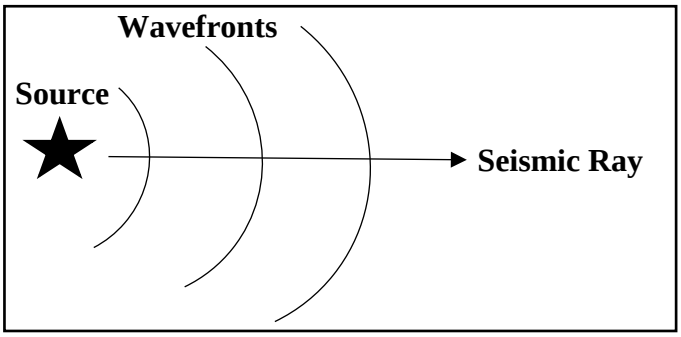

FIGURE 4 Wavefronts and seismic ray

Many researchers have carried out in situ seismic testing of pavement for performance evaluation. Many have used ultra-sonic and radar waves for pavement thickness and performance evaluation *(14, 15)*. Theoretical background for surface wave analysis for determination of Rayleigh wave was proposed in 1962 *(16)*. Heisey et.al. (1982) and Nazarian et.al. (1986) have successfully used the Spectral Analysis of Seismic Wave (SASW) method to determine the thickness and modulus of pavement layers. In their study, they have placed the sensors on top of the pavements. Ryden and Mooney (2009) have also used the Light Weight Deflectometer (LWD) and surface wave analysis technique to obtain pavement performance. The main advantage of using the SASW method is that it gives the material properties of all the pavement layers. However, it requires specialized test equipment. If one has only FWD and interested in the modulus of the AC layer only, or the gradient on how the AC modulus changes with depth, then it is possible to determine the modulus using seismic analysis. The main advantage of using the seismic method with FWD is that it does not require any iterative backcalculation, and it gives the modulus of the AC layer in different lifts, if there is any. It is important to mention that FWD backcalculation gives the modulus of the AC layer as a whole, and it cannot distinguish between the different AC lifts. This is an economical approach as it requires less resources.

Field Instrumentation

This section provides a brief overview of the sensor configurations at the I-40 instrumentation section. Pavement response under any types of loadings, such as traffic or FWD, were obtained from the instrumentation section located on I-40 near Albuquerque, New Mexico. Figure 5 shows the sensor locations in the instrumentation section. There are four layers in the instrumentation section. It has three lifts of HMA, base, subbase and subgrade layer. The instrumentation section has a total of 32 sensors. There are horizontal axial strain gages at the bottom of the first lift of AC. There are also horizontal axial strain gages at the bottom of the third lift of AC, around 10.5

inches from the pavement surface. For this study, strain gage response from the bottom of the third AC lift was used. Figure 5 shows the placement of the strain gage at the bottom of the third AC lift during the construction of the instrumentation section. There are Earth pressure cells (EPC) located at the base, subbase, and subgrade layers. Temperature probes are installed inside the pavement at depth 2, 4, 12, 15 and 21-inch from the surface to collect data every half an hour.

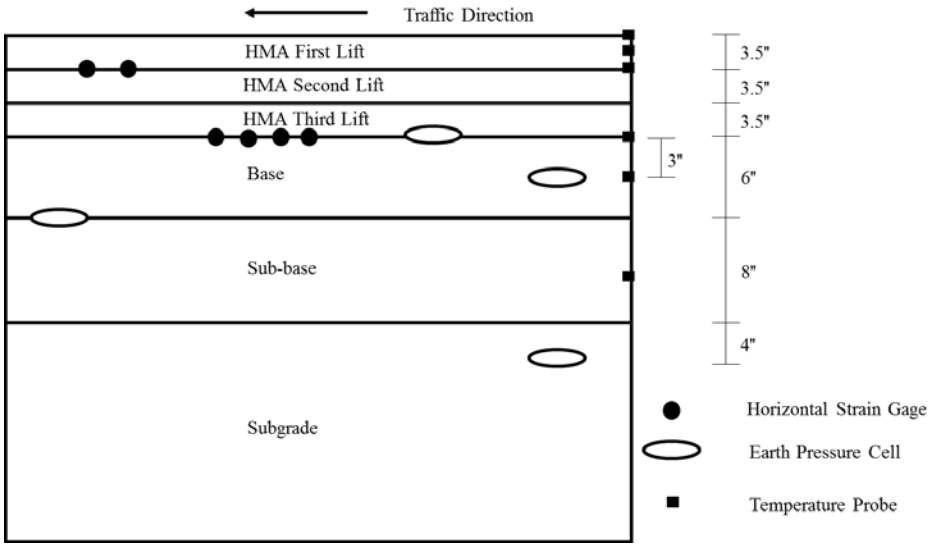

FIGURE 5 Sensor configuration at I-40 Instrumentation section

THIS PAGE LEFT BLANK INTENTIONALLY

FIELD CHARACTERIZATION OF MATERIALS

The AASHTOware pavement ME design guide requires three major inputs: climate, material, and traffic. Along with appropriate climate and traffic inputs, material input such as dynamic modulus (E^*) and resilient modulus (M_R) are needed to calculate pavement responses; mainly stress and strain in the asphalt concrete layer and unbound layers under moving loads through a mechanistic model. These calculated stresses and strains are used to predict pavement distresses such as cracking and rutting through the empirical models.

There are several sensors at the bottom of the AC layer to measure the horizontal strains. Also, earth pressure cells (EPCs) were installed to collect stress values at the base, subbase, and subgrade level. Weather station and temperature probes inside AC layer were also installed to collect continuous data. FWD test at the designated locations of the pavement was conducted since 2012 to observe changes in pavement response pattern.

Continuous pavement response was collected under traffic loadings and FWD test loads of 6, 9, 12 and 16 kips. It was found that pavement stress-strain decreases over time. Furthermore, from FWD test modulus data, field AC damage was quantified. It was observed that AC layer damage is increasing at a steady rate. At the present damage level of the driving lane, no distress was observed. No rutting/fatigue/thermal cracking was observed at the driving lane during Phase I or in Phase II of the study. Therefore, ME distress model could not be calibrated with the data available till now. However, recently (2018) distress (longitudinal cracking, transverse cracking) was observed at the passing lane. It is expected within the next few years these cracks either from shoulder or passing lane may propagate inside the driving lane, and AC damage value will increase rapidly.

STRESS-STRAIN UNDER MOVING LOADS

Figure 6 and Figure 7 shows the variation of pavement response under class 9 vehicle. Figure 6 shows strain variation at the bottom of the HMA layer and Figure 7 shows the stress variation in the unbound layers from EPC under the single and tandem axle of class 9 vehicle. The reason for showing the pavement response variation under class 9 vehicle is the dominance of this vehicle class over the other vehicle class at I-40. From WIM data analysis, it was observed that around 76% of the total vehicle passing through I-40 are class 9 vehicle. In these two graphs, pavement responses are plotted with an average AC temperature. From both Figure 6 and Figure 7, it can be observed that both HMA strains, and base, subbase, and subgrade stresses are decreasing with time.

HMA strain in Figure 6 ranges from 142 με to 22 με. It is well known that AC response is temperature dependent, therefore, it is ideal to compare the AC strain responses that are close in temperature. For example, in April 2013, July 2015, September 2017 and September 2018 average AC layer temperature was around 27°C. In these months, average AC strain under tandem axle was found to be around 86 με, 66 με, 61 με and 68 με. Therefore, it can be said that from 2013 to 2018 HMA strain under tandem axle decreased around 26%. This decrement in strain response with time may be due to the damage of the AC layer.

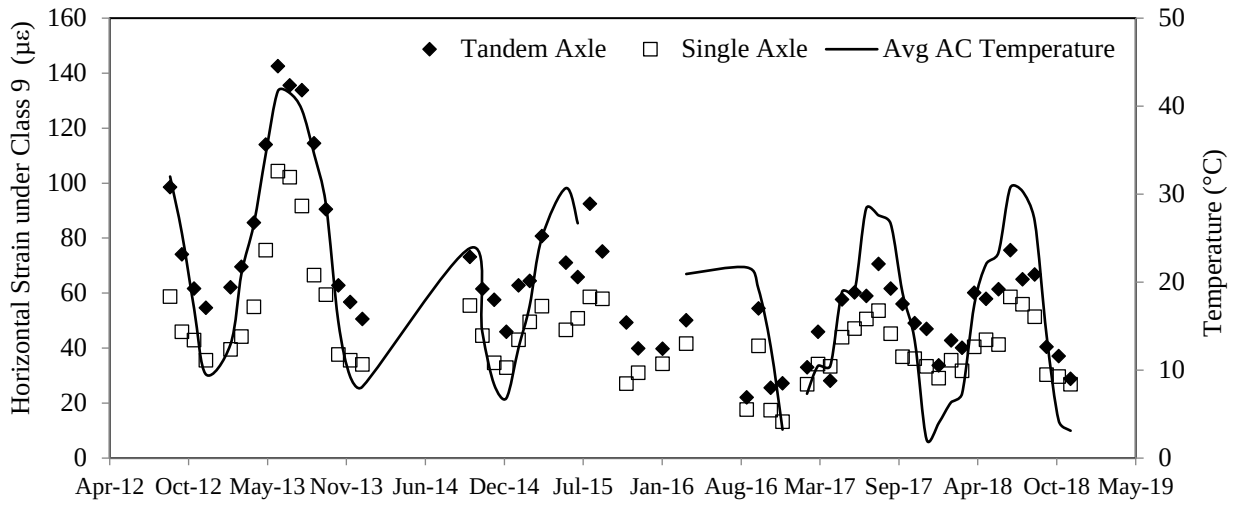

FIGURE 6 Yearly variation of strain at the bottom of the HMA layer under class 9 vehicle

Similarly, from Figure 7 it can be observed that vertical stresses in base range from 9.8 psi to 1.89 psi under tandem axle between 2013 to 2018. Average base stress under tandem axle in 2013 was around 6.34 and the value reduced to 3.3 in 2018. Therefore, there is a decrease of around 50% in the base response under tandem axle within four years after construction. Like the base layer, around 50% decrease in stress response under tandem axle was also observed in the subbase and subgrade layer.

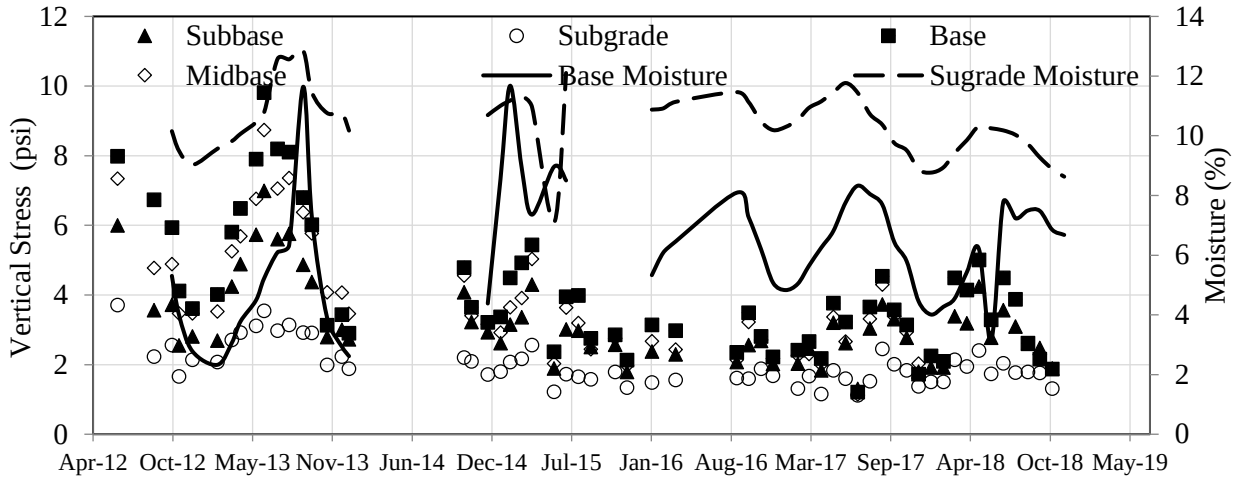

FIGURE 7 Yearly variation of stresses at various unbound layers under the tandem axle of class 9 vehicle

STRESS-STRAIN UNDER FWD TEST LOADS

Continuous FWD test on the instrumentation section was conducted since 2013 to observe the changes in layer moduli and stress-strain data. FWD test data can be used to develop field dynamic modulus and pavement performance curve to quantify damage, which can be used to perform timely rehabilitation.

Pavement responses were also obtained from the embedded sensors under the FWD test loads. Figure 8 shows the variation of the horizontal strain under the bottom of the HMA layer from the FWD test load from 2012 to 2018. This figure also shows the variation of the average temperature of the HMA layer within this time period. Figure 8 shows that there is a relationship between the HMA layer response and the average AC temperature. Horizontal strain response of HMA is directly proportional to the changes in average HMA temperature. As the HMA temperature rises, strain response at the bottom of the HMA layer increases and vice-versa. In the summer of 2013, July 2013, the maximum strain was obtained, which was around 152 με, and in December 2018 the value was found to be around 26 με. For this reason, it is important to compare the pavement response by shifting them to a common temperature. Figure 9 shows a comparison between the responses of the HMA layer when they were shifted to a common temperature of 21°C. From Figure 9 it can be observed that on July 2013 the horizontal strain at the bottom of the HMA layer was 100 με, but in April 2018 the value decreased to 40 με. Therefore, within 5 years of pavement construction, the response has decreased by 60%. As mentioned previously, this decrement is mainly due to the damage in the AC layer.

Figure 10, Figure 11 and Figure 12 shows the variation of stress in the base and subbase layer from 2012 to 2018. These figures show that initially, immediately after construction, the stresses in the unbound layers increased, but it decreased from the initial high value and remained almost the same. The reason for the initial increament may be due to the high temperature in 2013 and stress dependency on the AC layer. At first, after construction, pavement was new and more flexible. Thus, at high temperature under loading it flexed more. However, with time, AC layer got damaged and subsequently changed the stress responses in the unbound layers as well.

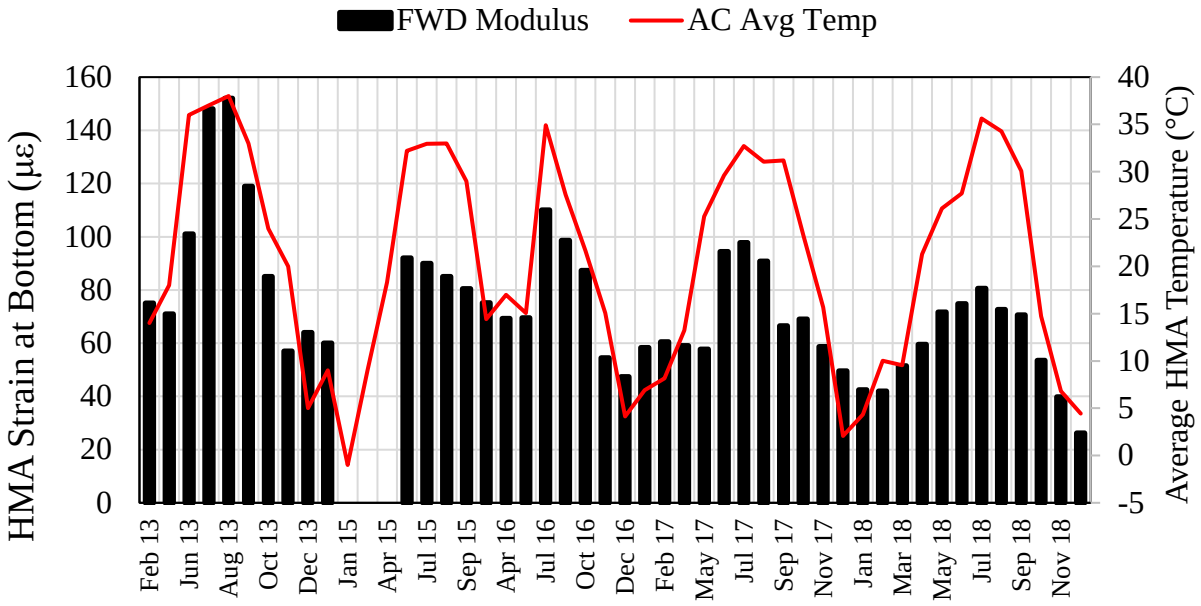

FIGURE 8 Strain at the bottom of HMA layer under FWD test load

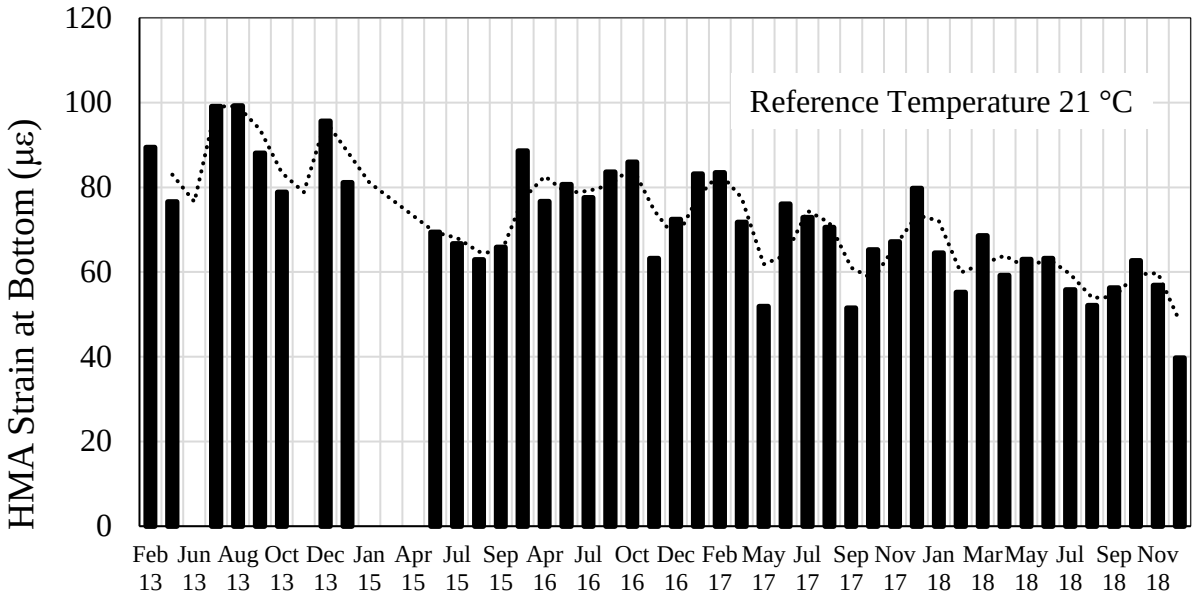

FIGURE 9 Strain at the bottom of HMA layer under FWD test load at reference temperature of 21°C

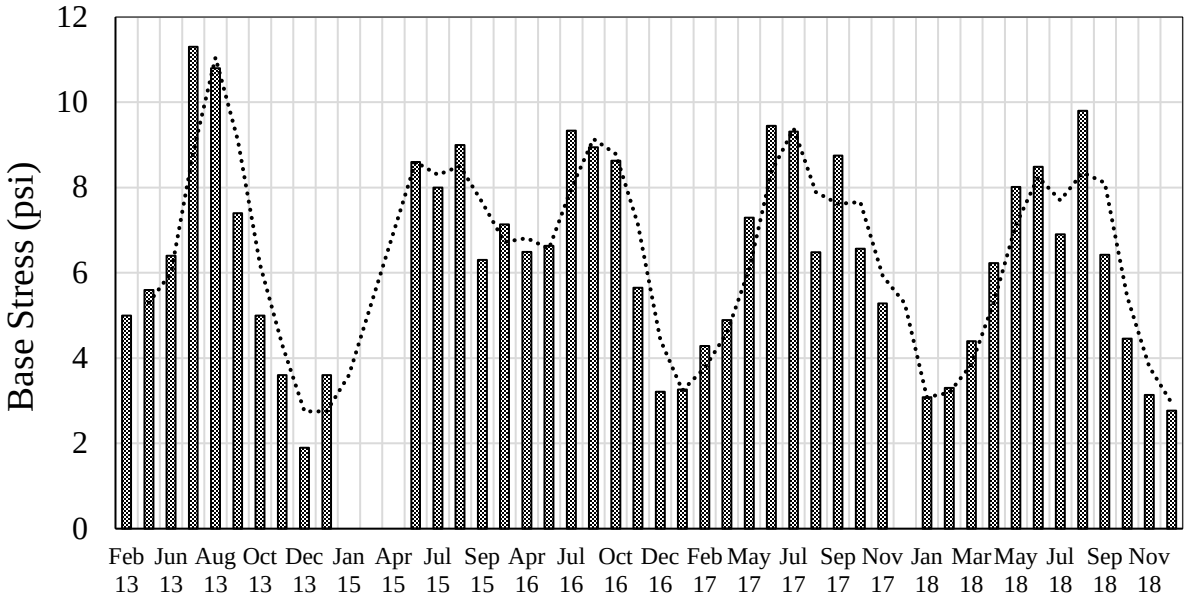

FIGURE 10 Stress variation at base layer under FWD test load

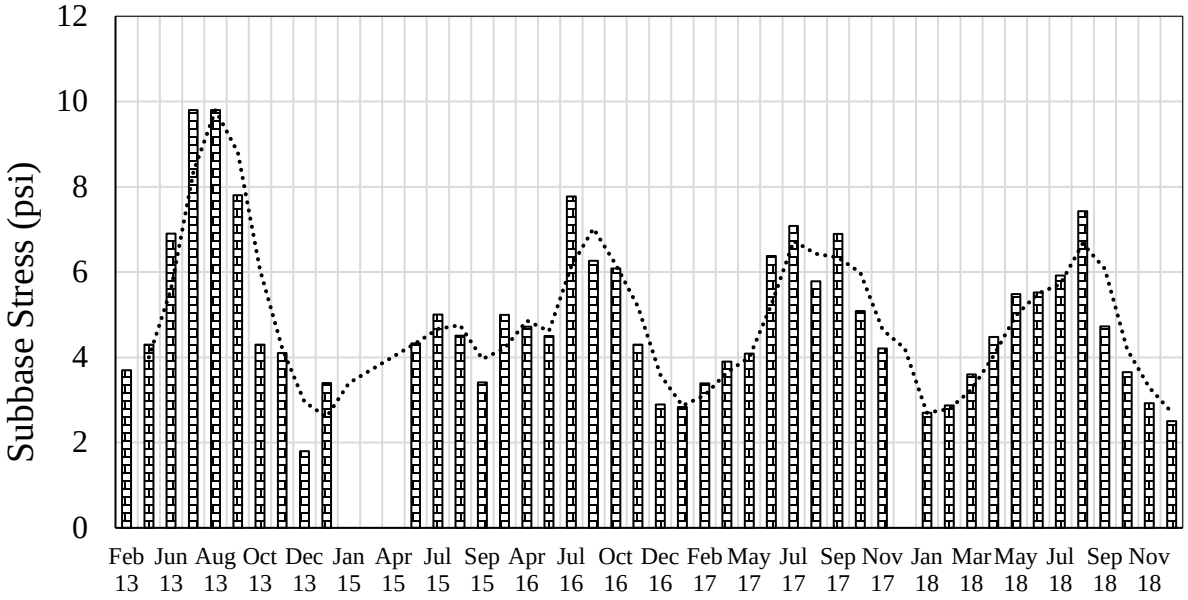

FIGURE 11 Stress variation at subbase layer under FWD test load

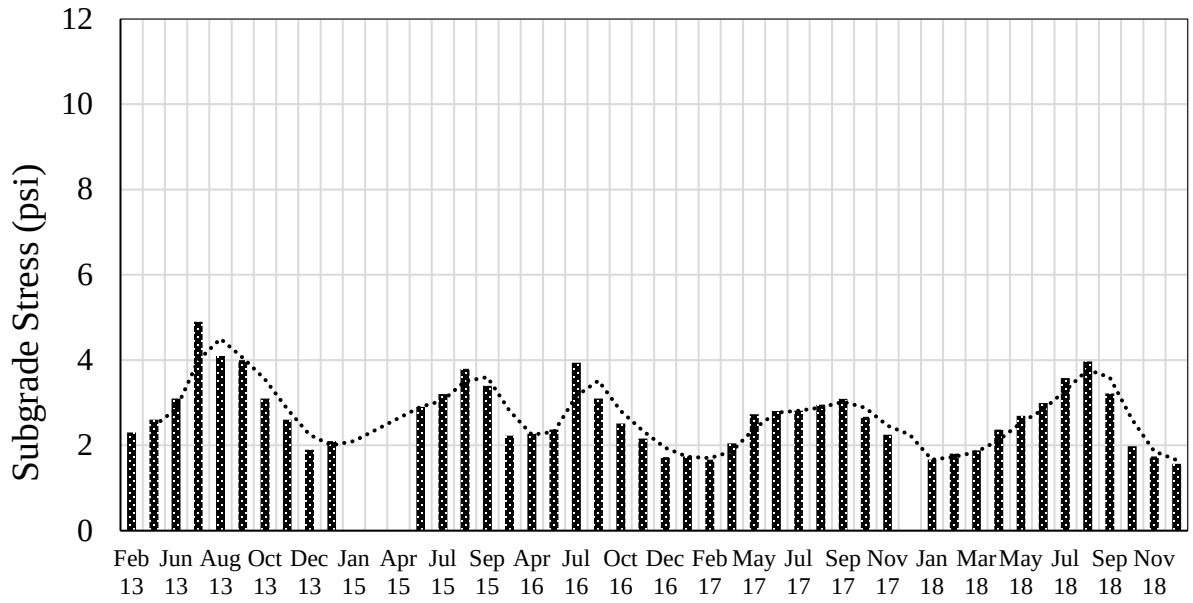

FIGURE 12 Stress variation at the subgrade layer under FWD test load

It is important to observe how this pavement response changes when all the elements of damage, such as aging, delamination, and cracking, are present in the field, or in another way, at what value of strain/stress cracking first occur in the AC layer at the field. Until now, it is not possible to measure exactly at what onset of stress and strain cracking first observed in the field. To understand the variation in field pavement behavior due to aging and distress, it is important to continue collecting the data, observe the subsequent changes and compare field response with AASHTOWare predicted values.

AC MODULUS

During Phase I and Phase II of the I-40 instrumentation project, regular monthly FWD test was conducted. Figure 13 shows the variation of FWD AC modulus with the reference temperature at 21°C. Due to the damage in the AC layer, modulus has decreased since the construction of the pavement. To ensure that the pavement survives its design life and to develop a maintenance schedule, it is important to know how much damage has occurred in the pavement. Once the modulus for various months have been shifted to a common reference temperature, damage of the AC layer can be calculated. For calculation of damage parameter, dynamic modulus value of newly constructed AC layer is required. This value was obtained from the laboratory prepared sample. The sample was prepared using the same AC mix specification that was used in the I-40 instrumentation section construction.

AC properties are changed constantly due to various chemical and physical forces. AC modulus is dependent on temperature and frequency. Therefore, in the laboratory, AC modulus is measured on different temperature and frequency. Using time temperature superposition *(20)* dynamic modulus master curve is constructed. Master curve can be represented by a nonlinear sigmoidal function:

$$\log(E^*) = \delta + \frac{\alpha}{1 + e^{\beta + \gamma(\log f_r)}} \tag{22}$$

In Eq. (22), δ is the minimum value of E^*, $\delta+\alpha$ is the maximum value of E^*, f_r is the loading frequency at the reference temperature, and β and γ are the shape parameters. Value of α, β, δ can be obtained using bitumen viscosity and volumetric properties (V_a, V_{beff}, ρ_{34}, ρ_{38}, ρ_4, ρ_{200}). Here, η = bitumen viscosity, V_a = air void content (%); V_{beff} = effective bitumen content, (% by volume); ρ_{34} = cumulative % retained on the 3/4 in sieve; ρ_{38} = cumulative % retained on the 3/8 in sieve; ρ_4 = cumulative % retained on the No. 4 sieve, and ρ_{200} = passing of the No. 200 sieve. A Detailed procedure for obtaining these values can be obtained from AASHTO *(5)*.

AASHTO *(5)* also outlined a method to calculate the dynamic modulus based on FWD test. In that method, FWD modulus (E_{FWD}) is conducted at the field temperature, *T*. Field core is collected to obtain the volumetric properties. From these volumetrics, undamaged dynamic modulus (E^*) is obtained from Witzack equation *(21)*. Damage parameter, d_j, is calculated by

$$d_j = \frac{E_{FWD}}{E^*} \tag{23}$$

Using the damage parameter α' is calculated by using $\alpha' = (1- d_j)\alpha$. Then, α' is used instead of α in Eq. (22) to construct master curve.

Figure 13 shows the variation of AC modulus from 2015 to 2018 with the reference temperature at 21°C.

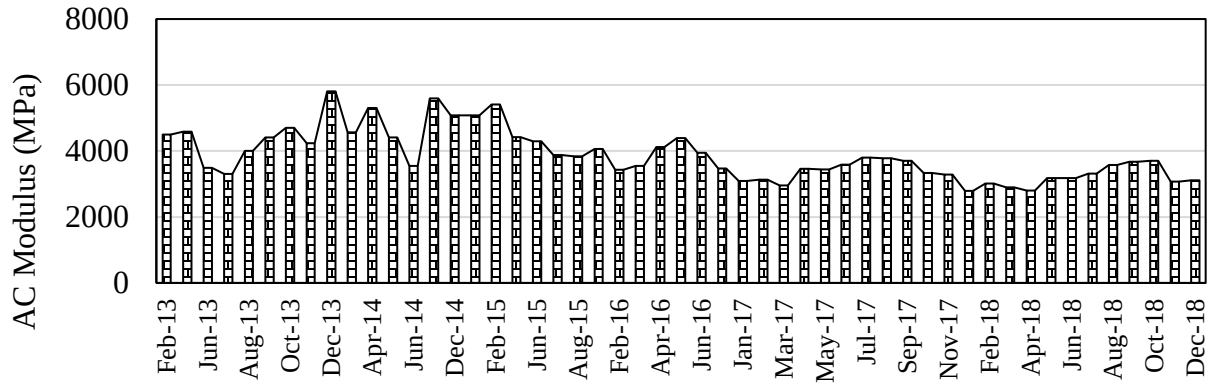

FIGURE 13 Variation of AC modulus with time at reference temperature of 21°C

Figure 14 shows the variation of AC layer damage parameter with time (1 means excellent pavement 0 means fully damaged pavement). At the beginning in February 2013, the AC layer damage parameter was around 0.94 and at the end of 2018, AC layer damage parameter is 0.83. Therefore, within 5 years, I-40 instrumentation section AC layer has been damaged around 11%. It is important to note that at the beginning, in February 2013, pavement damage parameter was around 0.94, not 1. The damage parameter in Figure 14 was obtained by comparing field damaged FWD modulus with undamaged modulus. The difference between field damaged FWD modulus and laboratory undamaged modulus made the damage parameter to start at 0.94.

Figure 14 also shows that at the beginning pavement damage was slow and with time the slope of damage has increased. As mentioned earlier, until phase II, no cracking has been observed at the instrumentation section. The AC damage shown in Figure 14 is mainly due to environment and traffic factors. However, distresses are expected to appear in the driving lane in the next few years, as it has already appeared on passing lane and shoulder. It is important to observe how the pavement damage parameter slope changes when cracking starts to appear in driving lane AC, where the sensors are located. This information can be used to develop a rehabilitation schedule, which will prevent the complete failure and costly reconstruction of the pavement.

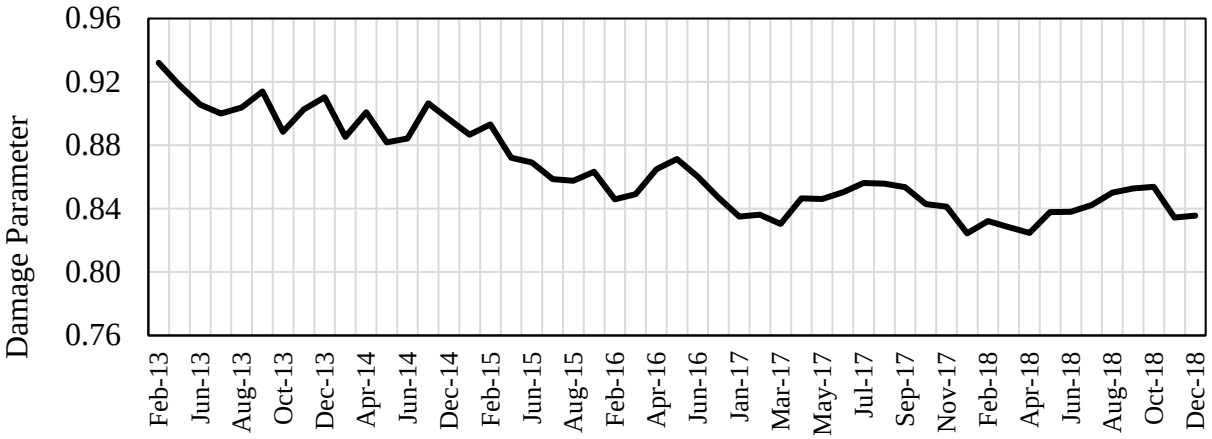

FIGURE 14 Damage parameter variation for AC layer since 2013 to 2017

The damage occurred in the AC layer so far is due to the environmental and traffic factors. It is possible to quantify how much damage has occurred in the AC layer due to these factors individually and what is the effect of this 11% damage. To identify the extent of damage due to the traffic alone, a combination of WIM data, FWD data and embedded sensor data needs to be analyzed.

WIM DATA ANALYSIS

WIM data has been collected from the I-40 WIM station. Data from January 2015 to July 2016 has been analyzed. The summary of traffic data for I-40 is given in Table 2. The station code of the WIM station is ‘r01000’. There are a total of four lanes in that section (two in each direction). The positive direction is ‘East’ direction and negative direction is ‘West’ direction.

TABLE 2 Summary of traffic data for I-40

Item name	Measured data
State Code	35
Station ID	r01000
Year	2015-16
Number of Lane	4
Positive direction	3 (East)
Negative direction	7 (West)
AADT	26076
AADTT	9207
Truck factor	35.5

Directional Distribution

Directional distribution of traffic is given in Figure 15. From the analyzed data it was observed that for January 2015 to July 2016, percentages of traffic in eastbound and westbound directions is almost evenly poised. Eastbound traffic was found to be 49.8% while westbound traffic was observed to be 50.2%. This value closely agrees with the assumed value in AASTHOWare ME design software, where directional distribution is 50% in both east and westbound traffic lanes.

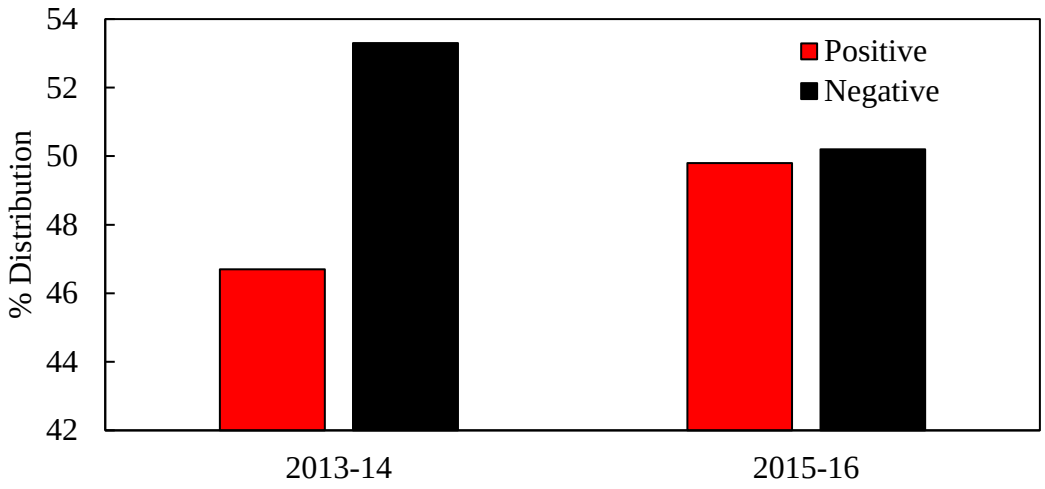

FIGURE 15 Directional Distribution

Lane Distribution

Lane distribution of truck traffic is given in Figure 16. Here, Lane 1 and Lane 2 are toward the positive direction (East) where Lane 3 and Lane 4 are toward negative direction (West). In the east bound lane, 69% of trucks drive through the driving lane and 31% of trucks use the passing lane. The AASHTOWare default value is 95% for the design lane, say driving lane. For the westbound direction it was observed that 48% of truck traffic drives through the driving lane while 52% of truck traffic uses the passing lane. For Lane 1, there has been a decrease in traffic distribution since 2013-14 and the value is 16%, while for Lane 2 there is an increase and the value is 16%. From 2013-14, there is an increase in traffic in Lane 3 and the value is 21.4%, and traffic decrease of 21.4% was observed in Lane 4 from 2013-14 to 2015-16.

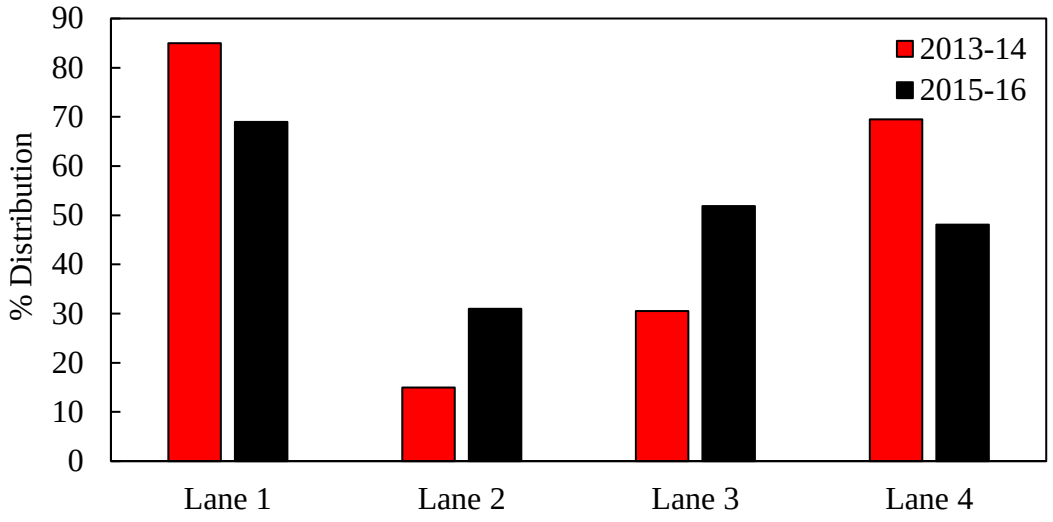

FIGURE 16 Lane Distribution

Hourly Distribution

Figure 17 shows the hourly traffic distribution. It can be observed that the data is not normally distributed, which is expected. It was also observed that most of the traffic travels during 10 AM to 5 PM. The maximum volume of traffic is observed at around 2 PM. It was also observed that around 2% of traffic travels during the late night time.

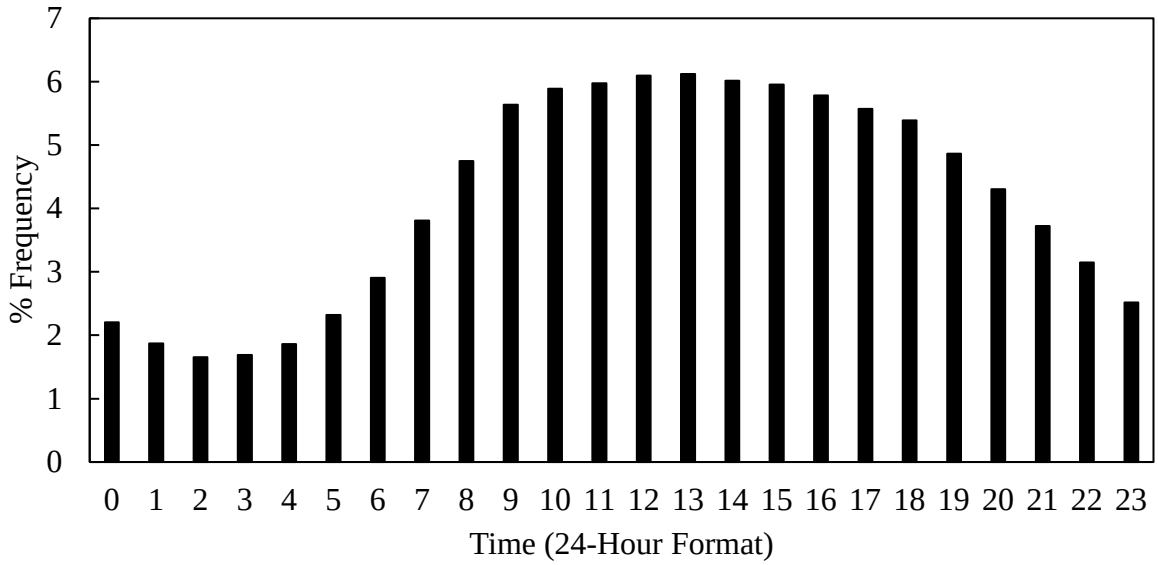

FIGURE 17 Hourly Traffic Distribution

Truck Class Distribution

Figure 18 shows the truck class distribution for 2013-14 and 2015-16. It can be seen that from 2013-14 to 2015-16 vehicle class distribution remains almost identical. The dominant vehicle class was observed to be class 5 and class 9. In 2013-14 and 2015-16, class 5 vehicle was observed to be around 15% and class 9 vehicle was observed to be around 71%.

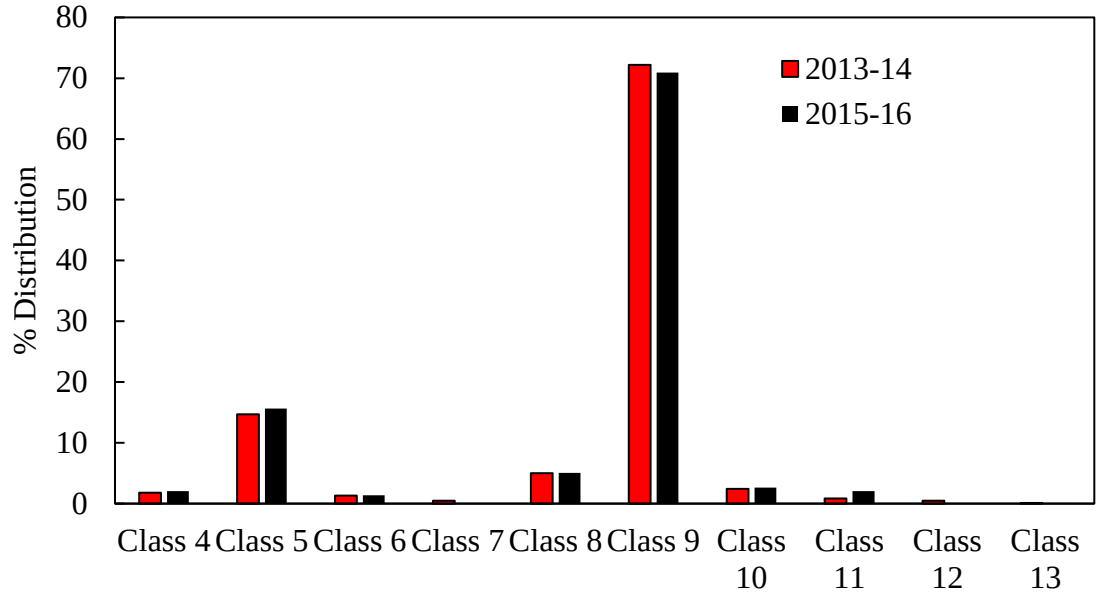

FIGURE 18 Truck Class Distribution

Truck Traffic Growth

Figure 19 shows the increase in truck traffic volume over the year. In January 2015, average monthly truck traffic was 7931 where in January 2016 the value was 8990. For the whole year of 2015, average monthly truck traffic growth was about 1.3%. However, for the first 7 months of 2016 (January 2016 – July 2016) average monthly traffic growth rate was observed to be around 2.42%, which is almost double than what was observed in 2015.

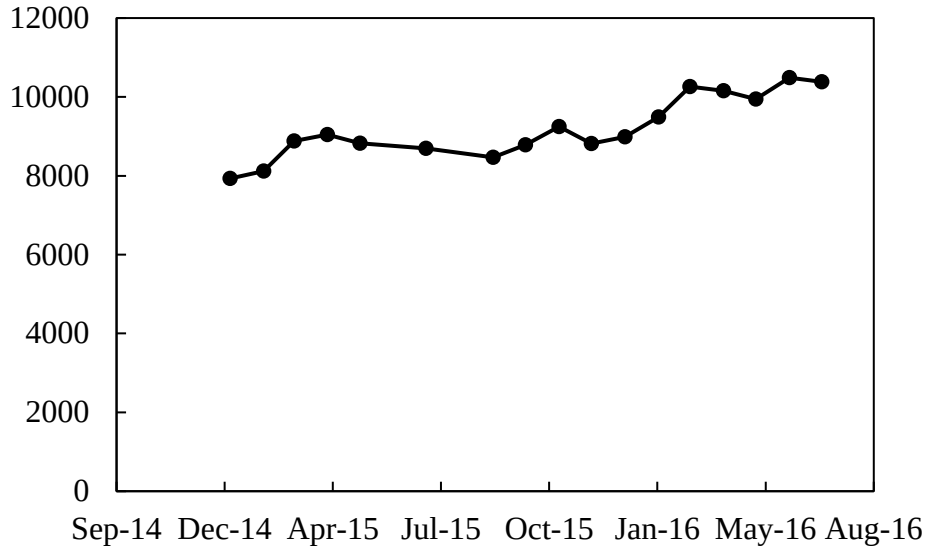

FIGURE 19 Truck Traffic Growth

Axle Load Spectra for Class 9 Vehicle

Single Axle Load Spectra

Figure 20 shows the single axle load spectra for class 9 vehicle. This is the average single axle load spectra for the period of January 2015 to July 2016. From AASHTOWare ME software, maximum single load spectra is observed at 10000 lbs with a frequency of 17.7%. However, from Figure 20 it can be observed that the WIM data from I-40 shows the maximum frequency of 46.8 at axle load of 12000 lbs.

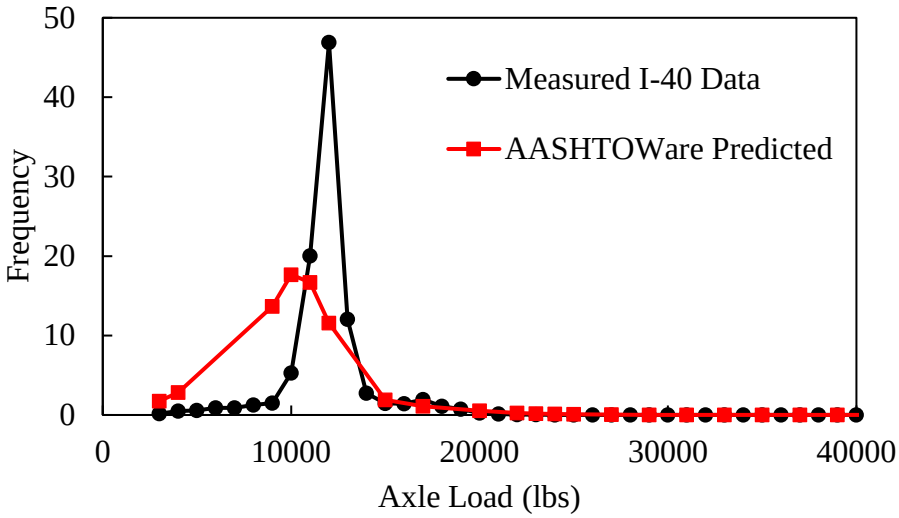

FIGURE 20 Annual Average Single Axle Load Spectra

Tandem Axle Load Spectra

Figure 21 shows the tandem axle load spectra for class 9 vehicle. This is the average tandem axle load spectra for the period of January 2015 to July 2016. From AASHTOWare ME software, maximum tandem load spectra is observed at 20000 lbs with a frequency of 17.7%. However, from figure 6 it can be observed that the WIM data from I-40 shows the maximum frequency of 13.8 at axle load of 32000 lbs.

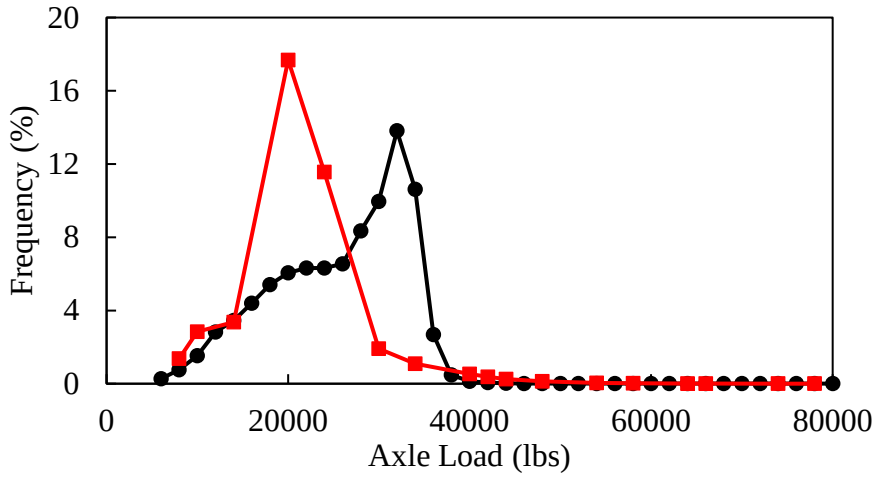

FIGURE 21 Annual Average Tandem Axle Load Spectra

Gross Vehicle Weight for Class 9

Figure 22 shows the gross vehicle weight for class 9 vehicles. This figure also shows that the maximum number of vehicles, 44150, have the gross vehicle weight of 74406 lbs.

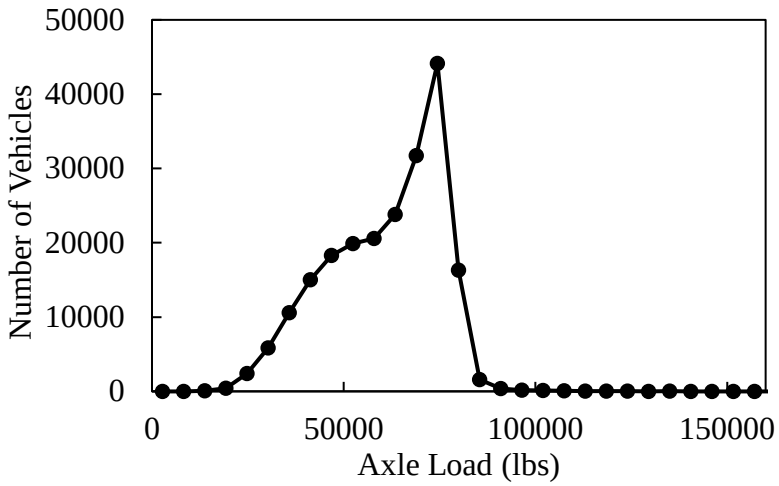

FIGURE 22 Gross Vehicle Weight Distribution

Steering Axle Weight for Class 9

Figure 23 shows the steering axle weight for class 9 vehicles. From Figure 23, it can be observed that the maximum number of vehicles, 99054, have the steering axle weight of 11574 lbs.

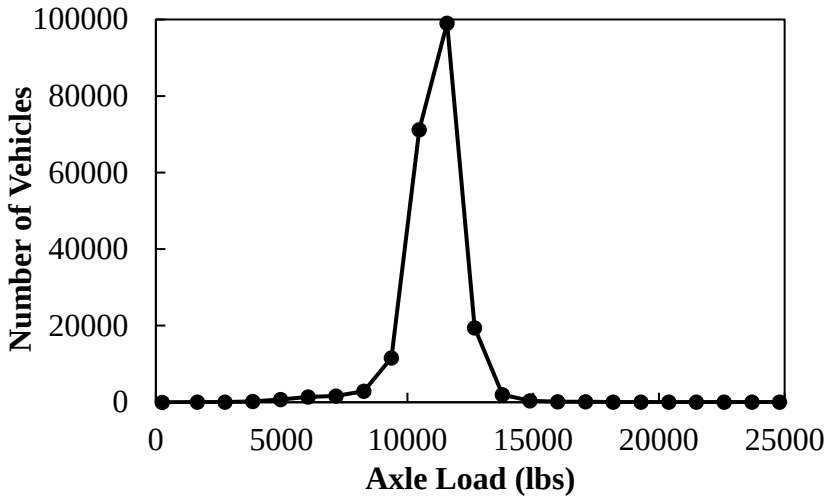

FIGURE 23 Steering Axle Weight Distribution

Average Axle per Vehicle

Table 3 shows the average axle per vehicle from the period of January 2015 to July 2016. From Table 3, it can be observed that for class 9 vehicle, the average single axle is 1.2 and the average tandem axle per vehicle is 1.9.

TABLE 3 Average Axle per Vehicle Class

Class	Single	Tandem	Tridem	Quad
Class 4	1.7	0.3	0	0
Class 5	2	0	0	0
Class 6	1	1	0	0
Class 7	0.6	0.8	0.6	0
Class 8	2.1	0.9	0	0
Class 9	1.2	1.9	0	0
Class 10	1	1	1	0
Class 11	3	0.8	0.1	0
Class 12	1.2	2.1	0.2	0
Class 13	1	1.9	0.1	0.1

Measured Monthly Adjustment Factor

The measured Monthly Adjustment Factor (MAF) for Class 4 to Class 13 is shown in Table 4. The AASHTOWare default values are unity for all months and classes. This means the AASHTOWare assumes the vehicle equally distributed in each month. The measured values from I-40 are way different than the AASHTOWare default ones. For example, the Class 9 vehicle is 0.87 instead of 1 in the month of February 2015, which is 13% less than the assumed AASHTOWare value.

TABLE 4 Measured Average Monthly Adjustment Factor

Vehicle Class	January	February	March	April	May	July	September	October	November	December	Total
Class 4	0.83	0.82	1.06	1.05	1.09	1.06	1.04	1.13	0.99	0.93	10.00
Class 5	0.95	0.85	1.09	0.99	1.04	1.09	0.91	0.94	1.03	1.10	10.00
Class 6	0.92	0.86	1.02	1.00	1.01	1.00	0.93	1.00	1.13	1.12	10.00
Class 7	0.67	0.82	0.96	1.24	1.35	1.42	1.26	1.17	0.53	0.58	10.00
Class 8	0.74	0.72	1.11	1.17	1.13	1.09	1.03	1.19	0.97	0.86	10.00
Class 9	0.94	0.87	1.03	1.02	1.03	1.00	0.96	1.03	1.06	1.04	10.00
Class 10	0.93	0.91	0.95	1.08	1.03	1.05	0.98	1.07	1.04	0.98	10.00
Class 11	0.96	0.85	1.05	1.07	1.02	1.06	1.04	1.08	0.95	0.92	10.00
Class 12	0.42	0.52	0.94	1.17	0.99	1.93	1.88	1.08	0.67	0.40	10.00
Class 13	0.64	0.74	1.02	1.02	1.08	1.55	1.16	1.02	0.85	0.93	10.00

FATIGUE DAMAGE BY CLASS 9 VEHICLE

In this study, fatigue damage in AC layer due to class 9 vehicle is studied. Figure 24 shows the truck class distribution for 2016-17 obtained from the WIM station in I-40 at MP 148. Due to the instrumentation problem at the WIM station at MP 148, recent data could not be used. Figure 24 shows that the most dominant vehicle class is class 9. As mentioned earlier, class 9 vehicle was observed to be around 73%, higher than any other vehicle class. For this reason, class 9 vehicle is studied for fatigue damage.

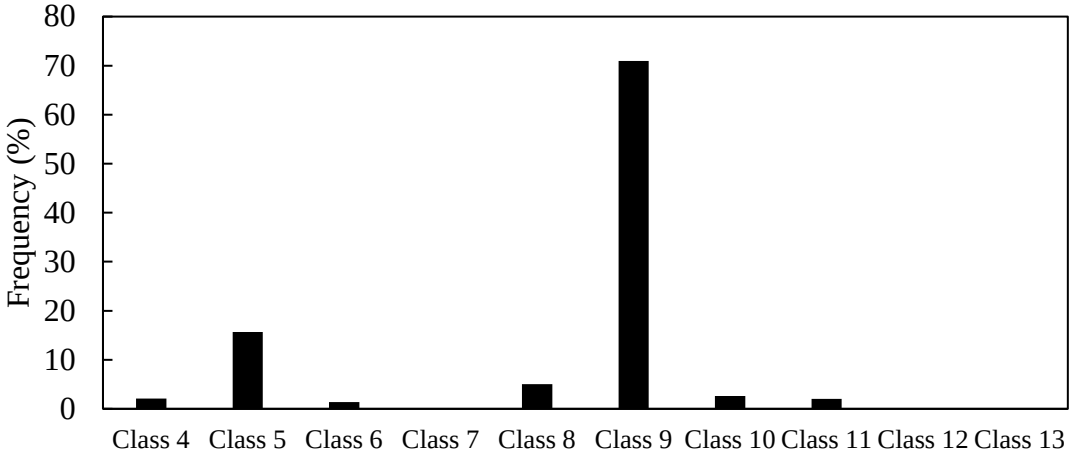

FIGURE 24 Truck Class Distribution

Furthermore, it is also difficult, sometimes not possible, to distinguish between different vehicle classes. Whenever any traffic leaves the instrumentation section, its footprint is captured by the installed sensors. However, as there is no video recording system, the class of the vehicle is identified from the signal's registered footprint. Figure 25 shows the signal footprint of the class 9 vehicle. It has a distinct 5 peaks for five axles obtained at 100 Hz frequency.

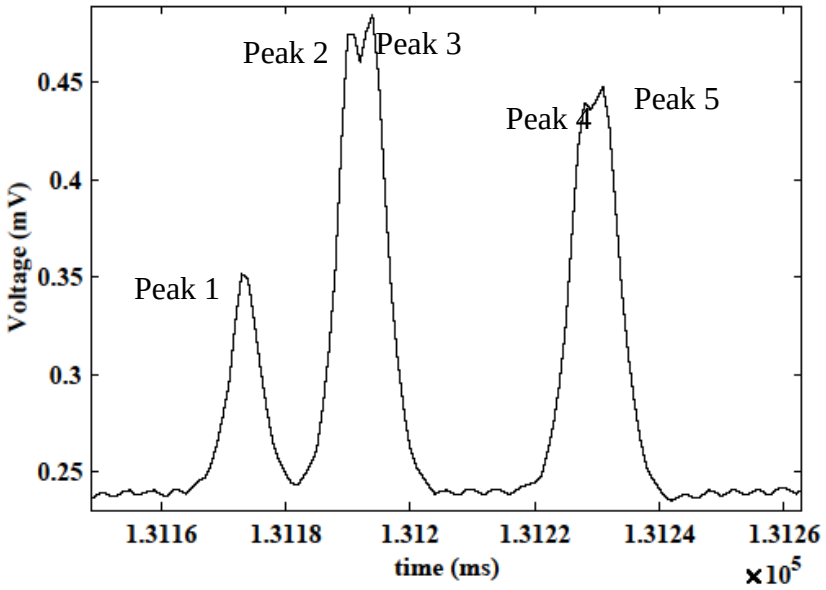

FIGURE 25 Class 9 vehicle signal footprint

However, for other types of vehicle class, the signal footprint is not easily distinguishable**.** Figure 26 shows the possible signal footprint of possible 2,3,5 or 4,8 vehicle class. Therefore, for accuracy in comparison, only class 9 vehicles are used in this study.

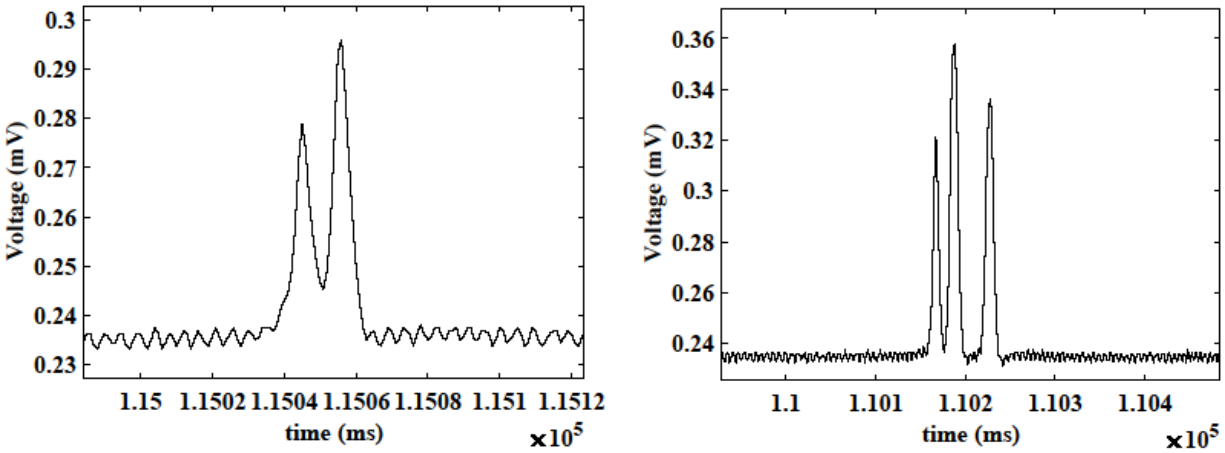

(a) Possible vehicle class 2, 3 or 5 (b) Possible vehicle class 4 or 8

FIGURE 26 Signal Footprint not easily matched to vehicle class

The fatigue damage of AC layer under class 9 vehicle is calculated based on the cumulative damage concept. In this concept, a damage factor is defined as the damage occurs due to per pass of a certain vehicle class on a certain pavement type. According to Miner's hypothesis, damage is cumulative. Eq. (24) shows the damage due to various load groups.

$$S = \sum_{i=1}^{n} S_i \tag{24}$$

Where, S = damage due to n number of load groups,
n = number of load groups,
and S_i = damage due to i-th load group

Damage due to any particular load group is defined as

$$S_i = \frac{N_i}{N_{f,i}} \tag{25}$$

Here, N_i is the load repetitions for the i-th load group and $N_{f,i}$ is the allowable load repetitions for the i-th load group. For this study, only one load group, vehicle class 9, is selected.

In this study, the value of N_i is obtained from the WIM station data for class 9 vehicle. Figure 27 shows the total monthly count of class 9 vehicle. The value for $N_{f,i}$ is obtained using the equation developed by the Asphalt Institute, which is shown in Eq. (26)**.**

$$N_{fi} = 0.0796\varepsilon_t^{-3.291}|E|^{-0.854} \tag{26}$$

Here, $N_{f,i}$ is the allowable load repetitions, ε_t is the tensile at bottom of AC layer obtained from sensor and E is the modulus obtained from FWD test.

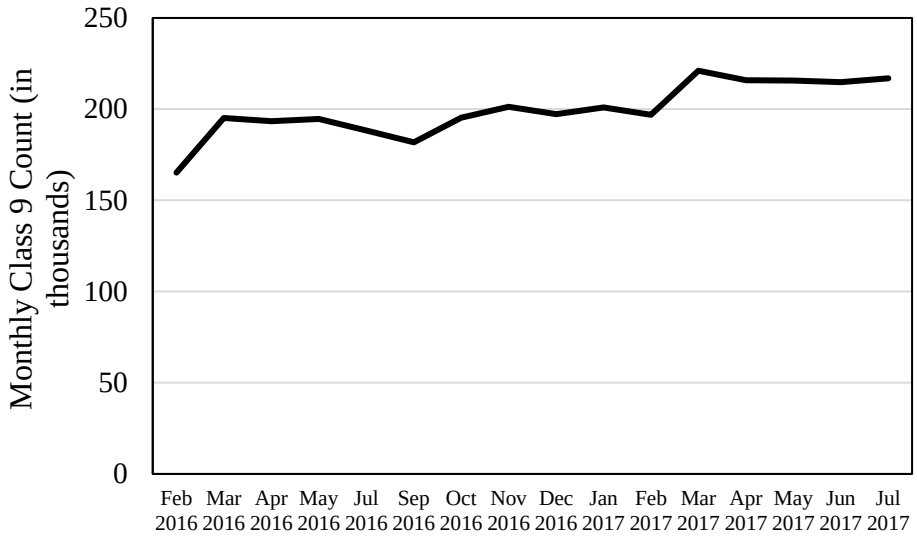

FIGURE 27 Monthly class 9 vehicle count

In this study, temperature correction for AC was applied according to the LTPP guide to asphalt temperature prediction and correction *(22)*. In this method, the adjustment factor is obtained as shown in Eq. (27):

$$adj.fac = 10^{slope(Tr-Tm)} \tag{27}$$

Here, *adj.fac*= modulus adjustment factor, *slope* = Log(*Modulus*) = intercept + slope *T*, *Tr* = reference temperature, *Tm* = measured temperature.

First, a graph is drawn between Log (AC Modulus) vs. Temperature. The graph is shown in Figure 28. A linear trend in logarithmic modulus and temperature can be observed in Figure 28. From this, the slope is obtained. The slope is used in Eq. (27) to obtain the modulus adjustment factor. With the adjustment factor, AC modulus, from 2015 to 2017, is shifted to a reference temperature of 21°C, as shown in Figure 29.

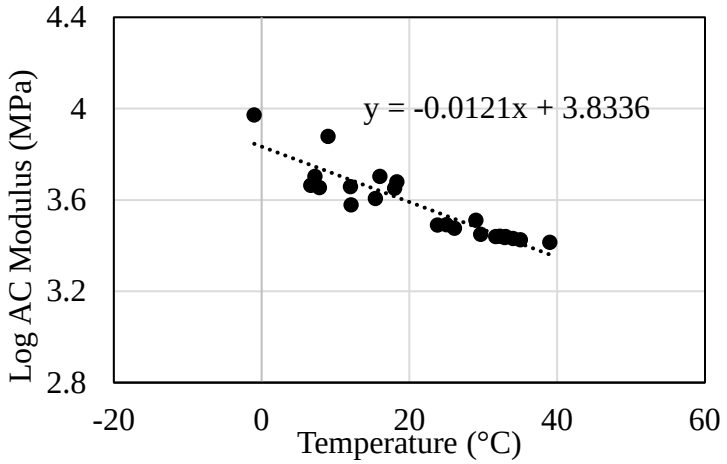

FIGURE 28 Variation of logarithmic AC modulus with temperature

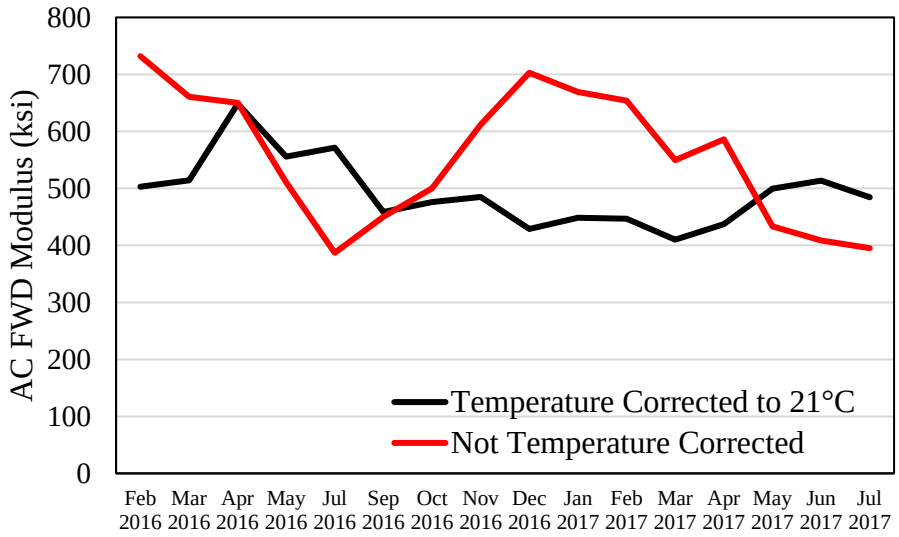

FIGURE 29 AC FWD Modulus Distribution

Similar methodology of temperature correction is also used for the tensile strain at the AC bottom obtained from the sensor under class 9 vehicle as seen in Figure 30.

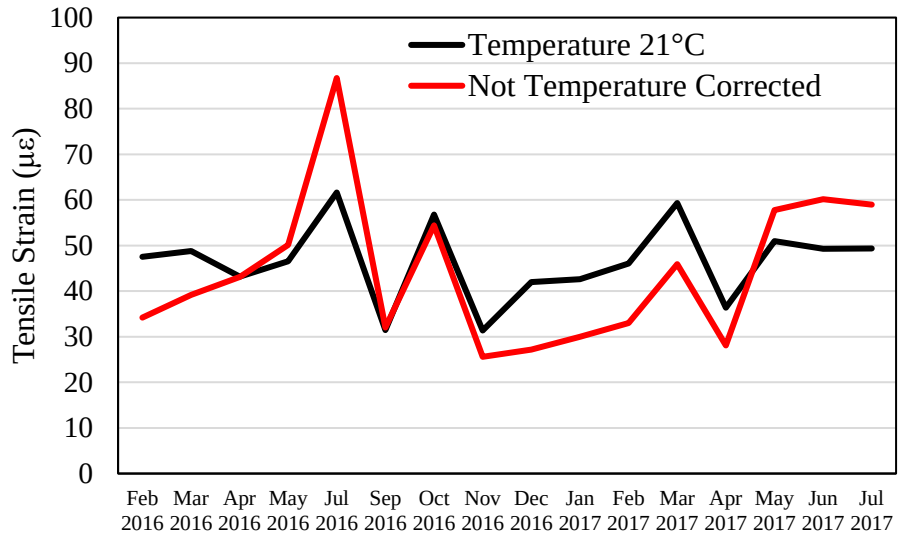

FIGURE 30 Tensile Strain Distribution

Figure 31 shows the damage accumulation per month in the I-40 instrumentation section due to the class 9 vehicle only. From Figure 31 it can be observed that damage varies in different months of the year due to the variation in the tensile strain at the bottom of AC and modulus. As expected, cumulative damage follows almost a straight line. From cumulative fatigue damage analysis under class 9 vehicle, it can be observed that damage in the AC layer is accumulating at a rate of 0.1% per month.

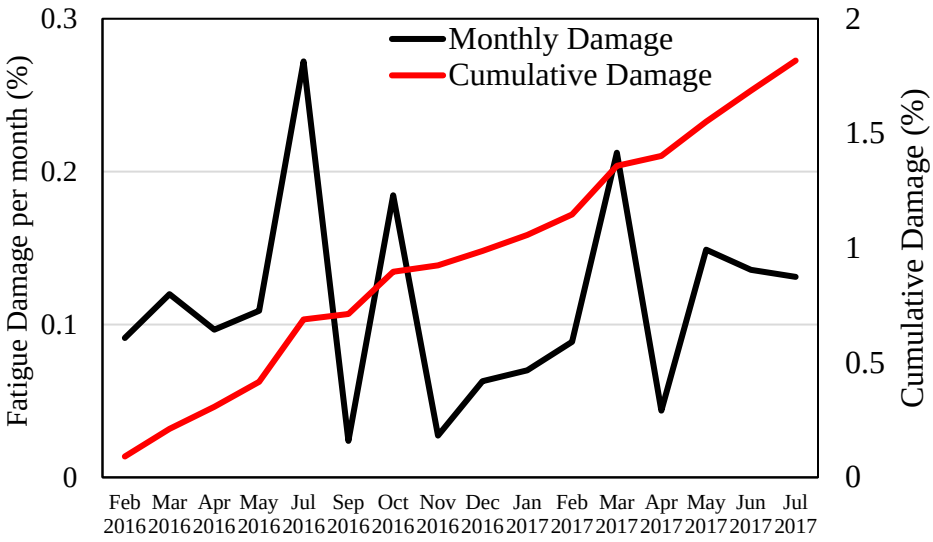

FIGURE 31 Fatigue damage in AC due to class 9 vehicle

Damage shown previously in Figure 14 from FWD is the total damage, which includes combined damage from the traffic and climate. However, cumulative AC damage shown in Figure 31 only shows the damage from class 9 vehicle. The combined damage from all traffic and weather from 2016 and 2017 was around 4.1%. Among this 4.1% of total AC damage, 1.8% is due to the class

9 vehicle only. Therefore, it can be implied that around 44% of the AC layer damage occurred between 2016 and 2017 is due to the traffic; specifically, due to the class 9 vehicle, which is more than 70% of the total traffic count at I-40.

From the above discussion, it can be said that around 45% of the total damage in the AC layer is due to the traffic and 55% of the total damage is caused by the environmental factors. Regardless of the contributing factors, it is important to identify the effect of this total damage on the AC layer. The following section discusses the distresses that have been observed in the I-40 instrumentation section so far.

OBSERVED DISTRESS

All the distresses that are observed in the I-40 instrumentation section until 2019 are either on the shoulder or in the passing lane. None of the distresses such as cracking or rutting are observed in the driving lane. In this report, the transverse cracks in the shoulder have been documented. Most of the cracks that have appeared on the I-40 instrumentation section is transverse cracks (TC), as shown in Figure 32. All of these cracks are on shoulder. Transverse cracks on the I-40 pavement section can be divided into two categories.

- Cracks confined in the shoulder without Open Graded Friction Course (OGFC)
- Cracks confined in the shoulder with OGFC

Previously, most of the transverse cracks fell within the first category, i.e. confined within the shoulder without OGFC, but the number of cracks in the shoulder with OGFC has increased significantly. Right now, most of the transverse cracks have reached the OGFC layer. Some cracks have started propagating into the driving/passing lanes.

A total length of transverse crack of 881 ft were found on March 05, 2018. This is a massive increase of around 660% from the first measured transverse cracks on December 2014. Within a period of four years, the transverse cracks have increased from 116 ft to 881 ft. On Mach 2016, transverse cracks were measured to be around 498 ft. Percent increase in transverse crack length from 2016 to 2018 is around 80%. If we look at the total transverse crack number, we can see that the number of transverse cracks on December 2014 was 19. On April 2015 that number was 34 and now the number is 51. This number of TC has increased to 74 in 2018. I-40 instrumentation shoulder has two different widths. Near the instrumentation site the shoulder width with OGFC is around 185 inch and towards the west of instrumentation site the width is 285-inch. Summary of the transverse cracks in shown in Table 5. Figure 33 shows the present state of transverse cracks at the field.

Figure 33 shows the visual representation of the transverse crack growth over the year. From Figure 33, it can be observed that lots of new transverse cracks have grown in the recent years.

(a) (b)

FIGURE 32 Transverse Cracks on I-40 instrumentation section

TABLE 5 Transverse crack growth over the year

	2018	2016	2015	2014
Total No	74	51	34	19
Total Length (ft)	881	498	282	116
TC with OGFC	43	10	4	0
TC without OGFC	31	41	30	19

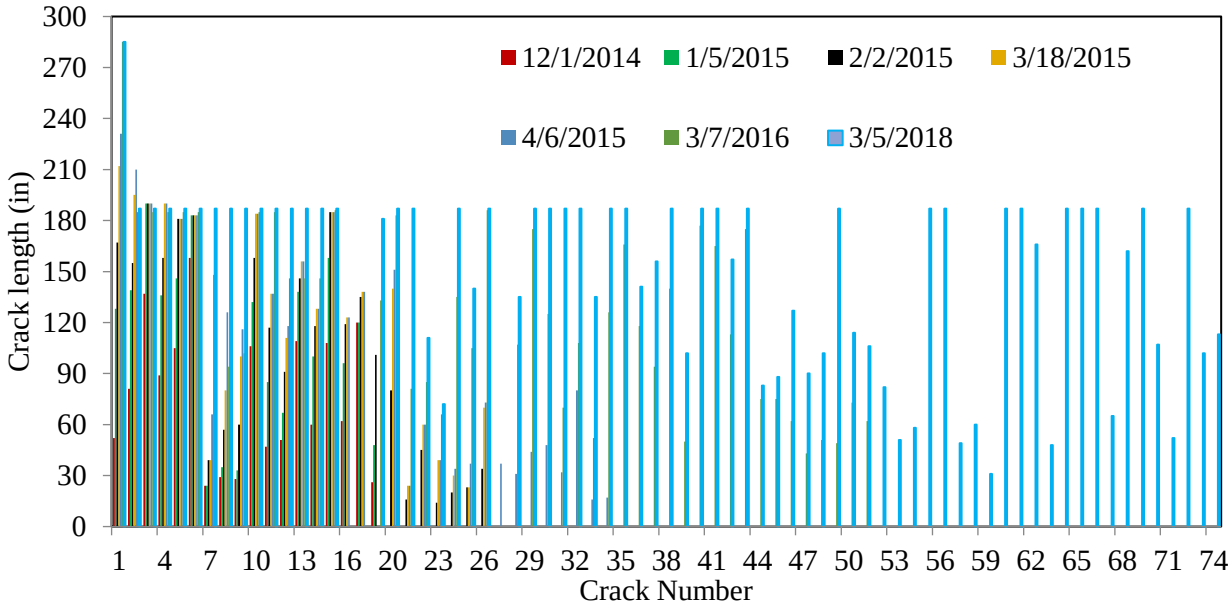

FIGURE 33 Transverse crack growth over the year

Some of the transverse cracks in the shoulder are getting interconnected with each other. These are smaller block cracks. Like other transverse cracks, these block cracks also initiate due to the temperature variation and inability of asphalt binder to accommodate expansion and contraction due to aging *(23)*. Figure 34 shows the propagation of block cracks.

(a) Unmarked

(b) Marked

(c) Block cracks in Number 9

FIGURE 34 Interconnected Transverse Cracks

The width of the transverse cracks is found to vary within a wide range. Some of the cracks have a width close to hairline cracks whereas some transverse cracks have width more than ½ inch. Mostly the transverse cracks that have propagated through the whole shoulder have a width of more than ½ inch. Figure 35 shows the variation of the width of the transverse cracks.

(a) Crack width less than ½ inch

(b) Crack width more than ½ inch

FIGURE 35 Variation of width of the Transverse Cracks

Although most of the documented transverse cracks in this report have propagated throughout the whole width of the shoulder, but they have not propagated inside the main pavement section. However, some of the transverse cracks have been observed in the passing lane, shown in Figure 36.

(a)

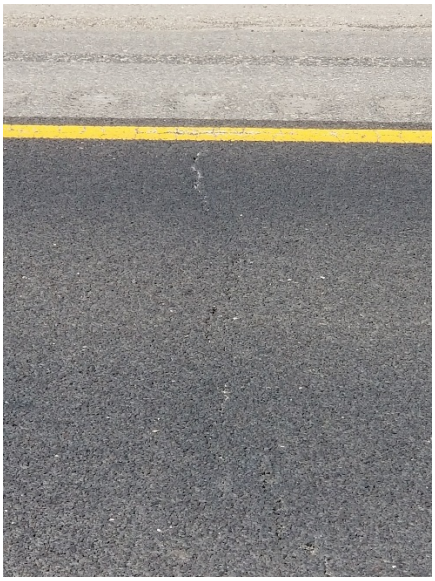

(b)

FIGURE 36 Transverse Cracks in passing lane

Field cores were collected in May 2016 and in July 2018. In the following section, status of the collected AC cores in July 2018 is given. A total of 8 AC cores were collected: seven from the driving lane shoulder and one from the driving lane.

AC Core 1: (Figure 37)

Location: Driving Lane Shoulder near Milepost 140.6

Distress Type: Transverse Thermal Crack

(a)

(b)

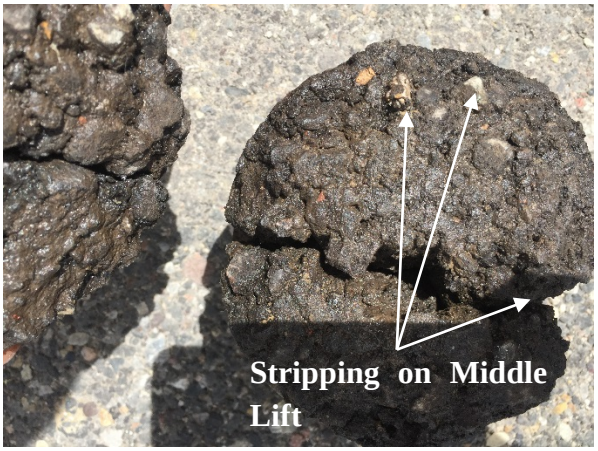

(c)

(d)

FIGURE 37 Cored pic at location 1

Observation: Crack has fully propagated through the first and second lift. Stripping was observed on both top and middle lifts.

AC Core 2: (Figure 38)

Location: Driving Lane Shoulder

Distress Type: Longitudinal Thermal Crack

(a)

(b)

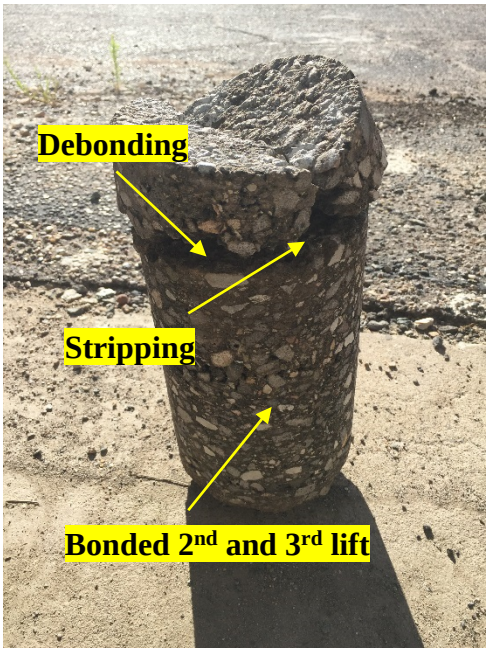

(c)

FIGURE 38 Cored pic at location 2

Observation: Crack has fully propagated to the first lift only. Top two lifts were found to be debonded. Stripping was observed at the bottom of top lift. Due to stripping top lift thickness was only found to be around 2″.

AC Core 3: (Figure 39)

Location: Driving Lane Shoulder

Distress Type: Transverse Thermal Crack

(a)

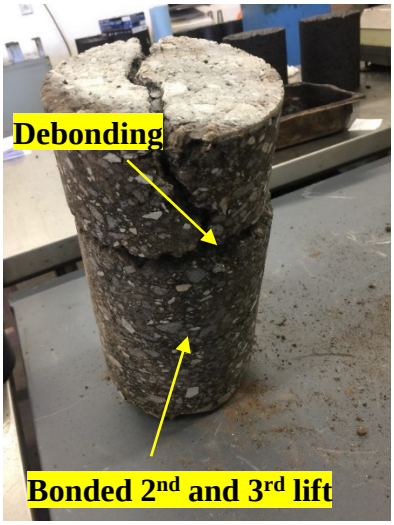

(b)

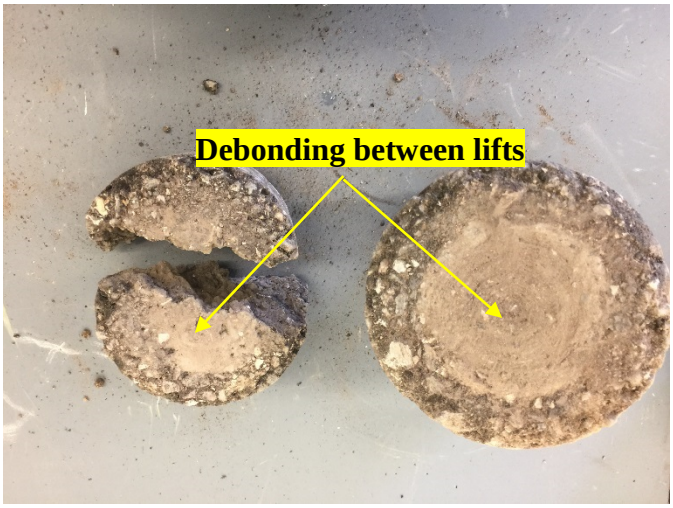

(c)

FIGURE 39 Cored pic at location 10

Observation: Crack has fully propagated through the first lift. Top two lifts were found to be debonded. Second and third lift were bonded together. Stripping was not observed.

AC Core 4: (Figure 40)

Location: Driving Lane Shoulder with OGFC layer

Distress Type: Transverse Thermal Crack

(a) (b)

FIGURE 40 Cored pic at location 7

Observation: Crack has fully propagated through the first AC lift with OGFC. All three AC lifts were found to be debonded. Stripping was not observed.

AC Core 5: (Figure 41)

Location: Driving Lane Shoulder

Distress Type: Transverse Thermal Crack

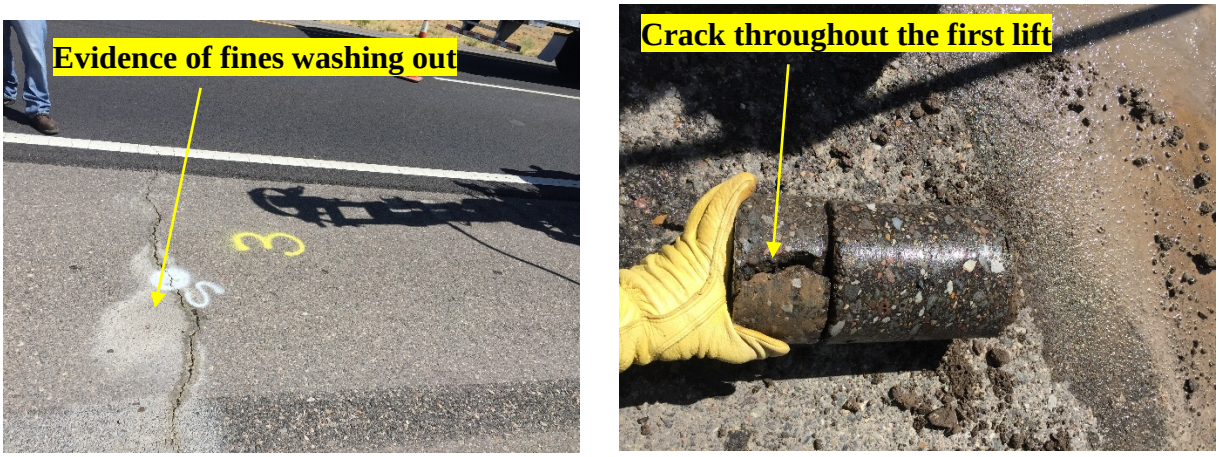

(a) (b)

(c)

FIGURE 41 Cored pic at location 3

Observation: Crack has fully propagated through the first AC lift. Top two lifts were found to be debonded. Second and third lift were bonded together. Stripping was not observed.

AC Core 6: (Figure 42)

Location: Driving Lane Shoulder

Distress Type: Transverse Thermal Crack

(a)

(b)

(c)

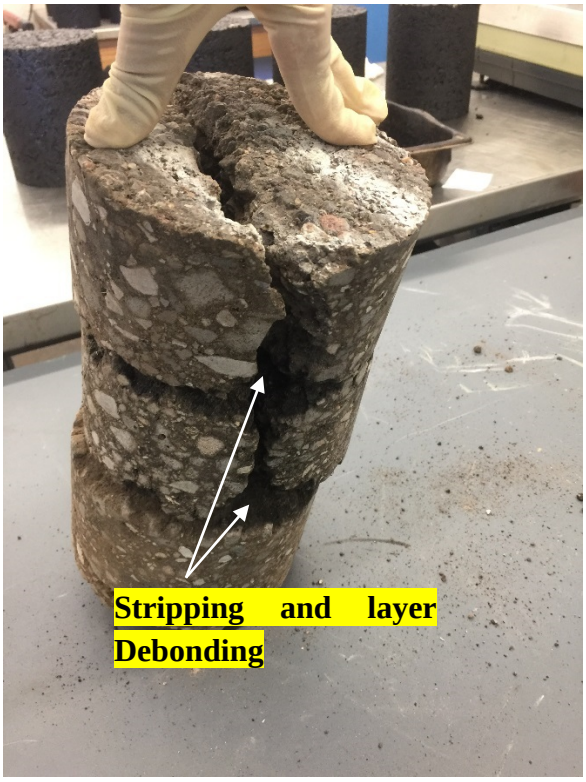

(d)

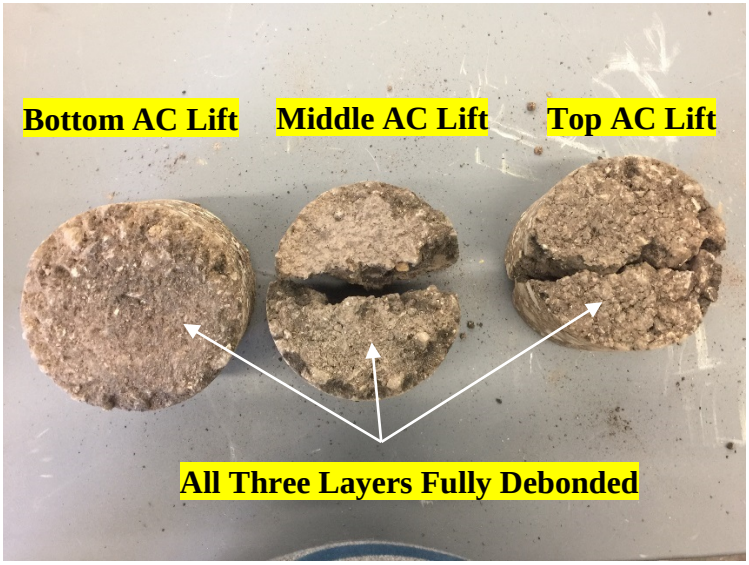

(e)

FIGURE 42 Cored pic at location 12

Observation: Crack has fully propagated through the first and second lift. Stripping was observed on both top and middle lifts.

AC Core 7: (Figure 43)

Location: Driving Lane outside wheel path

Distress Type: No Distress but transverse crack on adjacent shoulder (No propagation of transverse crack in driving lane)

(a)

(b)

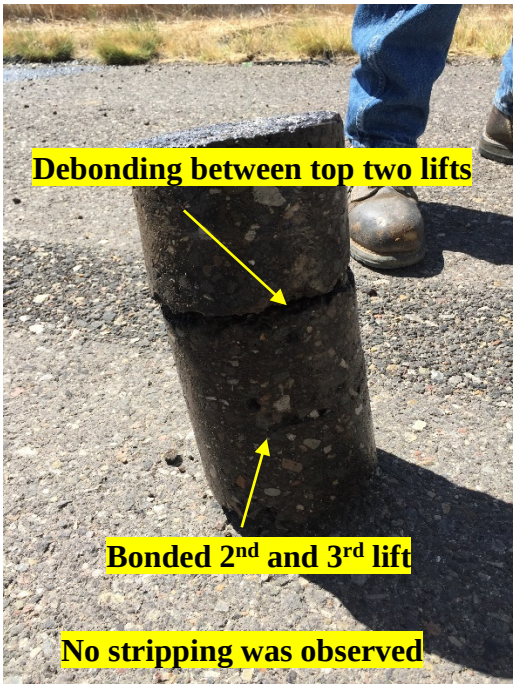

(c)

FIGURE 43 Cored pic at location 11 (Driving Lane)

Observation: Although there was a transverse crack on the adjacent shoulder, but that crack did not propagate to the driving lane. No stripping was observed. Top and Middle lifts were found to be debonded from each other. Middle and bottom lifts were founded to be bonded together.

AC Core 8: (Figure 44)

Location: Driving Lane shoulder

Distress Type: No Distress. Core was collected from comparison purpose.

(a) (b)

FIGURE 44 Cored pic at location 1

Observation: No stripping, cracking nor any layer debonding was observed.

AC Core 9: (Figure 45)

Location: Passing lane

Distress Type: No visible distress.

(a) (b)

FIGURE 45 AC core from passing lane

Observation: No stripping, cracking but top two layers were debonded.

In summary, transverse cracks have appeared on the shoulder and passing lane of the I-40 instrumentation section. Those cracks have not yet propagated into the driving lane. Although there was no cracking in the driving lane, the cores collected from the passing and driving lane, from the locations with no visible distresses, showed delamination, as shown in Figure 43 and Figure 45. It is important to determine when this delamination first occurred. With the embedded sensor response under FWD load, it is possible to identify the time frame when the delamination between the layers might have taken place.

COMPARISON OF STRESSES AND STRAINS

It is important to compare the layered elastic structural response with field measured response. AASHTOWare Pavement ME Design guide uses a linear elastic approach whereas the actual field response may be different. Timm and Priest (2006) used FWD loading data to understand the pavement structural response using layer elastic analysis (LEA). From their study at an National Center for Asphalt Technology (NCAT) test section, they concluded that layered elastic analysis is a reasonable approach for predicting the structural response of a pavement section. Many have used different tools for predicting the structural responses such as KENPAVE, JULEA, AASTHOWare Pavement ME Design Guide for LEA and for finite element analysis (FEA) one can use ABAQUS or ANSYS. The research team want to observe how LEA predicts the structural response under 9000 lbs of FWD test load for the I-40 instrumentation section.

In this report, LEA was used to predict the structural response at the installed sensor locations of the I-40 instrumentation section. Horizontal strain was calculated at the bottom of the asphalt layer located at the 11.125 inches from the pavement surface. Vertical stresses were calculated at the top of the base layer (11.125 inches from pavement surface), bottom of the base (17.125 inches from pavement surface) and in the subgrade (29.125 inches from pavement surface).

KENPAVE and JULEA were used to predict the LEA response of the pavement structure. AASHTOWare Pavement ME Design Guide was not used because it can only predict horizontal tensile strain at 0.5 inches from the top of the pavement surface. As this report tries to compare the measured and predicted pavement response, it is important to compare them at the designated locations of the sensors to be accurate. The reason for using JULEA is that this software is integrated into the ME Design Guide for pavement response calculation.

To obtain the pavement response from any types of loading KENPAVE and JULEA requires modulus of the pavement layers, thickness and Poisson's ratio. Modulus of the layers was given from the FWD backcalculated layer moduli.

To compare the LEA results from KENPAVE and JULEA with field obtained value p-2 norm of the error vector was calculated. The norm of a mathematical object is a quantity that in some (possibly abstract) sense describes the length, size, or extent of the object. A norm of vector $\boldsymbol{x}$ is defined as $\|\boldsymbol{x}\|$. A norm is always positive. In mathematics, there are several norms. For the

comparison purpose in this report, the scaled *p*-2 norm was chosen. Say, the field measured value is in Ψ_f as a vector form and predicted values are in Ψ_p.

$$\psi_f = \begin{bmatrix} \psi_{f1} \\ \psi_{f2} \\ \psi_{f3} \\ . \\ . \\ \psi_{fn} \end{bmatrix} \qquad \psi_p = \begin{bmatrix} \psi_{p1} \\ \psi_{p2} \\ \psi_{p3} \\ . \\ . \\ \psi_{pn} \end{bmatrix}$$

Then scaled *p*-2 norm of these two vectors $\|\boldsymbol{\Psi}\|$ can be defined as

$$\|\psi\| = \frac{1}{n^{1/p}} \left(\sum_{i=1}^{n} \left(\psi_{fi} - \psi_{pi} \right)^p \right)^{1/p} \tag{28}$$

KENPAVE

KENPAVE is a freeware software developed at the University of Kentucky. It gives pavement response, i.e., stress and strain at desired depth inside the pavement under designated load. Steps of calculating stress and strain through KENPAVE is given below briefly:

1) First, the layer properties of the asphalt pavement section and loading have to be defined. This is done through *LAYERINP,* which is shown in Figure 46.

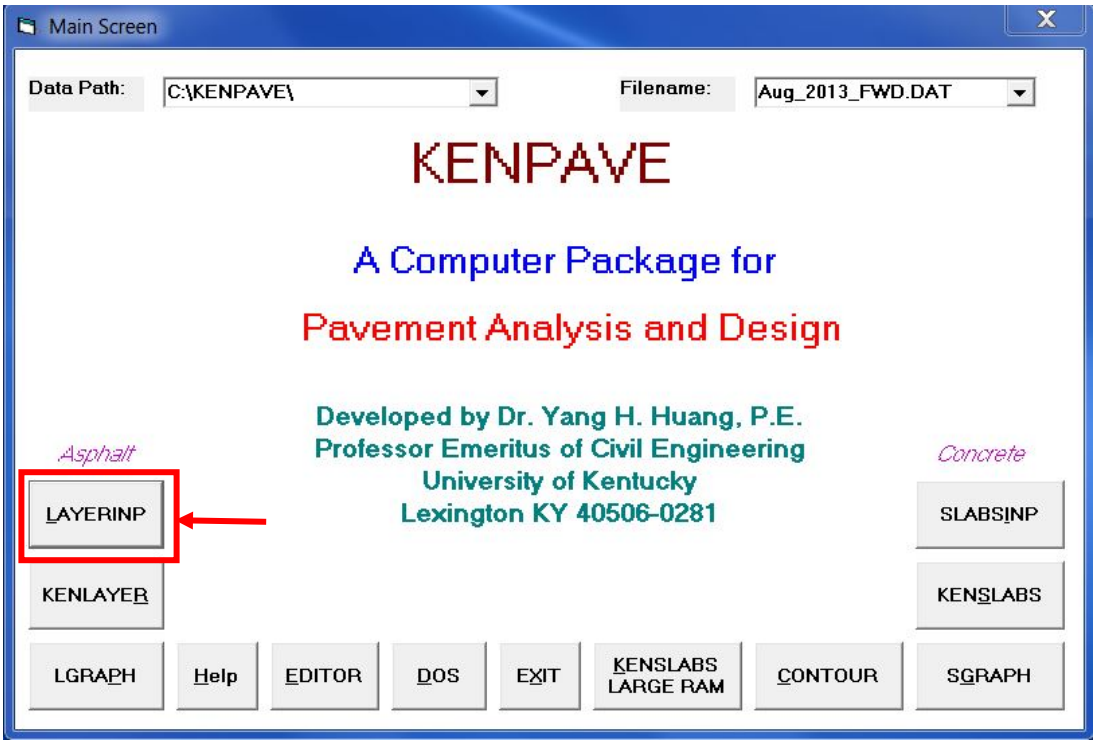

FIGURE 46 KENPAVE main window

2) Figure 47 shows the main menu of the *LAYERINP* option. This is the dialog box where all the parameters have to be defined. Pavement layers, location of desired responses, analysis mode and loading pattern. After all the desired properties have been defined the module is saved and exited.

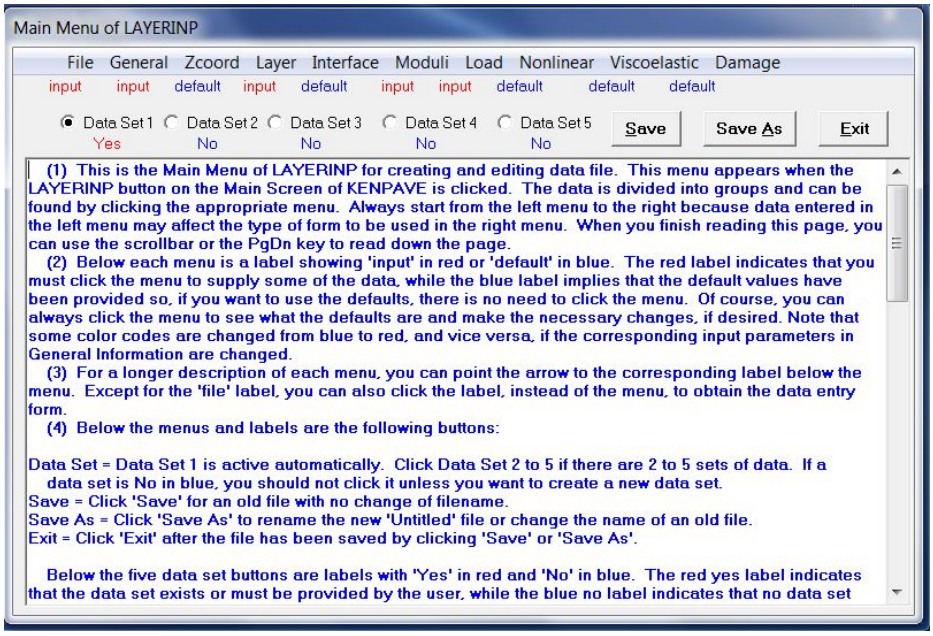

FIGURE 47 KENPAVE later input window

3) *KENLAYER* button on the main screen is pushed to start the analysis. Once done the analyzed file can be opened through *EDITOR* to view the results, which is shown in Figure 48.

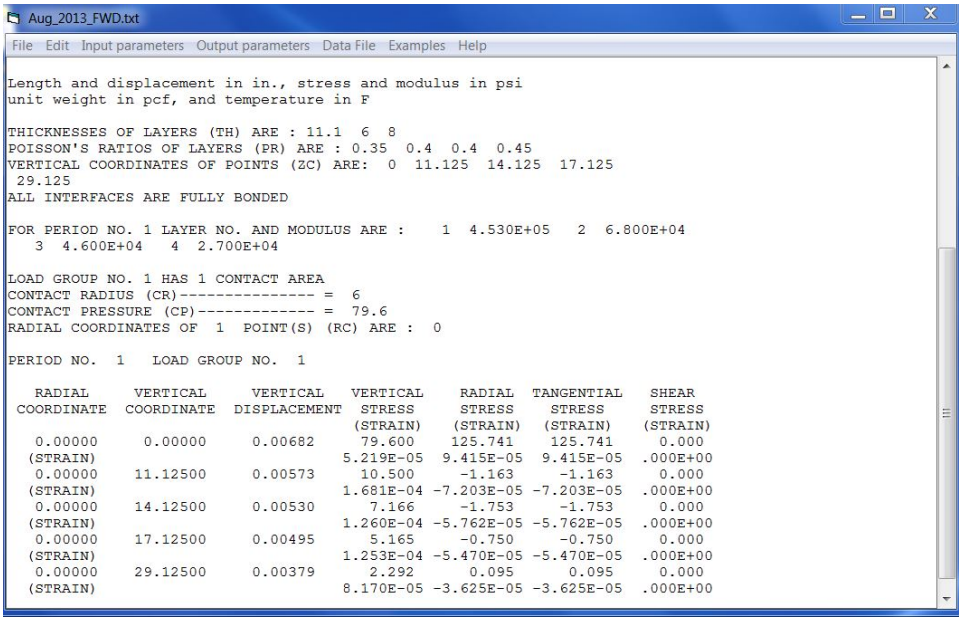

FIGURE 48 KENPAVE analysis result window

JULEA

This is a demo version of the software, which was developed for the AASHTO 2002 design guide and later its algorithm was integrated into the AASTHOWare Pavement ME Design Guide. Steps to calculate pavement response through JULEA was given below briefly:

1) Calculating pavement response through JULEA is more user-friendly than KENPAVE. It uses only linear elastic analysis that is why it is less complex. Figure 49 show the main window of WinJULEA. In the main window layer properties, loading configuration and desired response location have to be defined.

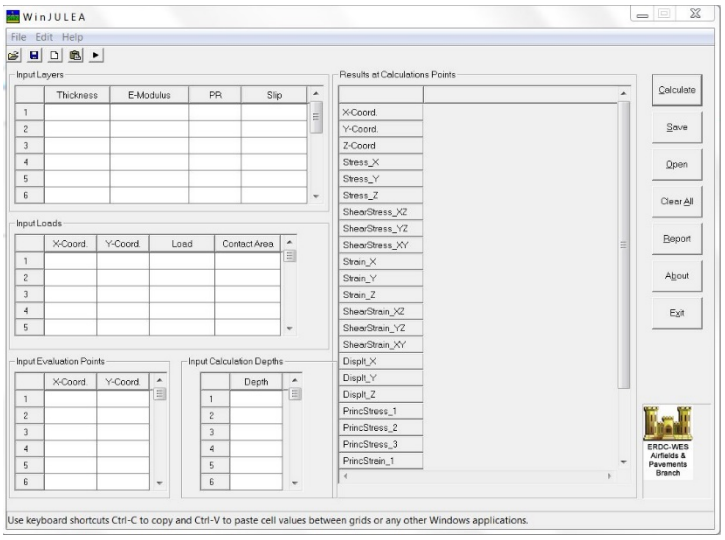

FIGURE 49 WinJULEA main window

2) After the parameters have been entered the run button is pressed to start the analysis. Figure 50 shows the analyzed result output window.

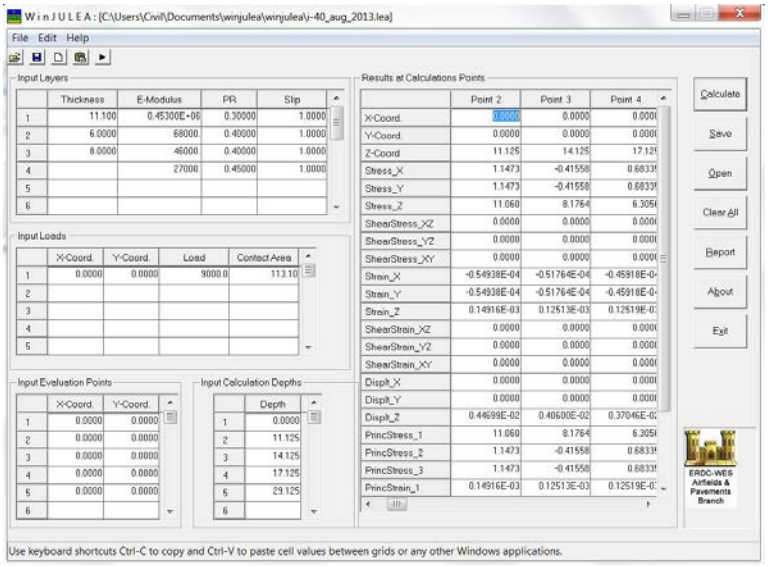

FIGURE 50 Analysis output window

Asphalt Layer Response

In this report pavement response from June 2015 to March 2016 is shown. Some of the months are missing in between them. This is because of the malfunction of the instrumentation site. Figure 51 shows the measured and predicted strain response of the asphalt layer. This figure also shows how the strain response is changing over the year. Strain variation shown in Figure 51 is the average of all the FWD test sequence in a single day. Reported temperatures are also the average pavement surface temperatures for that particular day of that month. The responses shown here are for FWD

test load of 9000 lbs. It can be seen that regardless of the strain calculation technique, strain in increasing from 2013 to 2015 which is evident. From Figure 51 it can be seen that when the pavement is new and stiffness is high, the KENPAVE LEA underpredicts the asphalt layer pavement response. When the pavement is old and the stiffness has reduced, KENPAVE LEA gives a conservative prediction. However, this is true for warmer temperature like summer and fall. When the temperature is cold then LEA underpredicts the asphalt response regardless the pavement is old or new. One other important observation is that for any pavement condition or temperature JULEA, which is the underlying software for AASHTOWare Pavement ME Design Guide, underpredicts the pavement response. From visual inspection, it can be said that KENPAVE LEA predicts asphalt response much better than JULEA. To distinguish among these two LEA packages, scaled *p*-2 norm were taken for both of the LEA packages with the field strain. Scaled *p*-2 norm for KENPAVE was 24.3 whereas for JULEA the value was 55.7. Therefore, it can be said for asphalt response under FWD load KENPAVE is a better option. Table 6 shows the temperature variations along the months where asphalt strains were measured.

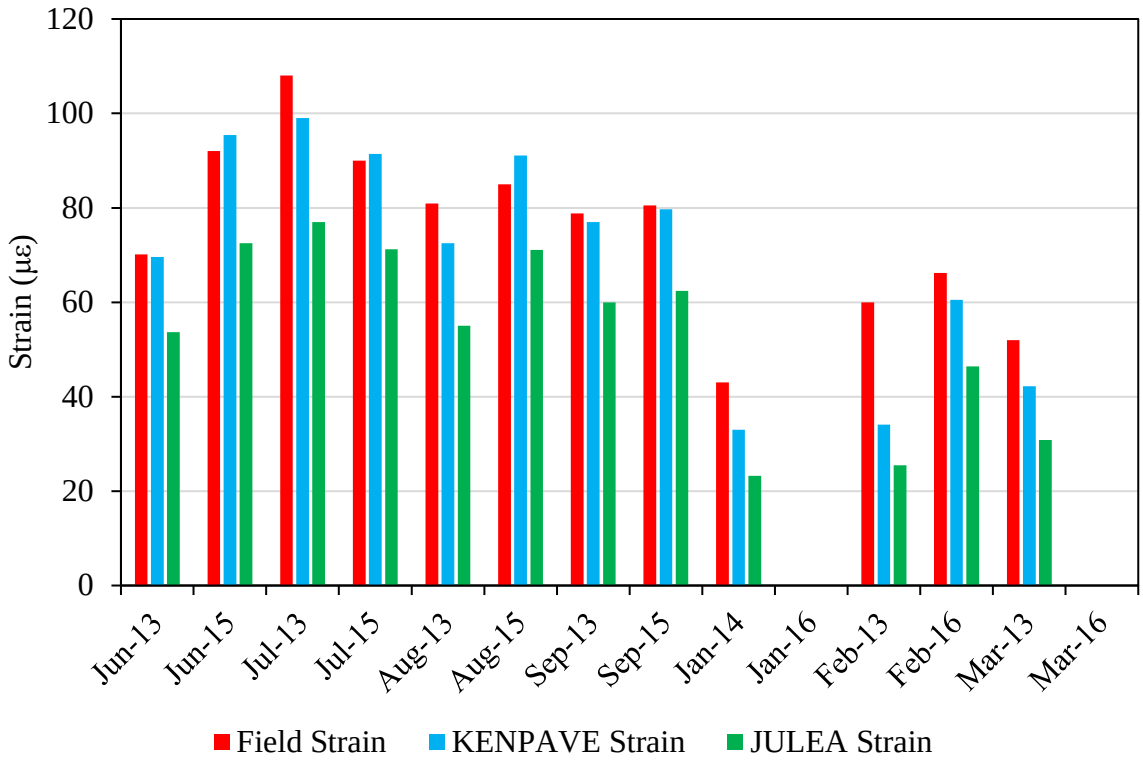

FIGURE 51 Asphalt Layer Strain Variation

TABLE 6 Temperature Variation

Month	Avg Pavement Surface Temp °C
Jun-13	35.9
Jun-15	33.0
Jul-13	41.0

Jul-15	32.0
Aug-13	37.9
Aug-15	29.0
Sep-13	34.5
Sep-15	25.0
Jan-14	7.1
Jan-16	
Feb-13	9.6
Feb-16	8.3
Mar-13	16.6
Mar-16	

Base Layer Response

Earth Pressure Cell (EPC) is installed at the top of the base. Figure 52 shows the measured and predicted stress response of the base layer. This figure also shows how the stress response is changing over the year. Stress variation shown in Figure 52 is the average of all the FWD test sequence in a single day. Reported temperatures are also the average pavement surface temperatures for that particular day of that month. The responses shown here are for FWD test load of 9000 lbs. It can be seen that regardless of the stress calculation/collection technique, stress is increasing from 2013 to 2015 which is evident. During warm weather, for new pavement, LEA overpredicts the stress response much higher than the old pavement. However, during cold weather, regardless of the pavement condition LEA overpredicts the response much higher than the similar prediction in warm weather condition. One important observation from the asphalt response Figure 51 and base response Figure 52 is that during the horizontal strain calculation the LEA packages differ much higher among them than they do during the vertical stress calculation. The scaled *p*-2 norm for base stress variation for KENPAVE and JULEA with measured field base stress was observed to be 13 and 14.

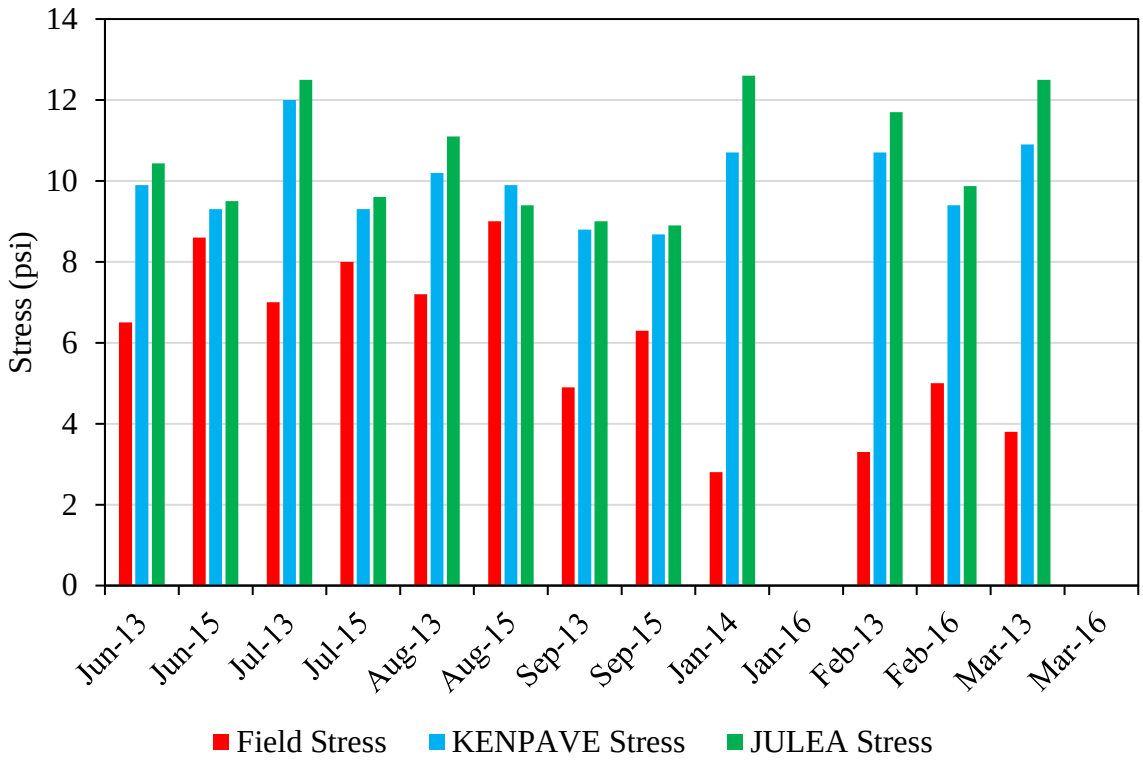

FIGURE 52 Base Stress Variation

PPC Response

EPC is also installed at the bottom of the base or top of the PPC layer. Figure 53 shows the measured and predicted stress response of the PPC layer. This figure also shows how the stress response is changing over the year. Stress variation shown in Figure 53 is the average of all the FWD test sequence in a single day. Reported temperatures are also the average pavement surface temperatures for that particular day of that month. The responses shown here are for FWD test load of 9000 lbs. It can be seen that regardless of the stress calculation/collection technique, stress is increasing from 2013 to 2015 which is evident. During warm weather, for new pavement, JULEA over predicts the stress response than the old pavement whereas KENPAVE under predicts the stress response regardless of the old or new condition. However, during cold weather, indifferent to the pavement condition, LEA over predicts the response much higher than the similar prediction in warm weather condition. One important observation from the asphalt response in Figure 51 and base response in Figure 52 with PPC response in Figure 53 is that LEA packages predicts PPC stress much closely than the other two responses. The scaled *p*-2 norm for PPC stress variation for KENPAVE and JULEA with measured field base stress was observed to be 4.4 and 6.7.

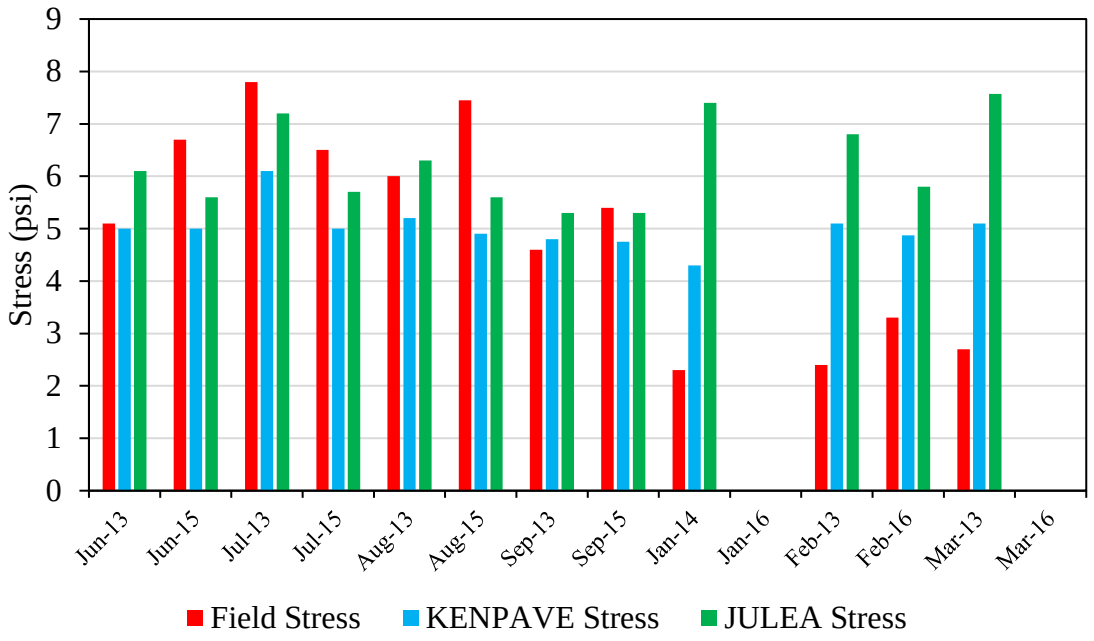

FIGURE 53 PPC Stress Variation

Subgrade Response

EPC is also installed at 4 inches below the top of the subgrade layer. Figure 54 shows the measured and predicted stress response of the subgrade layer. This figure also shows how the stress response is changing over the year. Stress variation shown in Figure 54 is the average of all the FWD test sequence in a single day. Reported temperatures are also the average pavement surface temperatures for that particular day of that month. The responses shown here are for FWD test load of 9000 lbs. It can be seen that regardless of the stress calculation/collection technique, stress is increasing from 2013 to 2015. During warm weather, for new pavement, JULEA overpredicts the stress response than the old pavement whereas KENPAVE underpredicts the stress response regardless of the old or new condition. However, during cold weather, indifferent to the pavement condition, LEA overpredicts the response much higher than the similar prediction in warm weather condition. It is interesting to note that the stress prediction trend of subgrade in Figure 54 is almost similar to what observed for PPC stress prediction in Figure 53. The scaled *p*-2 norm for subgrade stress variation for KENPAVE and JULEA with measured field base stress was observed to be 1.7 and 2.57.

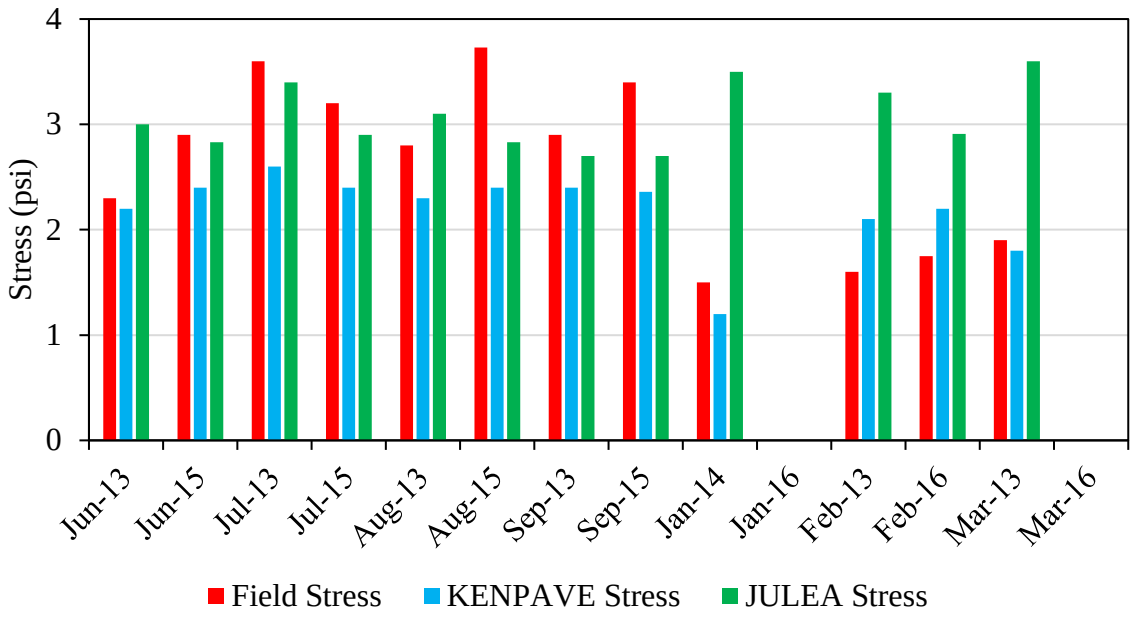

FIGURE 54 Subgrade Stress Variation

Discussion

Based on the above study, the following remarks can be made:

- Stress-strain response from the field instrumentation was compared with the layer elastic analysis software. KENPAVE and JULEA were used for the comparison purpose. Algorithm from JULEA was used in the AASTHOWare ME Pavement Design Guide. That is why JULEA was used. From the results of field horizontal strain in the asphalt layer, it was found that KENPAVE gives better response than JULEA for layer elastic analysis. For the analysis time frame, it was observed that JULEA always under predicts asphalt horizontal strain.
- For stress in the base layer it was found that KENPAVE and JULEA always over predict the base stress response. The over prediction rate is much higher in winter time than in warmer weather conditions. Moreover, when the pavement is new the over prediction rate is also higher. However, with time, as the pavement ages, the over prediction rate attenuates.
- For PPC and subgrade layer it was observed that the LEA software under predicts the stress in warmer weather condition and over predicts in colder temperature.

ENERGY DISSIPATION TIME

The Area under the FWD load-deflection curve or the stress-strain at the bottom of the HMA layer can be used to predict the deterioration of the pavement. Previous researchers have observed that the energy under the FWD load-deflection curve has a correlation with the pavement distress *(25–27)*. Only distress that was observed in the driving lane of the instrumentation section is the

delamination of the top two layers. From traditional FWD backcalculation alone it is not possible to identify when the pavement layers got delaminated. However, FWD data combined with the instrumentation response it is possible to determine when the top two layers got delaminated.

Toughness is the ability of a material to absorb energy and deform plastically before fracturing. Toughness can also be viewed as the energy absorbed by the material per unit volume. Toughness is calculated by integrating the area under the stress-strain curve, as shown in Figure 55.

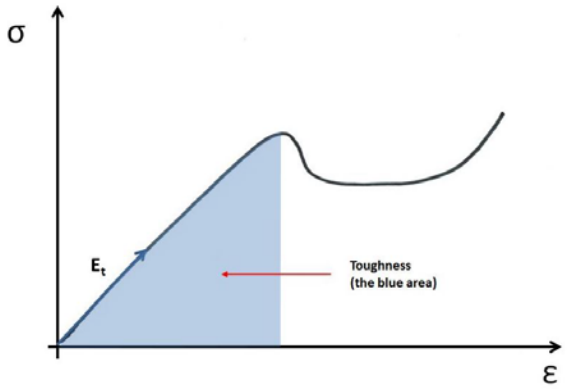

FIGURE 55 Stress-Strain Diagram

Mathematically, the expression of toughness can be written as Eq. (29),

$$\text{Toughness (energy/unit volume)} = \int_0^{\varepsilon_f} \sigma d\varepsilon \tag{29}$$

It is possible to obtain the stress-strain diagram of AC layer under controlled FWD loading from the embedded sensor. Let us consider a stress block, as shown in Figure 56**,** under FWD load in AC layer. The stress block in Figure 56 is situated directly under the FWD loading plate, thus, the stresses are principal stresses and the shear stress-strain components are zero.

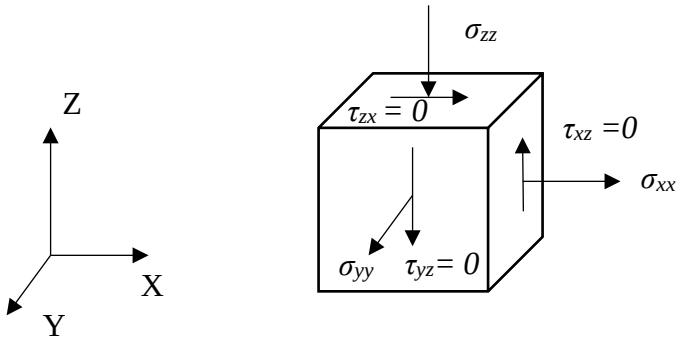

FIGURE 56 A Stress Block

In Figure 56, σ_{zz} and ε_{xx} can be obtained from the EPC and strain gage installed at the bottom of the AC layer. Assuming isotropic linear elastic behavior of AC and, stress-strain components of the stress block can be obtained using Eq. (30):

$$\left.\begin{aligned}\varepsilon_x &= \frac{1}{E}[\sigma_x - \nu(\sigma_y + \sigma_z)] \\ \varepsilon_y &= \frac{1}{E}[\sigma_y - \nu(\sigma_z + \sigma_x)] \\ \varepsilon_z &= \frac{1}{E}[\sigma_z - \nu(\sigma_x + \sigma_y)]\end{aligned}\right\} \quad (30)$$

Here, in Eq. (30), *E* is the modulus of the AC layer obtained from FWD. It is also assumed that stress-strain is the same in both the transverse and radial direction of AC.

Input energy by the FWD load can be calculated from the load-displacement curve. When a FWD load is applied on the pavement, the responses are obtained by the geophones. A plot of the load-displacement curve is shown in Figure 57. Once integrated, the plot of Figure 57 gives FWD input energy. Figure 58 shows the stress-strain diagram of AC layer in the vertical direction.

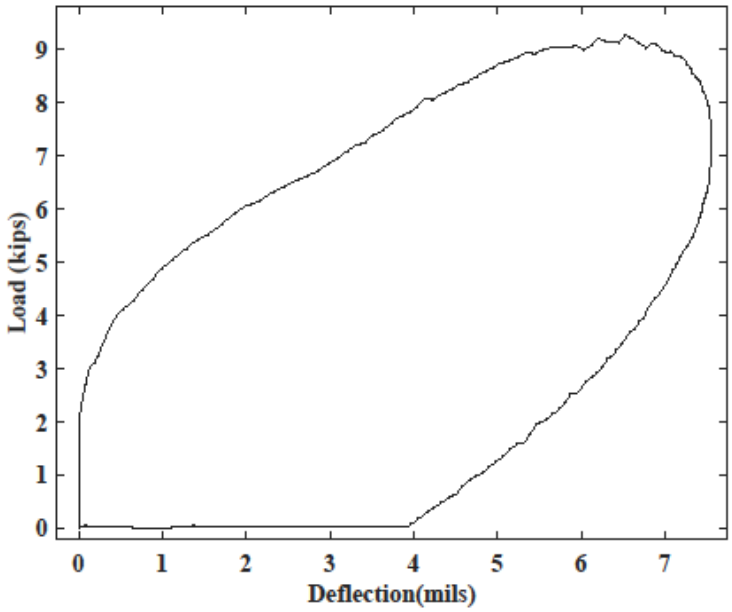

FIGURE 57 Load Displacement curve under FWD 9-kip load

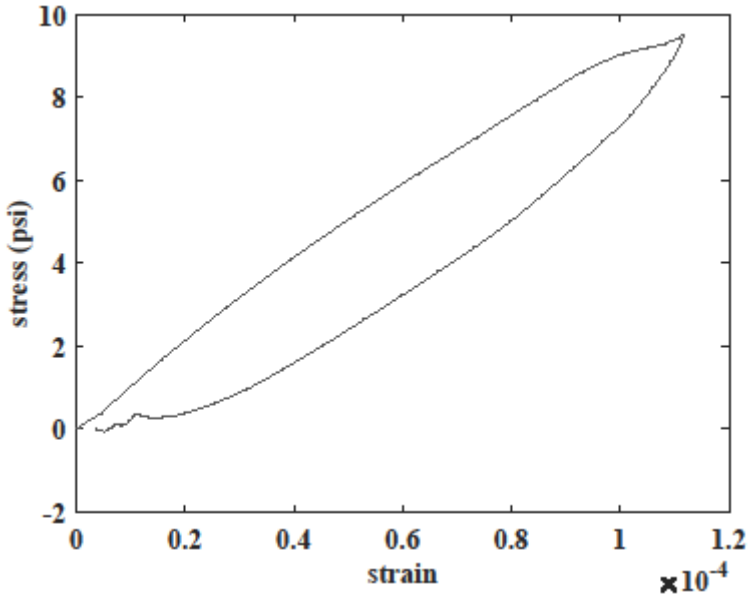

FIGURE 58 Stress-Strain curve of AC in the vertical direction under FWD 9-kip load

Using the Eq. (31) and the embedded sensor data from EPC and strain gage, it is possible to obtain the stress-strain plot of AC layer. Integration of the stress-strain graph gives toughness, as shown in Figure 58**.** The unit of toughness is energy per unit volume. As the integration of load-deflection graph from FWD only gives energy, thus, it needs to be divided by an appropriate volume for meaningful comparison with the stress-strain data from the embedded sensor. Energy per unit volume from the FWD load-deflection curve was obtained using the following equation:

$$\text{FWD input Energy per unit volume} = \frac{\text{FWD input energy}}{\text{area of FWD loading plate} \times \text{depth to bed rock}} \quad (31)$$

Figure 59 shows the response of the horizontal axial strain gages at the bottom of the HMA layer under the 9-kip FWD standard load. The horizontal axis is time in milliseconds and the vertical axis is volt readings of the strain gages. The vertical readings of the volts are multiplied with the calibration factors to obtain the corresponding strain readings. Therefore, if the area under this curve is integrated, we obtain the time required to dissipate this energy. The area is base times height. As height is strain, and it does not have any unit, and base has the unit of time, therefore, the area gives us the energy dissipation time.

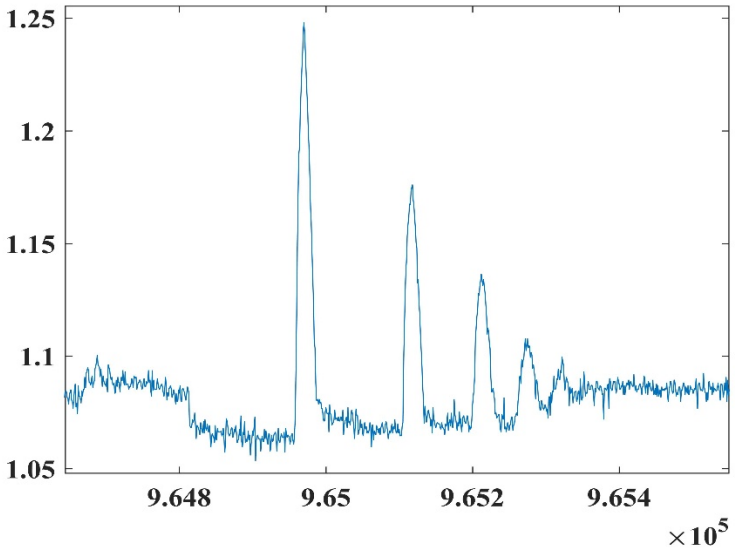

FIGURE 59 Horizontal Axial Strain Gage Response

Area (unit of time) = Base (unit of time) × Strain (unit less)

This report shows the variations in input and output energy per unit volume for the AC layer from 2013 to 2019 in extreme temperature conditions such as the highest and lowest temperature of a given year.

Data Analysis

Table 7 shows the energy variation for the FWD 9-kip test load. For ease of discussion, a visual representation of a portion of the Table 7 is shown in Figure 60.

TABLE 7 Energy analysis of AC layer under FWD

Month	Average AC Temperature (°C)	Toughness (in-lb/in^3)			% Absorbed Vertical	% Absorbed Radial	Area Under Strain Time (mili-Sec)
		FWD	Vertical	Radial			
Feb-13	9.6	9.25E-04	6.02E-05	3.03E-05	6.5	3.3	742.02
Jul-13	41	1.32E-03	6.11E-05	2.38E-05	4.6	1.8	1902.79
Jan-15	-1	7.76E-04	1.23E-05	2.68E-05	1.6	3.4	663.92
Jun-15	34	1.25E-03	5.06E-04	1.91E-04	40.3	15.2	1962.22
Feb-17	7.8	8.80E-04	1.22E-04	7.70E-05	13.8	8.7	1160.73
Jul-17	33	1.11E-03	3.90E-04	1.10E-04	35.3	10.0	2421.82
Jan-18	2	7.83E-04	5.79E-05	4.51E-05	7.4	5.8	679.65
Jul-18	29.3	1.13E-03	1.67E-04	1.01E-04	14.7	8.9	2034.83
Feb-19	3.5	9.30E-04	1.01E-04	5.69E-05	10.9	6.1	842.63

From Figure 60, it can be observed that input FWD energy per unit volume at the pavement surface decreases slightly over time from 2013 to 2019. However, this decrement in input FWD energy per unit volume is due to the decrease in temperature. On July 2013, average pavement temperature was around 41°C and the corresponding input FWD energy per unit volume at the pavement surface was around 1324×10^{-3} in-lb/in^3. Five years later, in July 2018, the value decreased to 1130×10^{-3} in-lb/in^3 due to the decrement of temperature to 29.3°C. Contrast to the input FWD energy per unit volume at the pavement surface, energy per unit volume at the bottom of the AC layer varied at a higher rate over time. In the beginning, after the construction of the instrumentation section, the amount of energy absorbed by the AC layer was relatively low, less than 5% of the input FWD energy per unit volume. However, there is a significant increase in absorbed energy by the AC layer in July 2015; around 40% of the input FWD energy per unit volume was absorbed. This sudden increase in absorbed energy is observed in both vertical and radial direction. After July 2015, the value of the energy per unit volume in the AC layer decreased from July 2015 value of 506×10^{-3} in-lb/in^3. However, energy per unit volume of the AC layer never returned to the state where it was immediately after the construction. Thus, this sudden increase of absorbed energy in the AC layer may have been due to some sort of damage. Studies conducted by Ayyala et al. (2018) and Von Quintus and Killingsworth (1998) have shown that after the construction there is a slight decrease in the AC layer energy per unit volume, but AC energy per unit volume increases due to the presence of distresses. They performed their study with the FWD load-deflection curve alone. FWD load-deflection curve does not reveal much information in the context of the AC layer delamination at the I-40 instrumentation section. However, studying the stress-strain data from the embedded sensor under the FWD 9-kip load, it can be observed that there is a sudden increase in absorbed energy by the AC layer. As there is no cracking or rutting present in the driving lane of the instrumentation section, thus, it can be stated that the increase in absorbed energy by the AC layer is due to the delamination of the AC layers. Therefore, based on the observed distresses from the field cores and embedded sensor instrumentation data, it can be said that the delamination of the AC layers occurred in the summer of 2015.

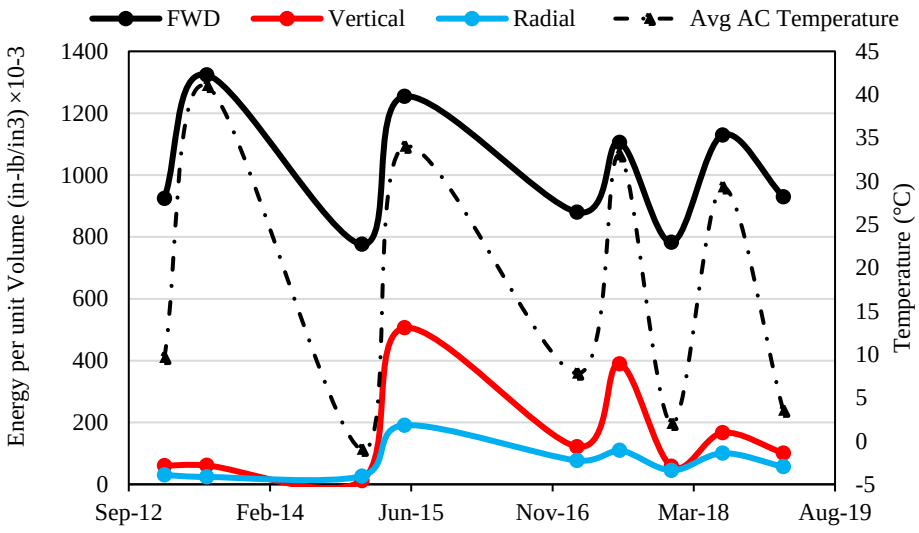

FIGURE 60 AC layer energy per unit volume variation with time

Dissipation time is the area under the strain curve as shown in Figure 61. Like the discussion in previous section, dissipation time is slightly increasing over time. This increment of dissipation time of AC strain gage from 2012 to 2018 suggests that distress is also increasing over time in the AC layer.

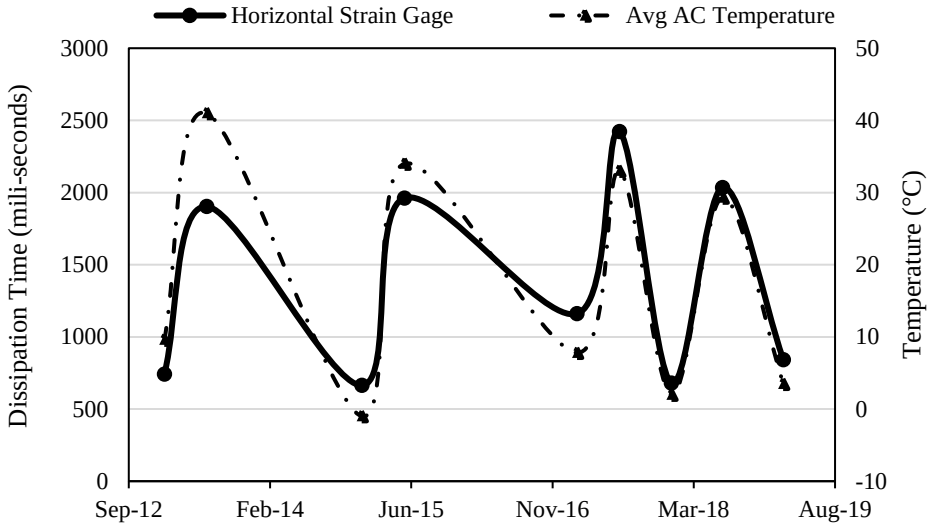

FIGURE 61 AC layer strain dissipation time variation over the years

Discussion

Based on the above discussion, it can be said that the delamination in the driving lane of the AC layers first started to occur in the summer of 2015.

PAVEMENT RESPONSE FREQUENCY

The Fourier transform is very powerful computational tools for analyzing data across engineering applications, including Fourier analysis for signal processing. Fourier transform of a time domain signal *f(t)* can be expressed as *f(ω)* in frequency domain in the following way, as shown in Eq. (31):

$$f(\omega) = \int_{-\infty}^{+\infty} f(t) e^{-i\omega t} dt$$
$$e^{-i\omega t} = \cos(\omega t) - i \sin(\omega t) \quad (32)$$

The above equation is true for a continuous signal. However, in modern world, all the signals are discrete in the time domain. Therefore, discrete Fourier transformation (DFT) can be used to determine the frequency content.

$$f[m] = \sum_{n=0}^{N-1} f[n] e^{\frac{i2\pi mn}{N}}, \qquad m = 0, 1, 2, 3\ldots\ldots\ldots, N-1 \tag{33}$$

In Eq. (33), N is the number of the data point in the signal. FFT is an algorithm which facilitates the computation of the DFT signal and thus, obtain the frequency information from the time domain signal.

Data Processing

For the study in this report, four months of data have been analyzed to obtain the predominant frequency content under the FWD loading at different depths inside the pavement. From 2015, February and June were chosen to compare with the 2016 data of the month of February and July. June 2016 was not used in the comparison as the data was not recorded due to an unknown technical difficulty. For comparison of frequency under the actual traffic loading, traffic data of July 2015 and February 2016 was used. The reason for choosing June/July and February is to compare the frequencies in different seasonal condition. February represents the winter condition and June/July represents the summer condition.

However, FFT could not be directly applied to the field obtained data. Field obtained strain data has lots of noise in it. The amount of noise is so much that it made the base an almost inclined line. In FFT, the length of the signal is very important. Therefore, it is imperative that we apply some post-processing on the field obtained data. From Figure 62, it can be observed that the raw strain gage data has an inclined base and a significant noise. It would give an erroneous result if FFT is directly applied to this data set.

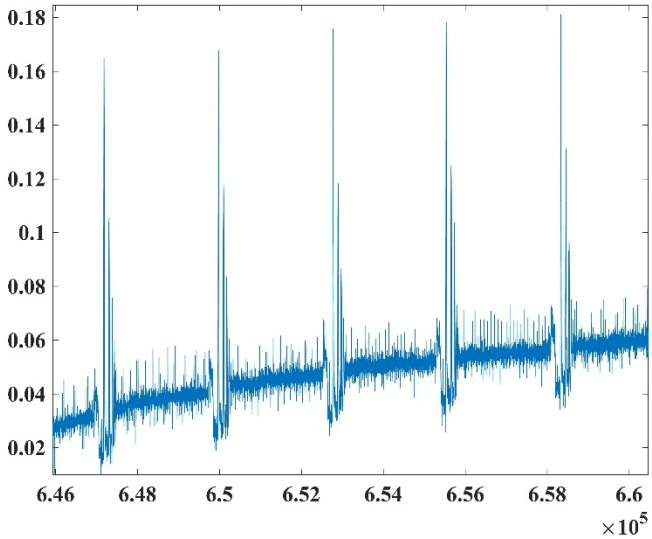

FIGURE 62 Raw strain gage data

Moreover, different channels (sensors) have different inclination and signal to noise ratio. Therefore, to compare the results from different sensors it is important that all the sensors data are shifted to a common base. An algorithm was written in MATLAB to detrend the data. Detrending means removing any preexisting feature or pattern from the data. For this instance, it is making

the base horizontal and shifts it to zero, if not already. From Figure 62, it can be observed the horizontal axis of the data intersects the vertical axis in between 0.02 and 0.06. After detrending, filtering was applied to remove the noise from the data. The median filter is a common choice to remove noise from data, but that filter distorts the data and removes high-frequency contents from the signal. To keep the distortion to a minimum and to increase the signal to noise ratio Savitzky-Golay filter is used *(28)*. It fits low degree polynomial between the successive blocks of the data by the method of linear least squares. After data processing, the signal looked like Figure 63.

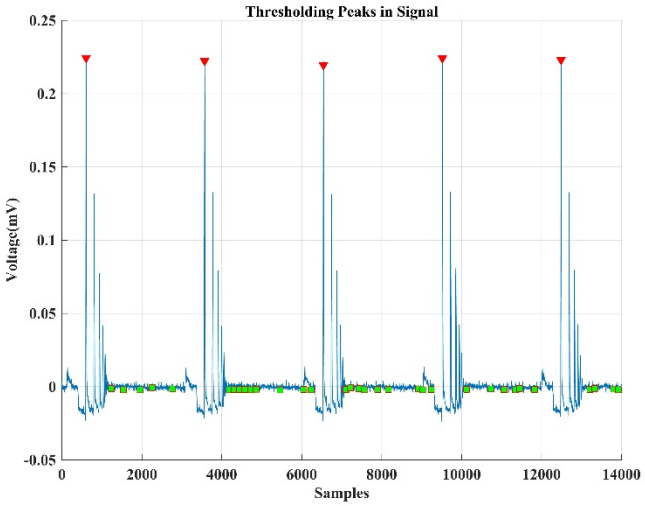

FIGURE 63 Processed data

This method was applied to all the data from different sensors for the previously designated months. Now a random peak was selected for the Fast Fourier analysis to identify the dominant frequency content.

Frequency under FWD load

FWD test is conducted on the I-40 instrumented section each month on designated locations since 2012. In some the locations where the test is conducted, sensors are embedded. Sensors range from strain gages at the bottom of the asphalt and earth pressure cells at the top of base, subbase, and subgrade. On the field obtained data under FWD test Fourier transformation is applied. The Dominant Frequency (DF) under the FWD load for the month of February 2016 is given below in Table 8.

TABLE 8 Dominant Frequency Content (DF) for February under FWD test load

Location	frequency (Hz)
Bottom of HMA	8.33
Top of Base	8.33
Top of Sub-base	8.33
Top of Subgrade	8.33

In I-40 instrumentation section the HMA layer is 11.1 inches thick. There is a 6-inch base on top of an 8-inch subbase layer. From Table 8, when the 9-kip load is applied on top of pavement surface, a DF value of 8.33 Hz is obtained at the bottom of HMA layer at the strain gages. It can be also be seen that the same DF value is observed for subsequent layers under the HMA. Depth and temperature or moisture of the subsequent layers do not have any effect on the DF value. The reason may be the length of time required to transfer the applied load. Regardless of the increment of depth, the time required to transfer the load through each layer is the same.

A similar observation was found for DF value under the FWD test load for June 2015. The dominant frequency content (DF) under the FWD load for the month of June 2015 is given below in Table 9.

TABLE 9 Dominant Frequency Content (DF) for June under FWD test load

Location	frequency (Hz)
Bottom of HMA	7.3
Top of Base	7.1
Top of Sub-base	7.1
Top of Subgrade	7.1

From Table 9, when 9-kip load is applied on top of the pavement surface, a DF value of 7.3 Hz is obtained at the bottom of the HMA layer at the strain gages. It can also be seen that almost the same DF value is observed for subsequent layers under the HMA. Depth and temperature or moisture of the subsequent layers do not have any effect on the DF value. The reason may be the length of time required to transfer the applied load. Regardless of the increment of depth, the time required to transfer the load through each layer is almost the same.

From Table 8 and Table 9, it can be observed that there is a slight difference in the observed DF value. In February 2016, the DF value was higher than what was observed for June 2015. The reason may be the temperature difference in those months. In colder temperature, asphalt pavement becomes stiff, therefore, it will transfer load quicker than it would in the warmer temperature. Hence, a higher DF value is observed for February.

Frequency under Traffic Load

The response of the pavement under the actual traffic loadings are also obtained through the embedded sensors. Pavement response from different vehicle class is recorded by the sensors. However, for comparison purpose, it is ideal to look at the pavement response under a certain vehicle class. For this study, DF under class 9 vehicle will be compared for the different climatic condition. The dominant frequency content (DF) under the FWD load for the month of February 2016 is given below in Table 10.

TABLE 10 Dominant Frequency (DF) for February under class 9 vehicle

Location	Vehicle frequency (Hz)	Tandem frequency (Hz)

Bottom of HMA	5.8	7.143
Top of Base	2.86	5.88
Top of Sub-base	2.81	5.56
Top of Subgrade	2.74	4.35

From Table 10, two different DF values are obtained depending on whether the whole vehicle response or tandem axle response is used in the calculations. When tandem axle response is used, DF value is seemed to be decreasing with depth contrary to what observed under FWD loading. The highest value of DF, 7.143 Hz, is obtained for the bottom of HMA and the lowest value of DF, 4.35 Hz, is obtained for the top of the subgrade. However, when the whole vehicle response is used for DF calculations, it can be observed that the DF value has decreased from what is observed from tandem axle calculation. The reason is the whole vehicle will have a longer response time than compared to only tandem axle response time. However, an interesting observation is that for whole vehicle response, the highest DF is obtained for the bottom of HMA and almost the same DF value is obtained for the unbound layers.

The dominant frequency content (DF) under the FWD load for the month of June 2015 is given below in Table 11.

TABLE 11 Dominant Frequency (DF) for June under class 9 vehicle

Location	Vehicle frequency (Hz)	Tandem frequency (Hz)
Bottom of HMA	5.88	7.143
Top of Base	2.89	5.88
Top of Sub-base	2.85	5.56
Top of Subgrade	2.78	4.35

From Table 11, two different DF value is obtained depending on whether the whole vehicle response or tandem axle response is used in the calculations. When tandem axle response is used, DF value is seemed to be decreasing with depth contrary to what observed under FWD loading. Highest value of DF, 7.143 Hz, is obtained for the bottom of HMA and the lowest value of DF, 4.35 Hz, is obtained for the top of the subgrade. However, when the whole vehicle response is used for DF calculations, it can be observed that the DF value has decreased from what is observed from tandem axle calculation. The reason is the whole vehicle will have longer response time than compared to only tandem axle response time. However, an interesting observation is that for whole vehicle response highest DF is obtained for the bottom of HMA and almost the same DF value is obtained for the unbound layers.

From Table 10 and Table 11, it can be observed that DF value for June 2015 and February 2016 are almost identical. However, it cannot be conclusively said from this results that there is no difference in the DF value in winter and warmer weather as seen from the DF value from the FWD

test results. It is worth mentioning that FWD results under 1000 Hz frequency and vehicular loadings are obtained through 100 Hz sampling frequency. Therefore, the slight variation in the DF value was captured under FWD test loads rather than vehicular loadings. The comparison between the whole vehicle and the tandem axle is important to have an idea of the value of DF the pavement system is subjected to under different loading conditions.

Importance of DF

Dynamic modulus testing is done at different frequencies and temperature to determine the master curve. MEPDG uses the value of frequency determined through Eq. (21) for various vehicle speed. Therefore, it is important to identify the frequency of the pavement under different loading conditions. FWD testing simulates the pavement response a vehicle speed of 50 – 60 mph. Therefore, for a vehicle traveling at 55 mph with 120 psi tire pressure and with the modulus of the respective layers, using Eq. (21) frequency can be obtained. For example, for a class 9 vehicle, what is the frequency for different layers of pavement for the month of June 2015 can be compared with field obtained frequency under the FWD test. Comparison of the DF for the month of June 2015 is given in Table 12.

TABLE 12 Comparison of DF for June 2015 under FWD test load of 9 kip

ME Speed (mph)	Location	FWD Modulus (ksi)	ME Time (s)	ME frequency (Hz)	Field frequency (Hz)
55	Bottom of HMA	400	0.08	12.89	7.3
	Top of Base	45	0.09	10.77	7.1
	Top of Sub-base	32	0.11	9.00	7.1
	Top of Subgrade	24	0.14	7.36	7.1

From Table 12, it can be observed that for a class 9 vehicle traveling at 55 mph in June 2015, the frequencies calculated by MEPDG using Eq. (21) decreases with depth. However, in actual field data under FWD test load, no change in frequencies is observed. Field obtained frequencies under the FWD test load of 9 kip remains almost the same for every pavement layer. Moreover, it can be observed that ME software overestimates the DF. For HMA layer, the DF value differs 77% between ME calculated and field obtained value. For base, subbase and subgrade layer ME software overpredicts the DF by 52%, 27% and 4%. Comparison of the DF for the month of February 2015 is given in Table 13.

TABLE 13 Comparison of DF for February 2015 under FWD test load of 9 kip

ME Speed (mph)	Location	FWD Modulus (ksi)	ME Time (s)	ME frequency (Hz)	Field frequency (Hz)

55	Bottom of HMA	700	0.09	11.16	8.33
	Top of Base	83	0.11	9.23	8.33
	Top of Sub-base	75	0.13	7.55	8.33
	Top of Subgrade	25	0.16	6.34	8.33

From Table 13, it can be observed that for a class 9 vehicle traveling at 55 mph in February 2015, the frequencies calculated by MEPDG using Eq. (21) decreases with depth. However, in actual field data under FWD test load, no change in frequencies is observed. Field obtained frequencies under the FWD test load of 9 kip remains almost the same for every pavement layer. Moreover, it can be observed that the ME software overestimates the DF for HMA and base layer and underpredicts for subbase and subgrade layer. For HMA layer, the DF value differs 34% between ME calculated and field obtained value. For the base, subbase and subgrade layer ME software differs with field measured DF by 11%, -9% and -24%.

Similar comparisons can be made between ME obtained frequency and frequency under actual traffic load. Moreover, comparison of the actual traffic speed and ME simulated traffic speed can also be made from the obtained data. In I-40 instrumentation section sensors are located at different distances and at different depths. For example, earth pressure cell (EPC) at base and subgrade are 20 feet apart from each other. Therefore, if the time difference of the EPC responses at those two sensors for a vehicle is known then the velocity can be obtained using *distance = velocity* $\times$ *time*. Comparison of the DF for the month of June 2015 is given in Table 14.

TABLE 14 Comparison of DF for June 2015 under class 9 vehicle

Location	ME Speed (mph)	Actual Speed (mph)	ME frequency (Hz)	Field frequency (Hz)
Bottom of HMA	55	70	12.89	7.14
Top of Base			10.77	5.88
Top of Sub-base			9.00	5.56
Top of Subgrade			7.36	4.35

From Table 14, it can be observed that for a class 9 vehicle traveling at 55 mph in June 2015, the frequencies calculated by MEPDG using Eq. (21) decreases with depth. Unlike frequencies from FWD test, under actual class 9 vehicle field frequency decreases with depth. Like before, ME software overestimates the DF for all the pavement layers. For HMA layer, the DF value differs 80% between ME calculated and field obtained value. For the base, subbase, and subgrade layer ME software differs with field measured DF by 83%, 62% and 69%. In actual field condition, a vehicle with higher velocity produces much less frequencies than it is observed with the simulation of lower speed vehicle in ME design software. To match the same DF values that are observed in field conditions ME software has to be simulated at a vehicle speed of 35 mph, which is much less than the legal limit operating speed of a class 9 vehicle in any interstate. Comparison of the DF for the month of February 2016 is given in Table 15.

TABLE 15 Comparison of DF for February 2016 under class 9 vehicle

Location	ME Speed (mph)	Actual Speed (mph)	ME frequency (Hz)	Field frequency (Hz)
Bottom of HMA	55	62	11.62	7.14
Top of Base			9.64	5.88
Top of Sub-base			8.01	5.56
Top of Subgrade			6.57	4.35

Like Table 14, similar observations were made from Table 15. For HMA layer, the DF value differs 63% between ME calculated and field obtained value. For the base, subbase, and subgrade layer ME software differs with field measured DF by 64%, 44% and 51%. Again, to match the same DF values that are observed in field conditions ME software has to be simulated at a vehicle speed of 35 mph, which is less speed than required on an interstate.

From the above discussion, it can be observed that ME design always overpredicts the DF value than what is observed in the field. When higher DF value is used in the pavement design, through the $|E^*|$ value, it is expected that the pavement response will be on the linear viscoelastic region. This is because higher loading frequency means the load will be applied within a very short amount of time. Being viscoelastic in nature, with the same amount of load asphalt pavement will deflect more when loading period is longer compared to when loading period is quicker. With continuous application of the loads for a longer time than what was accounted for in the design, pavements are expected to reach non-linear viscoelastic range early, which will eventually shorten the pavement design life.

Discussion

The following remarks can be made based on the obtained results:

- Dominant frequency (DF) values for the instrumented pavement section were identified under both the FWD test load and actual load from class 9 vehicles for summer and winter time. It was observed that DF values do not change in different depths under the FWD test load. However, DF values were found to be decreasing with increasing depths under the actual traffic loads from class 9 vehicles.
- DF values from the FWD test load and actual traffic conditions were compared with the DF from ME design software. It was observed that ME design always overpredicts the DF value.

MECHANICAL PROPERTIES OF ASPHALT CONCRETE

The mechanical properties of asphalt concrete (AC) are a function of time, temperature, and applied stress. A variety of mechanical models, e.g., elastic, viscoelastic, visco-plastic, and creep have been used to characterize the mechanical properties of AC *(29–32)*. Although an elastic model is used to characterize the behavior of AC for its simplicity, previous researchers have found that at intermediate and high temperatures an elastic model always underestimates the AC layer response *(33, 34)*. Typically, the viscoelastic parameters of the AC layer are determined using laboratory tests to be incorporated in the pavement design. In this study, mechanical properties of AC were evaluated based on the response from field instrumentation.

AC is a viscoelastic material which has a certain level of rigidity like elastic material, and it also flows and dissipates energy like a viscous fluid. At high temperatures or under slow-moving loads, AC behaves in a purely viscous manner. However, when the temperature is low, or loads are applied at a higher rate, then AC behaves more like a brittle elastic material. During high temperature, AC becomes susceptible to permanent deformation such as rutting; during low temperature, AC is more prone to low temperature cracking. Fatigue related distresses are important for intermediate temperature, as most of the traffic loads are applied at this temperature range.

When any load is applied on top of an AC layer it creates mainly two types of responses: elastic response and viscous response. The elastic response is recoverable. It is recovered as soon as the load is removed. However, the viscous response has two parts: recoverable and irrecoverable. If a sufficient amount of time is given, then a portion of the viscous response can be recovered. Viscous deformation is dependent on time, stress level and temperature. There are several mechanical models to describe the isotropic linear viscoelastic behavior of the AC such as the Maxwell model, Kelvin model and Burger model *(35)*. Researchers have used laboratory testing to obtain the mechanical parameters of AC using the previously mentioned isotropic viscoelastic models. Mun and Zi (2010) have used dynamic modulus test on AC to determine the mechanical model parameters. Aragão et al. (2010) have used a uniaxial tensile test to determine the viscoelastic parameters using the Maxwell model. Elseifi et al. (2006) have used indirect diametral test to determine the viscoelastic parameters using the Kelvin model. Many researchers have used nanoindentation technique on AC to model its creep response *(38–40)*. However, to date, researchers have determined the isotropic viscoelastic mechanical model parameters from the laboratory prepared AC sample. Researchers were not able to determine the isotropic viscoelastic mechanical model parameters directly from the field AC without any type of coring. With the recent advancement in technologies, many states across the U.S. have adopted instrumented pavement sections. If a load is applied on the pavement surface, then its response can be observed by the installed sensors at different depths inside the pavement. Therefore, in this study, the authors have used a new method to determine the isotropic viscoelastic mechanical properties directly from the field AC response through an instrumented pavement section at different intermediate temperatures.

Objectives

The main objective of this study is to determine the isotropic viscoelastic mechanical properties of asphalt concrete at different temperatures form the pavement response obtained through an instrumented pavement section.

Analysis Procedure

There are several mechanical models to characterize the isotropic viscoelastic response of AC. Maxwell model, Kelvin model, and Burger model are few of them. In this study, Burger model is used to model the creep behavior of AC. Burger model is a combination of Maxwell and Kelvin model. The Burgers model is represented using several springs and dashpots arranged in series and parallel connection. A representation of the Burger model is shown in Figure 64. The differential constitutive equation of a four-parameter Burgers model can be represented using Eq. (34).

$$\frac{\eta_1\eta_2}{E_2}\ddot{\varepsilon} + \eta_1\dot{\varepsilon} = \frac{\eta_1\eta_2}{E_1E_2}\ddot{\sigma} + \left(\frac{\eta_1}{E_1} + \frac{\eta_1}{E_2} + \frac{\eta_2}{E_2}\right)\dot{\sigma} + \sigma \tag{34}$$

Eq. (34) is a second order differential equation with respect to stress and strain. There are four constant coefficients which are functions of four parameters E_1, E_2, η_1 and η_2 in Eq. (34). E_1 and E_2 are Young's modulus of the springs, and η_1 and η_2 are the viscosity parameters.

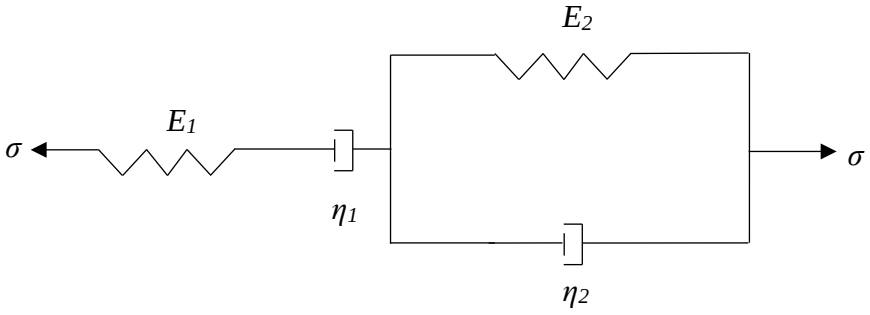

FIGURE 64 Burger model for isotropic viscoelastic material

Integrating Eq. (34) from time, $t_1 = 0$ to time, $t_2 = t$, with initial conditions $\varepsilon(0) = {}^{\sigma}/_{E}$ and $\dot{\varepsilon}(0) = {}^{\sigma}/_{\eta_1} + {}^{\sigma}/_{\eta_2}$ leads to Eq. (35)

$$\varepsilon(t) = \frac{\sigma}{E_1}\left(1 + \frac{t}{T_1}\right) + \frac{\sigma}{E_2}\left(1 - e^{-\frac{t}{T_2}}\right) \tag{35}$$

For constant stress, creep compliance $D(t)$ at various times can be obtained as:

$$D(t) = \frac{\varepsilon(t)}{\sigma} \tag{36}$$

Therefore, the Burger's model creep compliance from Eq. (35) is shown in Eq. (37).

$$D(t) = \frac{1}{E_1}\left(1 + \frac{t}{T_1}\right) + \frac{1}{E_2}\left(1 - e^{-\frac{t}{T_2}}\right) \quad (37)$$

E_1 is the instantaneous modulus; and T_1 and T_2 is relaxation time and retardation time respectively. For this reason, if pavement response can be obtained under constant stress, then using creep compliance of Eq. (37) AC isotropic viscoelastic parameters such as E_1, E_2, T_1 and T_2 can be obtained.

At the I-40 instrumentation section regular monthly FWD tests were conducted since 2012. At the designated locations, FWD load was applied. FWD test setup was mounted on a truck, which is a class 5 vehicle. The FWD truck drove on top of a sensor location and applied load. The baseline of the pavement strain gage signal changed either due to loading or diurnal temperature variation. If no load was present, then diurnal temperature variation changed the baseline *(41)*. However, during FWD testing, the inclination of the baseline was due to the creep behavior of AC.

Horizontal tensile strain at the bottom of different AC sub-layers, as well as vertical compressive stresses in base, subbase, and subgrade were collected under the FWD tests. During the FWD test, a total of four load levels are applied and these are 6, 9, 12, and 16 kip respectively. At each of these load levels, four replicates drops were applied where the first three drops are considered as seating drops. Figure 65 shows the strain gauge reading in volt (electric signal) over time during the FWD test. It is observed that the signal increases gradually with time with a total of 17 spikes at a regular interval. The gradual increase of this signal was due to the creep behavior of the AC layer under the static/self-weight of the FWD loading assembly resting on the pavement surface. The first spike/peak is due to the seating drop which was applied to ensure the firm contact between the geophones/sensors and surface. Among the remaining 16 peaks, the first group of drops (first four drops) is due to the 6-kip load. Similarly, the second, third, and fourth groups of drops are 9, 12, and 16-kip load respectively. The maximum magnitude of the signal is at 16-kip whereas the minimum magnitude of the signal is at 6-kip load.

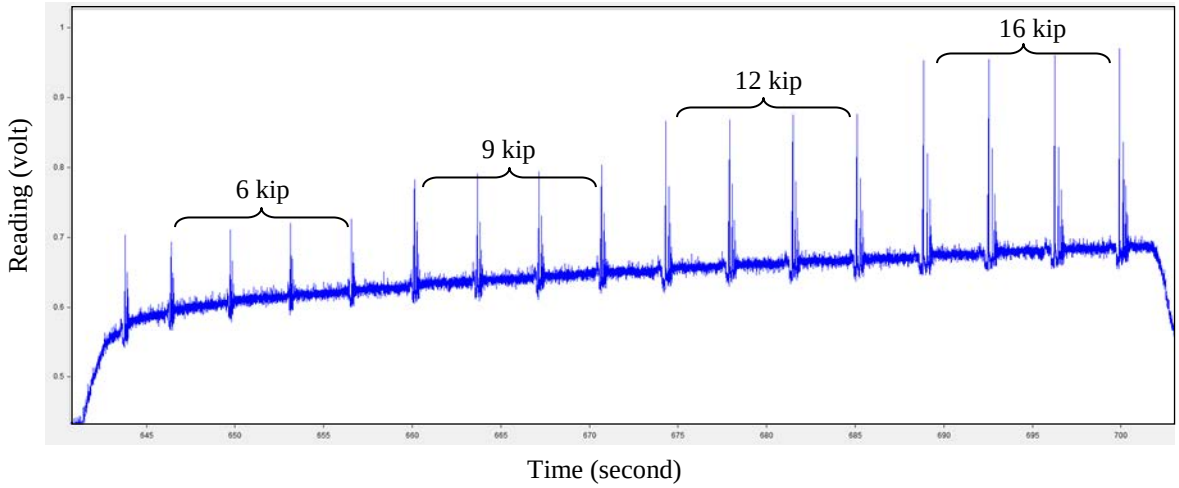

FIGURE 65 Data from instrumentation under FWD test load

This type of data collection, at different times over a day and in different months, is repeated for the rest of the strain gauges and pressure cells. Once the data are collected, voltage differences for every signal peak are extracted. Calibration factors, as assigned for strain gauges and pressure cells, are then multiplied with the extracted voltage difference to determine the stress-strain.

Signal Processing

To obtain creep response of AC under the self-weight of the FWD truck, some signal processing must be done. Figure 66 shows the signal processing steps involved to extract the creep response of AC under the self-weight of FWD truck. When the FWD truck goes on top of any sensor location and applies the FWD load, the sensor captures the pavement response due to the FWD load as well as the pavement response from self-weight of the truck. It is shown in Figure 66 (a). FWD load is an impact type of load and it is applied on the pavement surface for a very brief amount of time. To observe creep response of the AC layer, it is important to apply a constant stress on the top of the pavement surface for a certain amount of time. As mentioned earlier, total of 16 drops of FWD load is applied to a particular location on the pavement. It requires around one-minute for the FWD truck to apply all these 16 FWD test drops. During this time, self-weight of the truck is applied on the pavement surface. Therefore, the AC layer creep response under the constant self-weight of the FWD truck for this one-minute period of time can be observed from the sensor signal. However, to study this AC layer creep phenomenon under FWD truck self-weight, it is important to remove the FWD impulse responses. Savitzky-Golay filter *(28)* was used to remove the FWD impulse responses.

Figure 66 (b) shows the AC layer response under self-weight of the FWD truck. Figure 66 (b) also shows that after 60 seconds the strain is reduced, and strain is within Linear Visco-Elastic (LVE) range *(42)*. This is due to the relaxation nature of the AC layer for removal of the load.

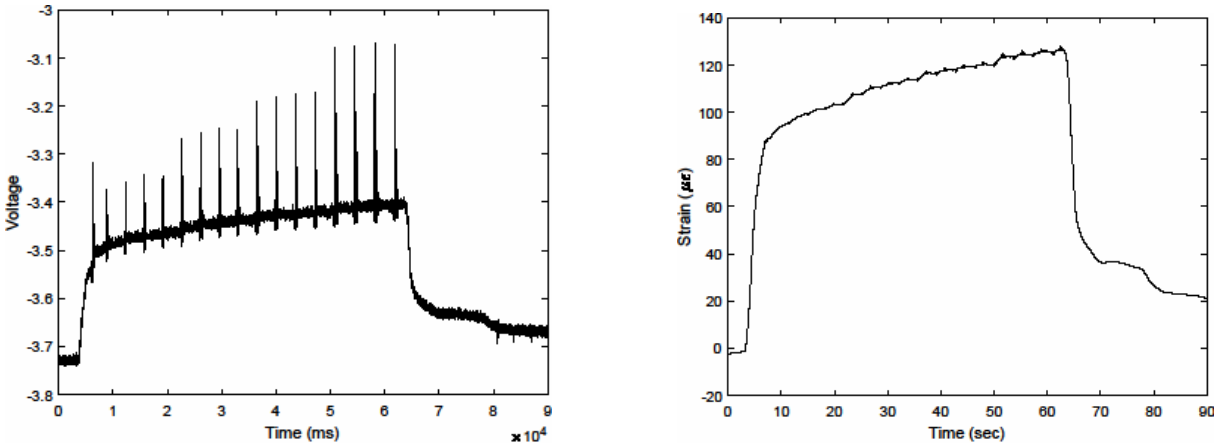

(a) Signal with FWD and truck self-weight (b) Signal without FWD impulse response

FIGURE 66 Creep response extraction from sensor signal for May 2017

AC Creep Response

To obtain the AC layer creep response using Eq. (36), the pavement strain shown in Figure 66 (b) must be divided by the applied stress. The value of average stress generated at the bottom of HMA layer due to the self-weight of the FWD test truck is around 3.5 psi, which is obtained from the earth pressure cell. EPC and the strain gage both are located at the bottom of the HMA layer. Therefore, the AC layer creep compliance curve can be obtained using Eq. (36) from the stress value and the strain response. Creep compliance curves of the AC layer at different times of the year is shown in Figure 67.

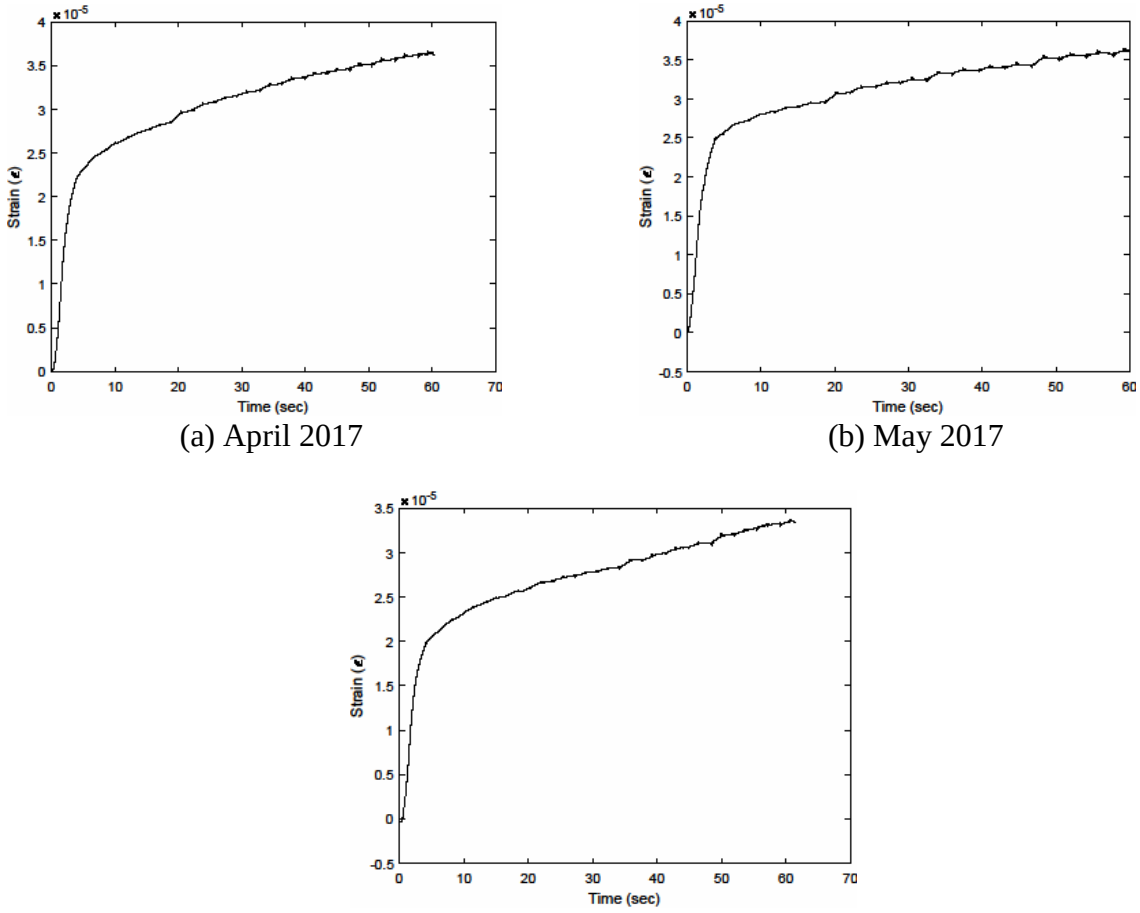

(a) April 2017 (b) May 2017

(c) November 2017

FIGURE 67 Creep Response of AC under FWD truck self-weight

Once the creep compliance curves are obtained, then they were fitted to the Eq. (37) to obtain the isotropic viscoelastic parameters. Table 16 shows the fitted parameters.

TABLE 16 Burger Model Parameters from Instrumentation Response

Month	Average AC Temperature (°C)	E_1 (ksi)	E_2 (ksi)	T_1 (sec)	T_2 (sec)
April 2017	18.3	498	42.4	10.27	2.924
May 2017	24	438	40	12.88	2.245
Nov 2017	13.3	582	48.8	8.364	2.814

From Table 16, it can be observed that under same level of applied stress, isotropic viscoelastic parameters of AC are dependent on temperature. Three months of data: April 17, May 17 and November 17, were used in this study. During these months average AC layer temperature varied from 13 to 24 °C. Instantaneous modulus E_1 is responsible for the instantaneous response of the AC layer. The other Young's modulus is related to the time-dependent response of the AC layer. From Table 16, it can be seen that when the temperature is lowest both E_1 and E_2 have higher values compared to their values when the temperature is highest. From May 2017 to November 2017, average AC temperature decreased around 11°C. For this 11°C temperature variation, E_1 increased by around 33% and E_2 increased by around 22%. Moreover, relaxation time is higher and retardation time is lower when the temperature is high. On May 2017, it takes 12.88 sec for the AC layer to reduce its stress to 36.8% of its original value. On the other hand, in November 2017, it takes 8.364 sec for the AC layer to reduce its stress to 36.8% of its original value. Therefore, 11°C temperature increment reduces the relaxation time by 35%. These variations in modulus and time are due to the intrinsic nature of AC. When AC layer reaches a higher temperature, it becomes soft; as its viscous nature starts to dominate the overall property. On the contrary, when the AC layer reaches a lower temperature, it becomes stiff as its elastic nature starts to dominate the overall property.

AC MODULUS WITH SPECTRAL ANALYSIS OF SURFACE WAVE FROM FWD

The general procedure for the evaluation of soil properties through wave propagation is straight forward. An impulse is generated and the response of that impulse travels through the surrounding media. This impulse response is recorded through several sensors placed at known distances. This information is used to calculate the wave velocity and subsequently is used for the determination of elastic properties. There are mainly two types of techniques available to capture the wave propagation. These are:

a) Borehole seismic method
b) Surface seismic method

In borehole seismic method, either source or receiver are kept on a borehole while the other is left on the surface. Sometimes both source and receiver are kept on different boreholes. In this method, it is typically assumed that the ray travels directly from the source to the receiver. In the surface seismic method, both source and receivers are kept on the surface and waves comes to receivers as a combination of direct waves, reflected waves and refracted waves.

In this study, SASW method was used to determine the elastic properties of the pavement. In traditional SASW setup both the source and receiver are kept at the surface level, however, in this study source was at the surface and receiver was at 11.1 inches below the surface. The impulse was generated through the application of a 9-kip FWD test load on the pavement surface and its response was recorded through horizontal axial strain gages.

Application of load on an infinite homogenous, isotropic and elastic media creates body waves and surface waves. The resolution of the installed sensors is not high enough to differentiate between body waves. However, surface waves can be easily detected through the sensors. Rayleigh waves have velocity approximately 90% of the S-waves. Therefore, if the velocity of the R-wave can be determined from the installed sensors through the surface wave spectrum analysis (SASW) method then the elastic properties of the medium can be obtained.

When the load is applied at the top of the pavement surface the response is recorded via the strain gages at the bottom of the pavement at different positions as shown in Figure 68. This sensor arrangements are similar the downhole seismic method. Instead of 3D motion sensors, the response is being monitored using installed strain gages. It is assumed that the responses observed through the strain gages are the result of direct wave propagation and there is no or very little contribution of reflected or refracted waves. It is also assumed that the wavelength of the generated wave through the FWD test load produces reliable responses for spectral analysis. With these assumptions, the waves can be treated traveling through an elastic space and from the SASW the properties of the traveling media can be identified.

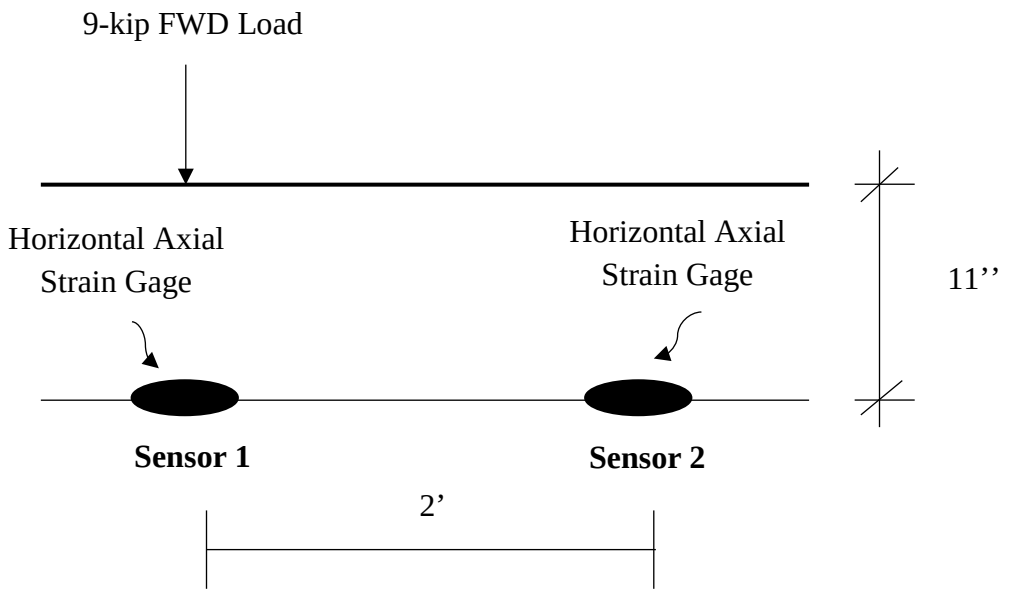

FIGURE 68 Sensor arrangement and load application

Methodology

As shown in Figure 69, waves generated through the FWD 9-kip load arrive directly to the installed sensors at the bottom of the HMA layers. Due to the distance in between the sensors, the registered signals at those two sensors, under the same impulse, will have a phase difference. There will be a 360° phase difference if the travel time equals the period of the wave.

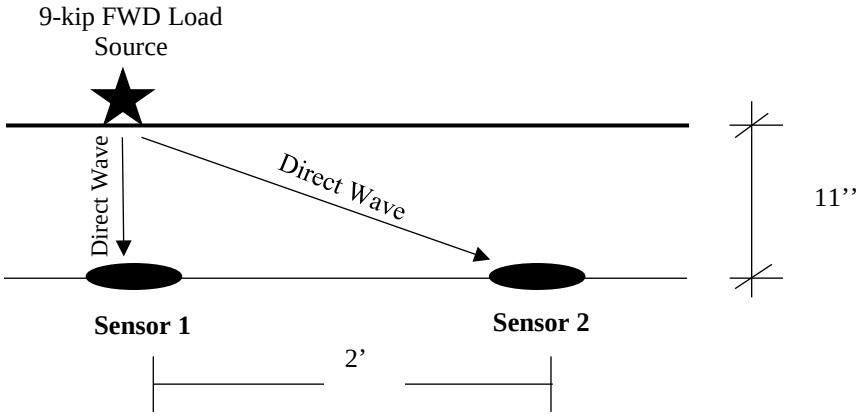

FIGURE 69 Direct wave traveling from source to sensor

Thus, the travel time can be written as

$$t = \frac{\phi / f}{360} \tag{38}$$

here, f is the frequency, Φ is phase angle for a certain frequency. In Eq. (38), travel time is calculated for a certain frequency. However, the response of FWD 9-kip test load creates a signal which has a range of frequencies. For this reason, from the response signal, a window is selected which contains only the body waves.

For the same selected window, the phase difference between the signals from both sensors is calculated. This phase difference is calculated for each frequency, which is embedded in the signals of the selected window. From the obtained vector of phase difference and frequencies, a plot of phase difference vs frequency is generated, and the phase was unwrapped for each frequency. The slope of the unwrapped phase vs. frequency graph was gives the value of Φ/f. This value is used in Eq. (38) to obtain the travel time. With travel time and the information about the spacing of the sensors (S), the velocity of Rayleigh wave (V_R) is determined.

$$V_R = \frac{X}{t} \tag{39}$$

Rayleigh wave velocity and shear wave velocity are related by Poisson's ratio. However, as mentioned earlier, Rayleigh wave velocity is around 90% of the shear s-wave velocity.

$$V_S = (1.135 - 0.182\upsilon)V_R \tag{40}$$

Once the S-wave velocity is obtained elastic property of the medium can also be obtained. Shear modulus (G) of the medium and S-wave velocity are related as

$$G = \rho V_S^2 \tag{41}$$

In Eq. (41), ρ is mass density. In an isotropic media, Young's modulus (E) and shear modulus (G) is related through the following equation:

$$G = \frac{E}{2(1+\upsilon)} \tag{42}$$

Combining Eq. (41) - (42), Young's modulus can be obtained as follows:

$$E = 2(1+\upsilon)\rho V_S^2 \tag{43}$$

In Eq. (43), υ is Poisson's ratio.

Analysis

Figure 70 shows the response of sensor 1 and sensor 2 when 9 kip FWD load has been applied directly on top of sensor 1 for the month of January 2017. It shows the response of 4 repeated FWD 9 kip load. From

Figure 70, it is evident that if 9 kip FWD load is applied directly over sensor 1 then at a distance of 2 feet, on sensor 2, response can be captured. The responses registered at sensor 1 and sensor 2 are results of direct rays. From these four FWD 9-kip drops, a specific window, last FWD 9-kip

drop, was selected for further analysis. However, before performing any analysis it is important to remove the noise embedded in both the signals. Savitzky-Golay filter was used to increase the signal to noise ratio *(28)*. The results are shown in Figure 71. As the sensors are 2′ apart each other, therefore, there may be a phase difference in the signals of the selected window. Moreover, Fourier transformation can be applied to the signals of the selected window to obtain the embedded frequencies, as shown in Figure 72.

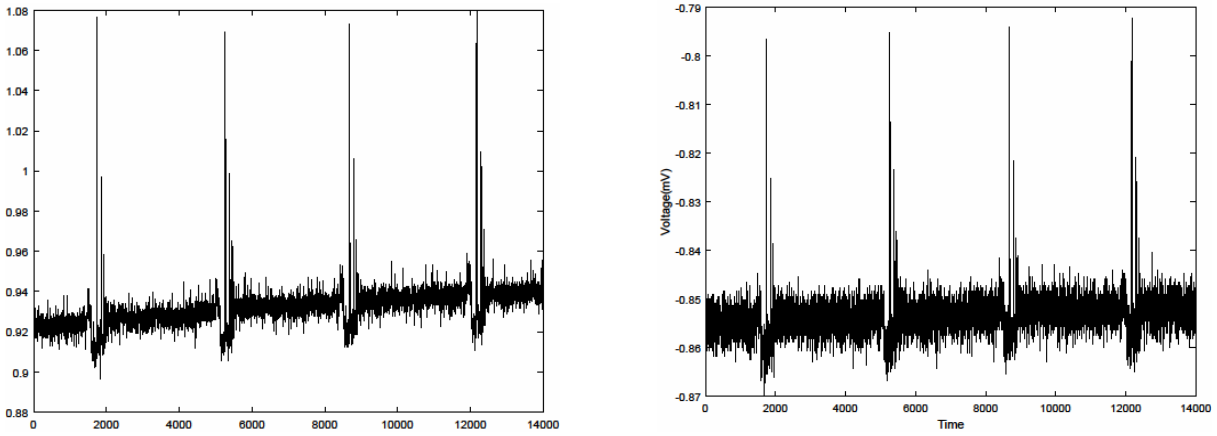

(a) Raw Signal in Sensor 1 (b) Raw Signal in Sensor 2

FIGURE 70 Whole signal Under FWD 9-kip load for January 2017

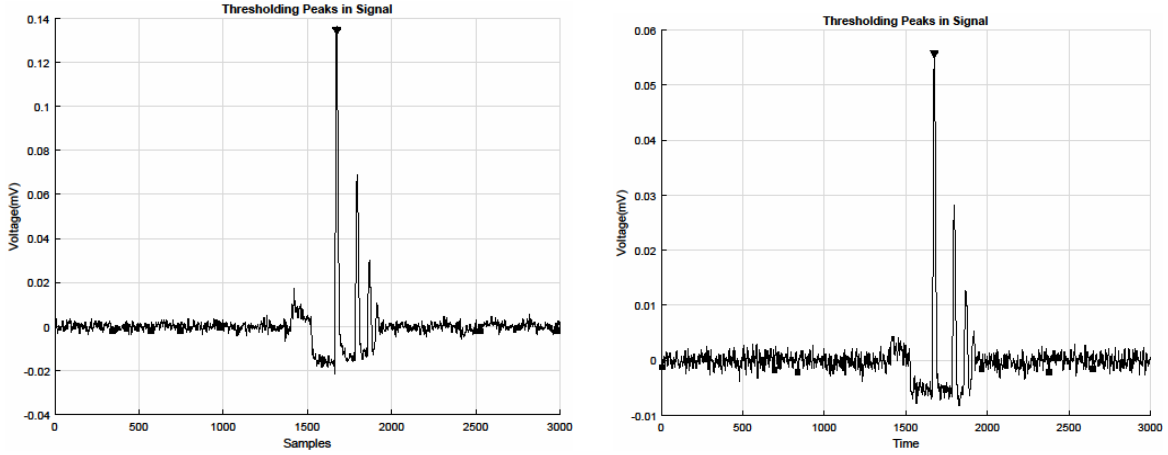

(a) Processed Signal in Sensor 1 (b) Processed Signal in Sensor 2

FIGURE 71 Selected signal window for January 2017

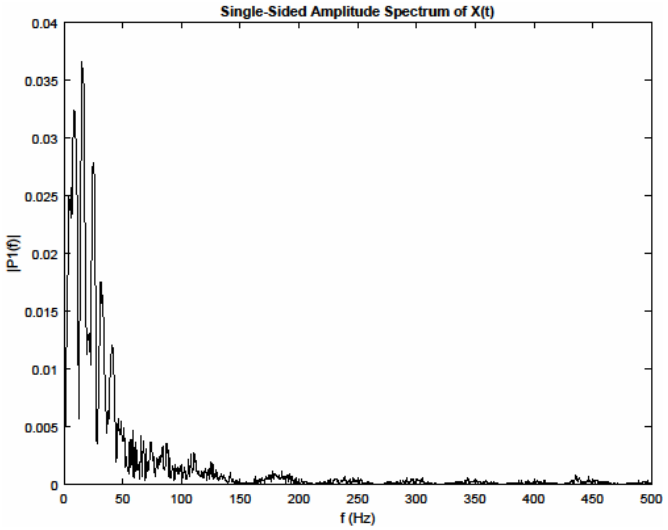

FIGURE 72 Frequency Spectrum

Once the embedded frequencies and phase difference is obtained for the selected signal window, then phase difference vs. frequency graph was generated to obtain the information whether phase reversal is occurring or not. Figure 73 shows the phase reversal with frequency for the selected signal window for the month of January 2017. It shows that up to 30Hz frequency value phase reversal is clear, however, with higher frequencies it becomes difficult to distinguish between the phase reversals. Therefore, the phase was unwrapped for the lower frequency values.

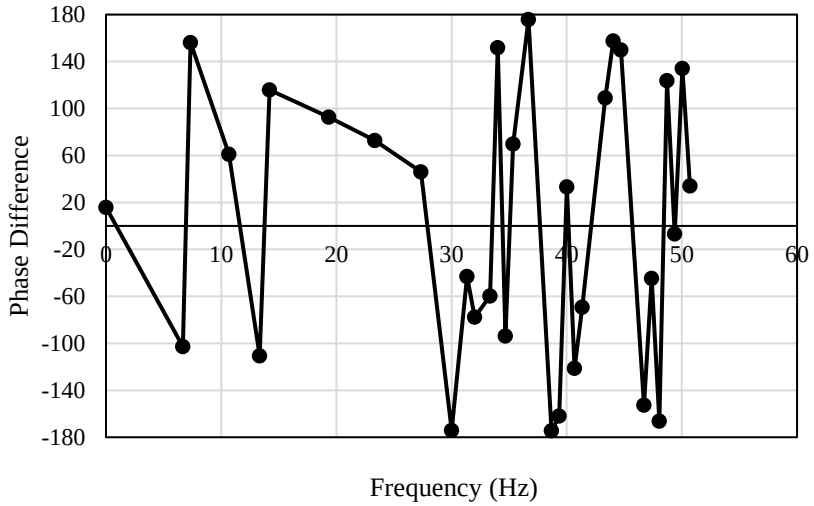

FIGURE 73 Phase Reversal with Frequency

Secant slope was obtained from the unwrapped phase frequency information of Figure 74. This slope gives the value of Φ/f. With this information and spacing of the sensors, Rayleigh wave velocity was determined for the month of January 2017 using Eq. (39). From R-wave velocity, shear S-wave velocity was determined. For the month of January 2017, the S-wave velocity was found to be 975 fps within the asphalt layer. On January 2017, the average pavement surface temperature was around 10°C. With the S-wave velocity and Eq. (43), Young's modulus value of AC for the month of January 2017 was found to be 950 ksi.

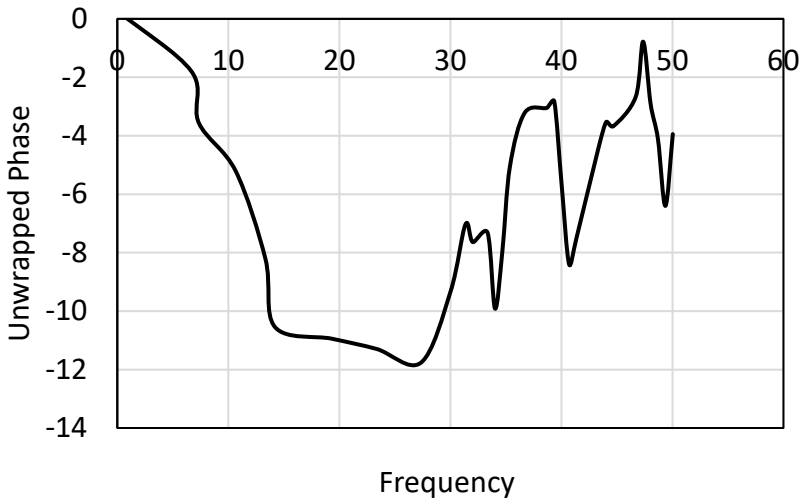

FIGURE 74 Unwrapped Phase Frequency Information

Similar observation was conducted for the month of February and March 2017. Shear wave velocity and Young's modulus of AC for those months are given in Table 17.

TABLE 17 AC Shear wave velocity and Young's Modulus

Month	Average Pavement Surface Temperature °C	Shear wave velocity in AC (fps)	Young's Modulus of AC (ksi)
January 2017	10	975	950
February 2017	9.8	952	908
March 2017	15.5	869	756

Relationship between Speed, Frequency and Strain

In this quarter, during the regular monthly FWD test, a special test was conducted. In that test, a NMDOT transport trailer with known load was used to pass the instrumented pavement section at different speeds. This was done to obtain the pavement response under known loading conditions. The trailer truck had a total gross weight of 72 kips: the transport truck was 52 kip and it was loaded with 20 kips. The transport truck passed the instrumented section at speed of 45, 55 and 60 mph. From the pavement response, the following quantities were identified: strain at the bottom of the asphalt layer and frequency. Three frequency quantities were determined for the known truck speeds. First was maximum peak frequency, mean frequency and frequency content with associated with 90% of the power. These three types of frequencies were determined to identify which would be more appropriate in quantifying pavement response. The maximum frequency may not be an important quantity. Instead of maximum frequency, frequency content associated with 90% power of the signal is more important *(43)*.

From Table 18, it can be observed that maximum frequency varies erratically with vehicle speed for the response from the strain gage at the bottom of AC. Moreover, the power associated with the maximum frequency is also very low. On the contrary, it can be seen that mean frequency increases with vehicular speed as expected, but the power associated with that signal is not

constant. It is very difficult to quantify any response with a varying item. For this reason, frequency content that has 90% power associated with it was chosen. From Table 18, as the vehicular speed increases 90% power frequency content is also increasing, which is expected. From the strain value, it can also be observed that as the vehicle speed increases pavement strain decreases.

TABLE 18 Pavement response from Horizontal Axial Strain Gage at bottom of AC

Horizontal					Sensor 1
Speed (mph)	max f (Hz)	power in max f	mean f (Hz)	90% Power f (Hz)	Strain (με)
45	8	50	7.9	14.67	61
55	4.67	34	10.64	16.67	35
60	5.33	27	13.7	20.67	19

Like Table 18, pavement response from the vertical strain gage under 3 inches from the pavement surface, at the first AC lift, was observed, as shown in Table 19.

TABLE 19 Pavement response observed from Vertical Strain Gage at First AC Lift

Vertical				Sensor 20
Speed (mph)	max f (Hz)	power in max f	mean f (Hz)	90% Power f (Hz)
45	2	58	6.81	17
55	2	58	7.2	20
60	2.67	50	14.44	37

From Table 19, it can be observed that no difference can be made among different speed of the vehicle based on the maximum frequency. Also, based on the mean frequency, no practical difference can be observed in between the responses from the bottom of AC and 3 inches from the surface. However, if frequency content associated with 90% signal power is used, then a clear distinct difference is observed.

From Figure 75, it can be seen graphically how pavement response changes with vehicular speed. Therefore, based on the available data, a correlation among frequency and speed can be obtained for the I-40 instrumented pavement section as some researchers have done for their pavement sections *(13, 44)*. The following relationship was developed from the obtained data:

$$f = 0.874e^{0.061v} \quad (44)$$

$$f = 5.08e^{0.0228v} \quad (45)$$

In Eq. (44) and Eq. (45), f is frequency (Hz) and v is speed (mph). Eq. (44) is for pavement response at the first lift of AC and Eq. (45) is pavement response at the bottom of AC. R^2 for Eq. (44) is 0.8 with an RMSE of 6 whereas for Eq. (45), R^2 is 0.9 with an RMSE of 1.4.

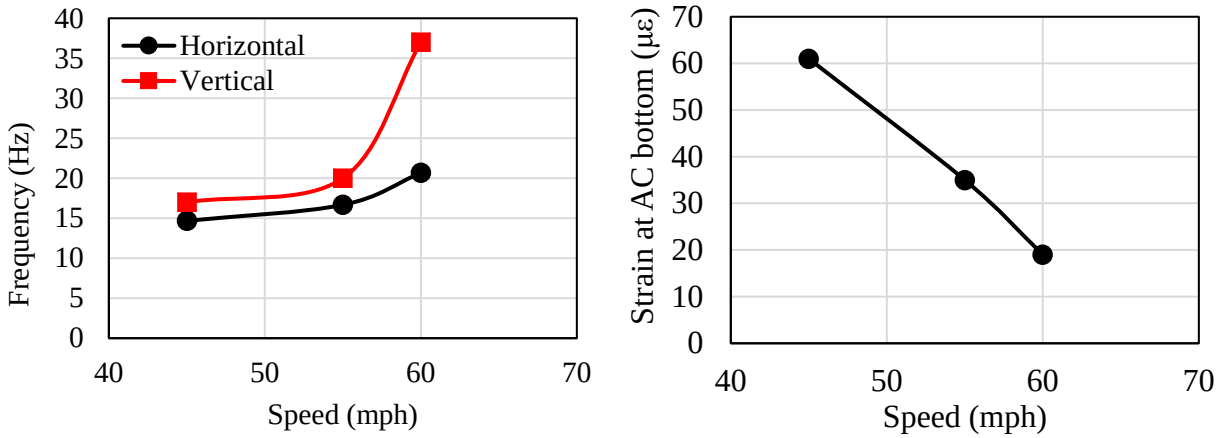

(a) Frequency vs Speed Speed

(b) Strain at the AC bottom vs

FIGURE 75 Pavement response at Different Speed

From Figure 75, it can also be implied that there exists a relation between frequency and measured strain of the pavement. As the frequency increases then the measured strain at the bottom of the AC layer also decreases.

Discussion

Based on the above study from the instrumentation data, the following remarks can be drawn:

- Spectral Analysis of Seismic Wave (SASW) was successfully applied to the pavement response obtained under the FWD test load to obtain the elastic property of the AC layer. With the application of this SASW method, without any iteration or assumption like FWD backcalculation, Young's Modulus of the pavement layers were obtained. For the month of January 2017 AC layer Young's Modulus was found to be 950 ksi; for February 2017 Young's Modulus of AC layer was 908 ksi whereas for March 2017 Young's Modulus of AC layer was found to be 756 ksi.
- For a certain loading, frequency in the AC layer decreases as the depth increases and frequency content associated with 90% of the signal power is more appropriate in pavement design.

WAVE PROPAGATION METHOD FOR AC YOUNG'S MODULUS

I-40 instrumentation section has an array of different kind of sensors installed. It has sensors installed at different depths and various sensors at the same depth. Therefore, if a load is applied on top of the pavement surface then the response of the pavement structure can be observed through the installed sensors. When an FWD load is applied on the pavement surface, it creates an impact. This impact produces seismic waves, which are detected through the installed accelerometers, also known as FWD sensors, on the surface, located at a certain distance. This response can be used to deduce many important features about the medium through which the wave travels and about the source that creates these waves. In this study, FWD sensors response under the 9-kip FWD test load is used to determine the elastic properties of the AC.

Methodology

The general procedure for the evaluation of soil properties through wave propagation is straight forward. An impulse is generated and the response of that impulse travels through the surrounding media. This impulse response is recorded through several sensors placed at known distances. This information is used to calculate the wave velocity and subsequently is used for the determination of elastic properties. In the surface seismic method, both source and receivers are kept on the surface, as shown in Figure 76 and waves comes to receivers as a combination of direct waves, reflected waves, and refracted waves.

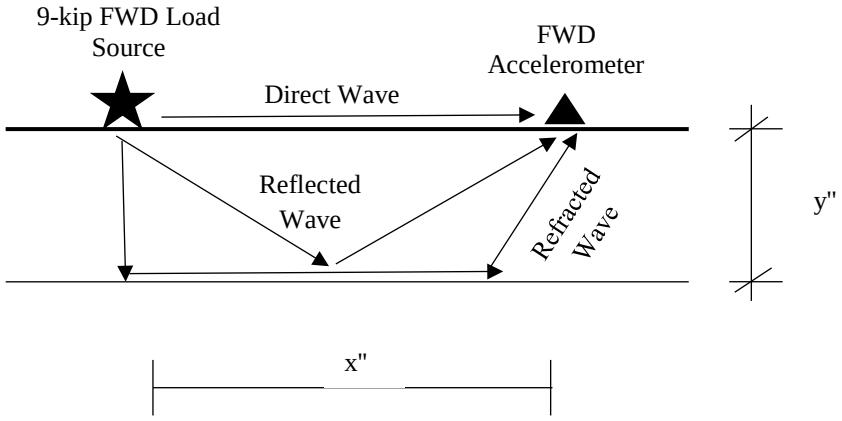

FIGURE 76 Different waves traveling from source to sensor

In this study, time-distance graph of wave arrival information also known as t-x diagram was used to determine the elastic properties of the AC layers. The impulse was generated through the application of a 9-kip FWD test load on the pavement surface and its response was recorded through FWD accelerometers.

For the traditional method of backcalculation, deflection time history of the pavement surface is required under the FWD load. This is deflection time history is obtained by performing double integration on the raw accelerometer data, as shown in Eq. (46).

$$a(t) = \frac{d^2z}{dt^2} \tag{46}$$

Instead of using the deflection time history, this study uses the raw accelerometer data to track the arrival time of the *p*-wave. FWD test truck has 7 accelerometers at different distances. By tracking the *p*-wave arrival time at each accelerometer, a t-x diagram, can be obtained. A typical *t-x* diagram obtained during a seismic investigation is shown in Figure 77.

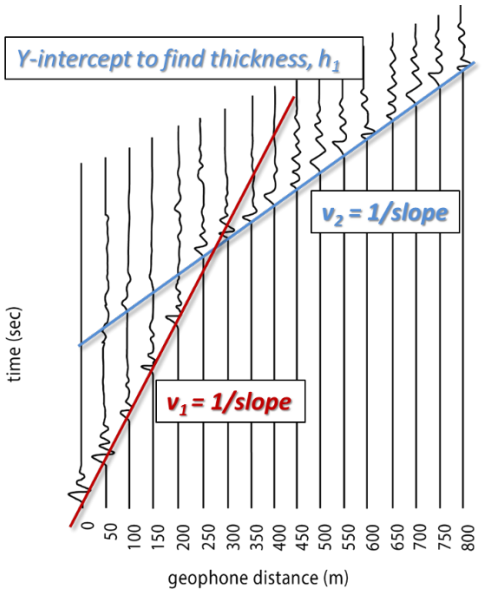

FIGURE 77 A typical t-x diagram

Instead of the slope the velocity of each layer can be obtained from Eq. (47):

$$t = \frac{x}{v_i} + 2h_{i-1}\sqrt{\frac{1}{v_{i-1}^{\ 2}} - \frac{1}{v_i^{\ 2}}} \tag{47}$$

here, v_i is the velocity of the *i*-th layer, v_{i-1} is the velocity of the *i-1*-th layer, h_{i-1} is the thickness of the *i-1*-th layer, *t* is the travel time of the wave and *x* is the sensor offset. Once the *p*-wave arrival time or velocity is obtained, the material property is obtained using the following equations shown in Eq. (48).

$$\left.\begin{aligned} v_p &= \sqrt{\frac{(\lambda+2G)}{\rho}} \\ \lambda &= \frac{\nu E}{(1+\nu)(1-2\nu)} \\ G &= \frac{E}{2(1+\nu)} \end{aligned}\right\} \tag{48}$$

here *E* is the Young's modulus of the AC layer, v_p is the velocity of the p-wave, *G* is the shear modulus, ν is the Poisson's ratio (assumed 0.35 for AC) and ρ is the mass density of the material (assumed 23240 N/m^3 for AC layer) *(45–47)*.

Data Analysis and Discussion

In this study, two months of raw FWD accelerometer data were analyzed for the AC modulus gradient analysis. September 2017 and March 2019 data were analyzed. The reason for using only two months of data is availability. Generally, DAT and THY files are stored and used for backcalculation purpose and they are only several megabytes in size. On the contrary, raw files are several hundreds of megabytes for each sequence and were not typically saved. RAW files are generally consisting of loading pulse information and arrival of wave times. Figure 78 shows the FWD raw files from September 2017. It is important to note that the horizontal axis of Figure 78 is the signal sample number. This is the typical way how the raw files are generated. Using the total time duration from THY file, sample numbers are converted to time. From Figure 78 (b) to Figure 78 (e), it can be observed that with the increasing distance from loading source, the accelerometer signal attenuates and the first peak arrival time in each sensor also changes.

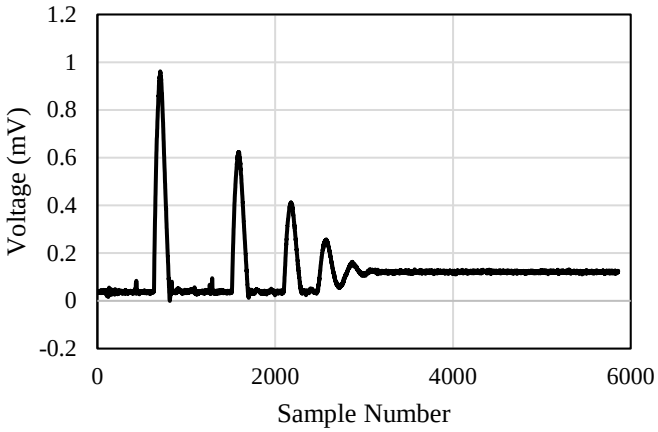

(a) Load Pulse

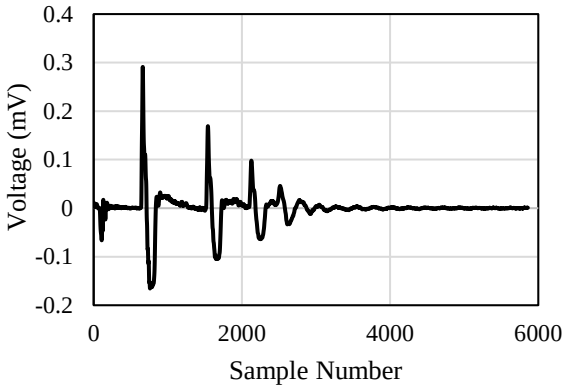

(b) Vibration at 0" offset

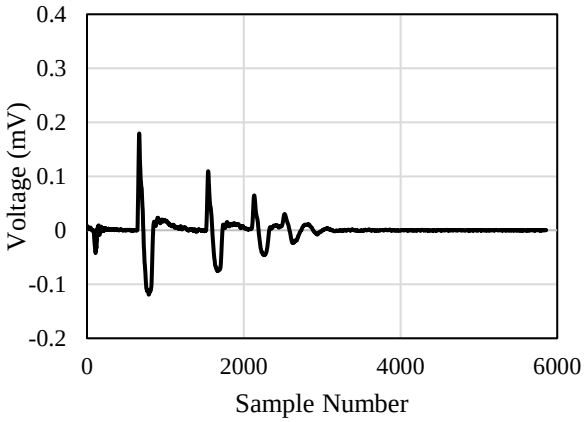

(c) Vibration at 12" offset

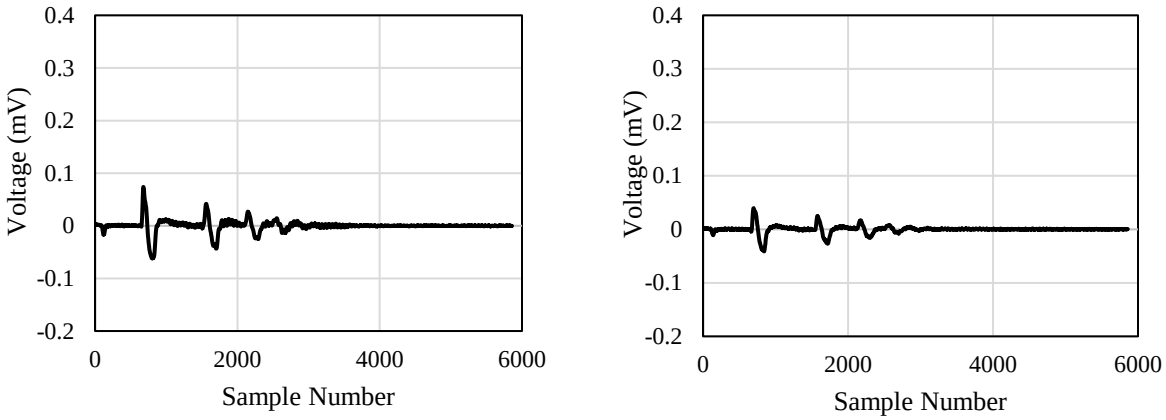

(d) Vibration at 36" offset (e) Vibration at 60" offset

FIGURE 78 Signals from FWD sensors on September 11, 2017, at 1 PM

Using the arrival time in Figure 78, *t-x* plot can be constructed. Figure 79 shows the *t-x* plot for the month of September 2017. The black dot represents the first *p*-wave arrival time at each FWD accelerometer offset. One of the caveats of seismic refraction is that it can only be used where the *p*-wave velocity increases in each successive layer. As wave velocity decreases in unbound layers after AC, thus, this study focused only on the three lifts of AC. Four colored lines can be seen in Figure 79. The velocity of the layers can only be determined for the layers where slope decreased for the successive lines. A similar diagram was also obtained for the month of March 2019.

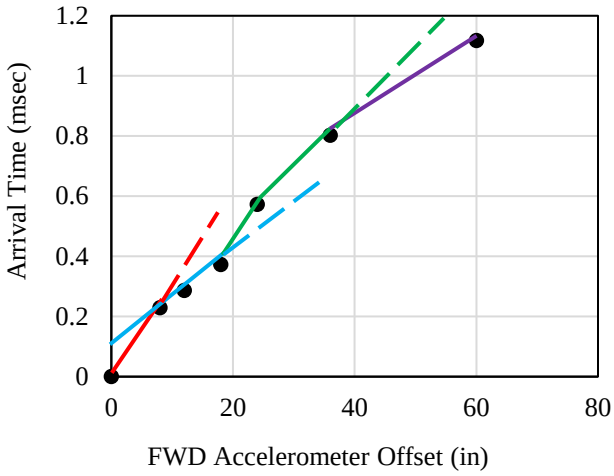

FIGURE 79 Time-distance (*t-x*) diagram for the month of September 2017

Table 20 shows the variation of modulus of AC lifts in different temperature conditions. As expected, modulus changes with both depth and temperature. Modulus change due to depth has an effect from both temperature and aging. Top AC lifts are exposed to the atmosphere therefore, they induce more damage due to aging and their modulus varies most with temperature change. For September 2017, 28°F of temperature change changes the modulus by 75% between the top and bottom AC lifts. For March 2019, the value was 52% for almost similar 26°F temperature change. This shows AC modulus varies more in warmer temperature than in cooler temperature conditions.

TABLE 20 Velocity and modulus of different AC lifts

	September 2017				March 2019			
Location	Temperature (°F)	Thickness (in)	v_p (ft/s)	Modulus (ksi)	Temperature (°F)	Thickness (in)	v_p (ft/s)	Modulus (ksi)
AC (Top)	104	8.79	2906	1651	78	9.33	4914	4716
AC (Bottom)	86	2.31	5817	6605	52	1.77	7309	10427

The seismic analysis also reveals the presence of water in the bedrock layer, which is around 30 ft from the top surface, obtained from the FWD deflection analysis. Figure 80 shows the depth to bedrock determination from the FWD deflection basin. From the seismic analysis, it was observed that there is a layer where velocity is higher than AC layer at some depth below the surface. Those layers have a *p*-wave velocity of around 4921 fps in warmer temperature condition of September 2017, and in cooler temperature condition of March 2019, the *p*-wave velocity increases to around 13123 fps. These velocities are in the range of p-wave velocity in water and ice respectively, which suggest that bedrock layer have water and the United States Geological Survey (USGS) data also suggest that depth of water table at Rio Puerco area near the instrumentation section is around 35 ft, shown in Figure 81.

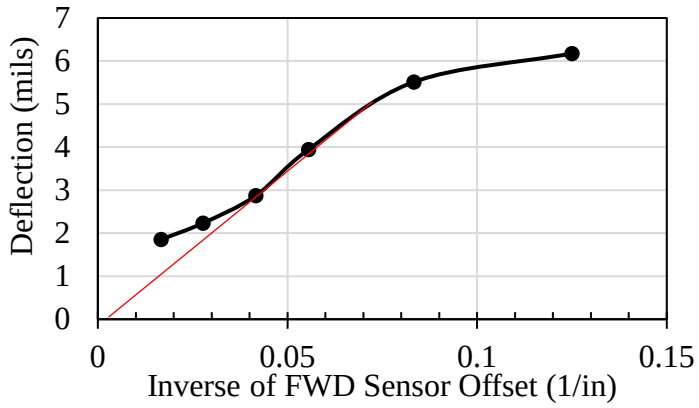

FIGURE 80 Depth to bedrock determination

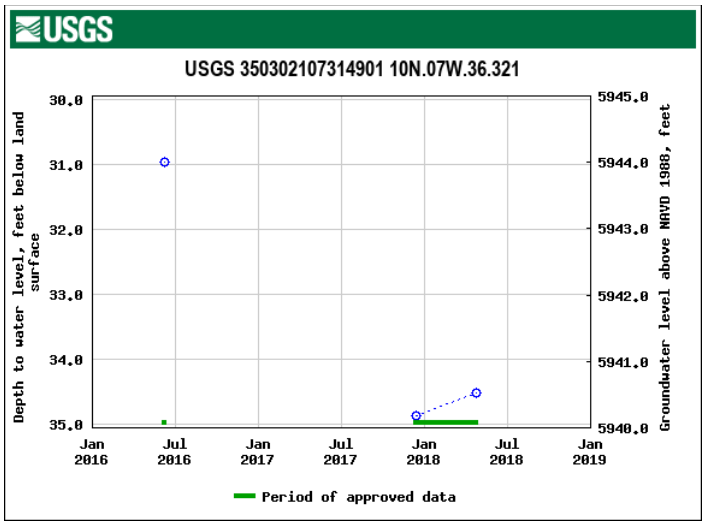

FIGURE 81 Depth of water table at Rio Puerco near instrumentation section (obtained from USGS website)

Remarks

From the above discussion, it can be said that the FWD sensor obtained wave information can be used to predict the stiffness gradient of the AC layer and condition of the sub-surface layers. AC stiffness varies with both temperature and depth. AC stiffness varies more along the depth in warmer temperature than in cooler temperature condition.

RESILIENT MODULUS MODEL

Resilient modulus (M_R) of the unbound layers is an important parameter for pavement design. Along with the AC layer, flexible pavement performance over the design period is dependent on the unbound layers. Traditionally, the unbound layer modulus are determined through the laboratory resilient modulus testing *(48)*. The amount of material required for a single set of M_R test is quite significant. If continuous pavement performance evaluation is the goal, then collection of the unbound materials after pavement construction can be challenging. Collection of unbound materials through coring is labor intensive and time consuming. In this regard, non-destructive testing such as FWD can be a suitable alternative.

Researchers have been using FWD test to monitor the pavement performance and evaluate the modulus of the pavement layers *(49–51)*. Some researchers have also used FWD testing to determine the stress dependency in the unbound layers. In their study, Salour and Erlingsson (2013) considered stress-hardening in the base layer and stress softening in the subgrade layer. Varma and Kutay (2016) have also used FWD test to quantify the pavement material properties. They have used FWD test to determine the damaged E^* of AC. However, none of these studies develop the k_1-k_2-k_3 model of the M_R test used in the Pavement ME design guide *(5)* from the non-destructive field testing.

Furthermore, Nazzal and Mohammad (2010) and Von Quintus and Killingsworth (1997) developed interconversion technique between laboratory resilient modulus and FWD modulus. However, both studies did not mention the stress level at which the interconversion was conducted. Stress level is important as they differ in field and laboratory condition. To determine resilient modulus model from field FWD test, the state of stress at different depth inside the pavement layers must be known. With recent advancement in measurement techniques, it is possible to accurately measure the stress at different layers. Many states across the United States have adopted instrumented pavement section *(24, 56, 57)*. The instrumented pavement sections have sensors installed at different depths, which measure the pavement response under any type of loadings. In this study, pavement responses from an instrumented pavement section under FWD test loads have been used to develop the resilient modulus model.

In addition, deflections from the sensor under FWD test load can also be used to quantify damage in the unbound layers. Al-Qadi and Appea (2003) have used Base Damage Index (BDI) to quantify damage due to rutting in the base layer with geosynthetics from FWD test. They did not consider the damage in the other unbound layers. Donovan and Tutumluer (2009) used the modified base damage index and modified Base Curvature Index (BCI) to quantify damage in all the unbound layers. However, their study was performed on airfield pavement to quantify damage due to the aircrafts. It is important to quantify the unbound layer damage in the highway pavements where dominant loads are coming from class 9 vehicle. Therefore, in this study, FWD sensor deflection under 9-kip test load was used to determine the relative damage in the unbound layers caused by traffic loads.

Objectives

The main objectives of this study are as follows:

a) Develop the resilient modulus model used in the Pavement ME combining the FWD testing on a field instrumentation section and layer elastic analysis.
b) Using the FWD deflection data BDI and BCI was obtained to quantify damage in the base-subbase and subgrade layer due to traffic loads.

Methodology

Resilient modulus (M_R) is used to describe the nonlinear constitutive relation of the unbound materials under repeated loading conditions. The ratio between the maximum cyclic stress (σ_{cyl}) to the recoverable strain (ε_r) under repeated dynamic loading is known as resilient modulus (M_R).

$$M_R = \frac{\sigma_{cyl}}{\varepsilon_r} \tag{49}$$

Typically, M_R is determined in the laboratory through the resilient modulus test on representative sample according to AASHTO T-307. To describe the constitutive behavior of the unbound materials Hicks and Monismith (1971) proposed a *k-θ* model.

$$M_R = k(\theta)^n \tag{50}$$

where M_R is the resilient modulus, θ is the bulk stress ($\theta = \sigma_1 + \sigma_2 + \sigma_3$) and *k*, *n* are material constants.

The model shown in Eq. (50), also known as bulk stress model, does not take deviator stress and confining pressure into account. Uzan (1985) modified the model in Eq. (50) to take deviatoric stress into account but the proposed model did not include confining pressure of soil.

$$M_R = k_1(\theta)^{k_2}\sigma_d^{k_3} \tag{51}$$

where, $\sigma_d$is the deviatoric stress ($\sigma_d = \sigma_1 - \sigma_3$) and k_1, k_2, k_3 are material constants.

Afterward, a modified model was introduced which takes both shear and bulk stress into account. This model was known as the octahedral shear stress model *(62)*.

$$M_R = k_1 p_a \left(\frac{\theta}{p_a}\right)^{k_2} \left(\frac{\tau_{oct}}{p_a}\right)^{k_3} \tag{52}$$

where p_a is the atmospheric pressure = 14.7 psi (101.325 kPa) and τ_{oct} is the octahedral shear stress = $^1/_3\sqrt{(\sigma_1-\sigma_2)^2+(\sigma_2-\sigma_3)^2+(\sigma_3-\sigma_1)^2}$.

The model shown in Eq. (52) is later modified and incorporated in Pavement ME design guide *(5)* to describe the material behavior of the unbound layers. The ME design model for M_R is shown in Eq. (53).

$$M_R = k_1 p_a \left(\frac{\theta}{p_a}\right)^{k_2} \left(\frac{\tau_{oct}}{p_a} + 1\right)^{k_3} \tag{53}$$

In this study, M_R model shown in Eq. (53) is developed based on the field FWD test. The following steps are followed to develop the M_R model from field non-destructive testing:

1) Perform regular FWD test to obtain the modulus of the unbound layers.
2) Obtain the stresses at different depths inside the unbound layers due to the FWD test loads through the installed EPCs. This is denoted as the vertical pressure (σ_v). The horizontal pressure (σ_h) due to the FWD test load application is obtained from the layer elastic analysis.
3) Total vertical pressure is obtained by adding the overburden pressure of the layers with the pressure reading from EPC.

$$\sigma_3 = \sigma_v + \sum_{i=1}^{n-1} \gamma_i h_i \tag{54}$$

here, *i* = layer above unbound layer *n*, γ_i is the density of the *i*-th layer, and h_i is the thickness of the *i*-th layer.

4) Total horizontal pressure is obtained by adding horizontal pressure from load with the earth pressure at rest.

$$\sigma_1 = \sigma_2 = \sigma_h + k_0 p_0 \tag{55}$$

where, k_0 is the coefficient for earth pressure at rest and p_0 is the overburden pressure. k_0 is obtained using the angle of internal friction.

$$k_0 = 1 - sin\varphi \tag{56}$$

where φ is the angle of internal friction. For this study, base and subbase layer angle of internal friction was taken as 45° and subgrade layer the angle of internal friction was taken to be 30° *(63)*.

To determine the damage in the unbound layers, this study uses modified index properties obtained from the pavement deflections under FWD test load *(59)*. Modified BDI and BCI are obtained using Eq. (57) and Eq. (58):

$$BDI = d_{300} - d_{900} \tag{57}$$

$$BCI = d_{900} - d_{1500} \tag{58}$$

where, d_{300} is the deflection at 300 mm from the loading plate (12 inch), d_{900} is the deflection at 900 mm from the loading plate (36 inch) and d_{1500} is the deflection at 1500 mm from the loading plate (60 inch).

Damage in the unbound layers can occur due to both traffic loads and environmental loads. Therefore, the *BDI* and *BCI* from traffic lanes were normalized against the non-traffic lanes to identify the damage due to traffic loads only. *BDI* and *BCI* under traffic loads were obtained from the FWD test on the driving lane and *BDI* and *BCI* of non-traffic lanes were obtained from the FWD test on the shoulders.

$$\text{Relative Base/Subbase Damage} = \frac{BDI_{traffic}}{BDI_{non-traffic}} \quad (59)$$

$$\text{Relative Subgrade Damage} = \frac{BCI_{traffic}}{BCI_{non-traffic}} \quad (60)$$

Results

Figure 82 shows the various stress distribution at the base layer under the FWD 9-kip test load from 2013 to 2017. Figure 82 shows that initially the base modulus decreased rapidly, and with time, the base modulus reduction rate has decreased. A similar trend was observed for the base stress distribution as well. Like the modulus, base stresses had also decreased from 2013 to 2017. This stress and modulus reduction may have been attributed from the stress dependency of the AC layer.

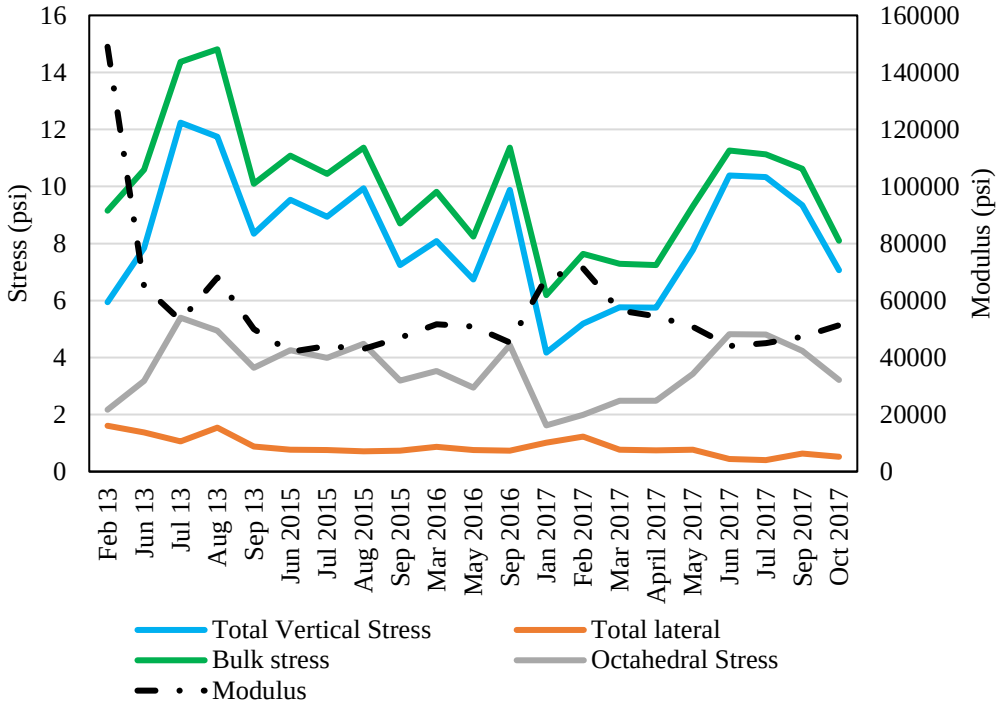

FIGURE 82 Stress distribution at the base layer under FWD 9-kip load

With the stress distribution and modulus of the base layer, Eq. (53) was fitted to the data using MATLAB 2018b to obtain the base material constants k_1-k_2-k_3. Fitting of the base layer data to Eq. (53) is shown in Figure 83. The nonlinear regression has yielded a R^2 value of 0.7.

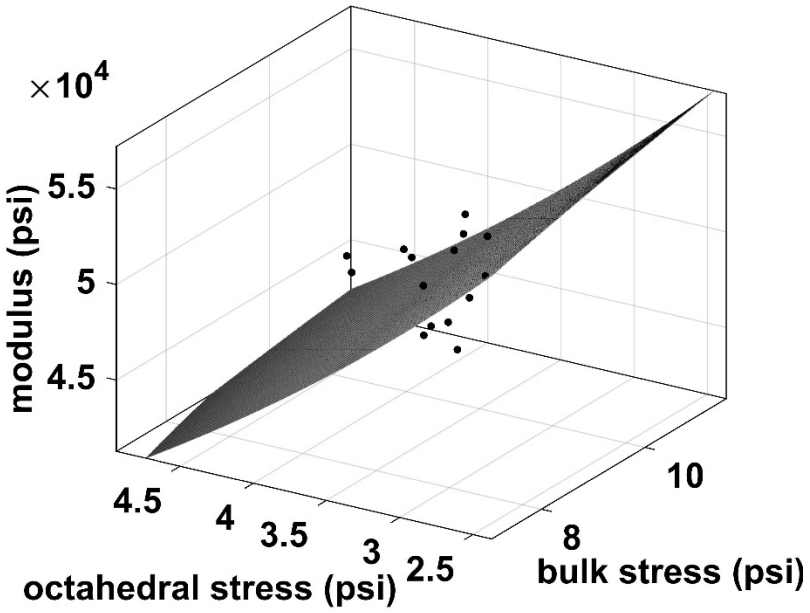

FIGURE 83 Base M_R model fitting

Base layer resilient modulus model from the field FWD test can be expressed as Eq. (61):

$$M_{R-Base-FWD} = 5617 p_a \left(\frac{\theta}{p_a}\right)^{0.1} \left(\frac{\tau_{oct}}{p_a} + 1\right)^{-2.22} \quad (61)$$

Figure 84 shows the various stress distribution at the subbase layer under FWD 9-kip test load from 2013 to 2017. Figure 84 shows that initially the base modulus decreased rapidly, and with time, the subbase modulus is increasing steadily. A similar trend was observed for the subbase stress distribution as well. Like the modulus, subbase stresses had decreased at a fast rate initially but since 2015, the modulus and stresses are increasing. These stresses and modulus increment may have attributed from the aging of the Reclaimed Asphalt Pavement (RAP) materials present in the subbase.

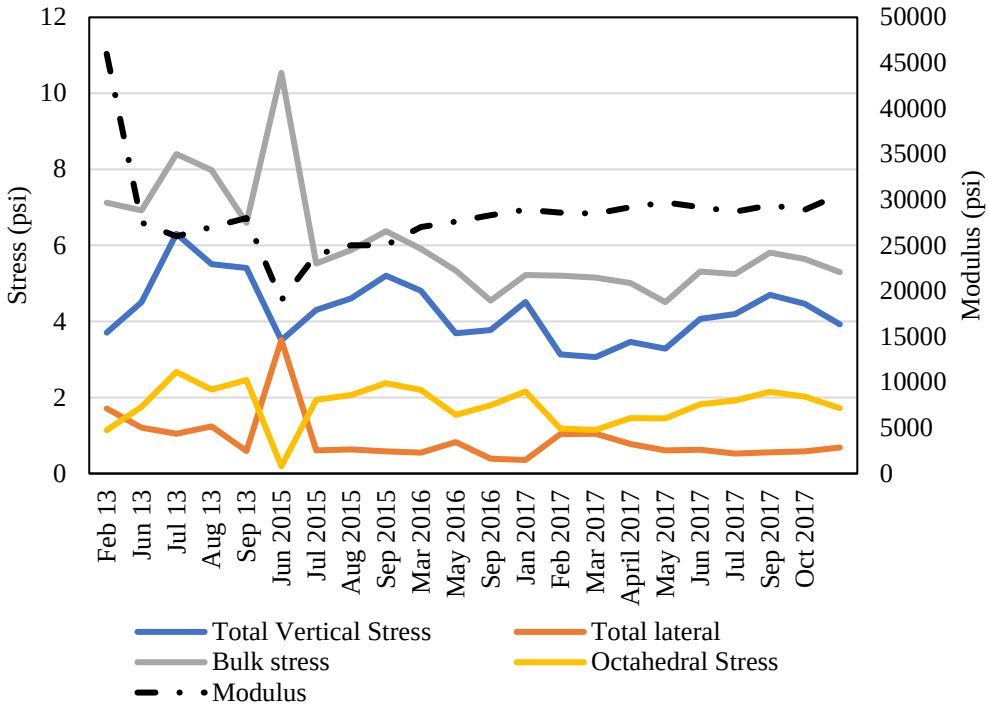

FIGURE 84 Stress distribution at the subbase layer under FWD 9-kip load

With the stress distribution and modulus of the subbase layer, Eq. (53) was fitted to the data using MATLAB 2018b to obtain the subbase material constants k_1-k_2-k_3. Fitting of the subbase layer data to Eq. (53) is shown in Figure 85. The nonlinear regression has yielded a R^2 value of 0.58.

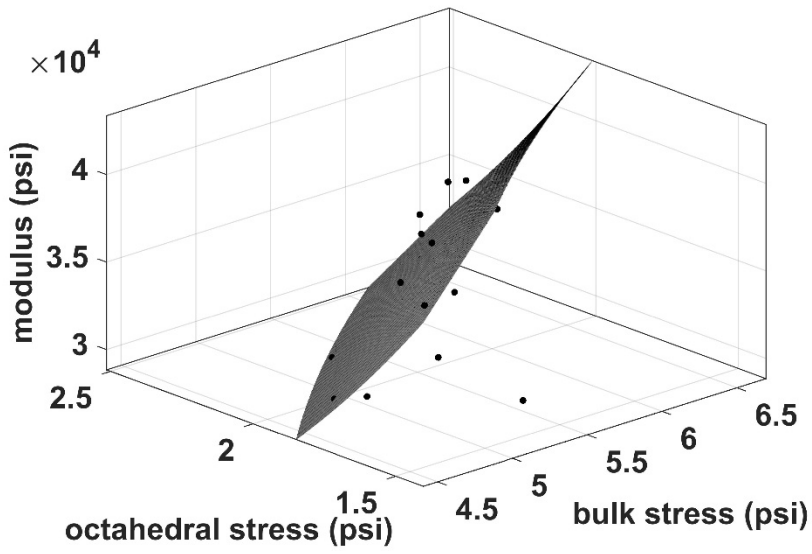

FIGURE 85 Subbase M_R model fitting

Subbase layer resilient modulus model from the field FWD test can be expressed as Eq. (62):

$$M_{R-Subbase-FWD} = 28700 p_a \left(\frac{\theta}{p_a}\right)^{1.213} \left(\frac{\tau_{oct}}{p_a} + 1\right)^{-10.3} \quad (62)$$

Like the subbase layer, similar stress and modulus distribution were observed for the subgrade layer. Figure 86 and Figure 87 shows the stresses and modulus distribution and curve fitting of the data.

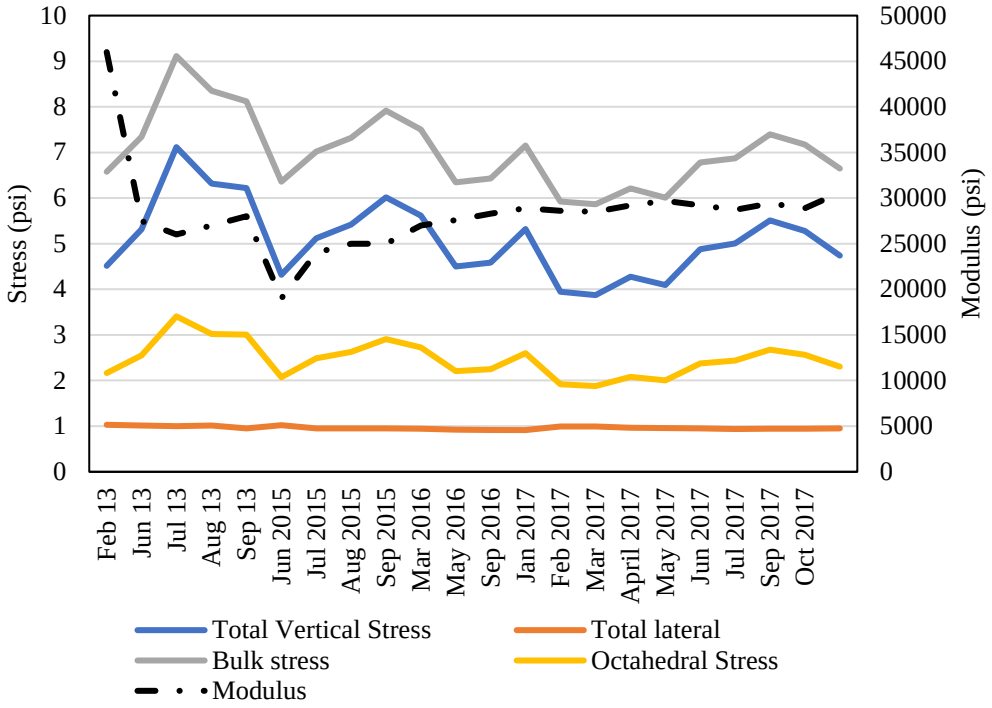

FIGURE 86 Stress distribution at the subgrade layer under FWD 9-kip load

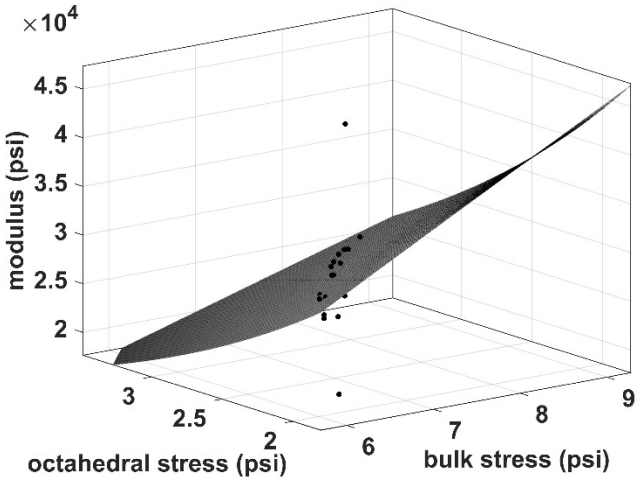

FIGURE 87 Subgrade M_R model fitting

Fitting of the subgrade layer data to Eq. (53) has yielded a R^2 value of 0.74. Subgrade layer resilient modulus model from the field FWD test can be expressed as Eq. (63):

$$M_{R-Subgrade-FWD} = 10100 p_a \left(\frac{\theta}{p_a}\right)^{0.94} \left(\frac{\tau_{oct}}{p_a} + 1\right)^{-6.13} \quad (63)$$

Validation

The M_R models developed in Eq. (61) to Eq. (63) were validated with the stress and modulus data obtained in March 2013, April 2016 and August 2017. These months were chosen because AC temperature was almost the same, around 21°C. It is important to note that the bulk and octahedral shear stress in these three months were not obtained under FWD test load rather they were obtained under the actual tandem axle of class 9 vehicle. The modulus obtained from the stresses under class 9 vehicle were compared with the FWD backcalculated modulus of these three months. Table 21 shows the comparison between the unbound layer resilient modulus obtained from the FWD backcalculation and stresses under the tandem axle of class 9 vehicle. It can be observed that the average variation between the predicted and measured modulus is around 15%. The variation may be due to the wheel wandering of the class 9 vehicle.

TABLE 21 Comparison of the backcalculated modulus and modulus obtained from the stresses under the tandem axle of class 9 vehicle

	Base Modulus (psi)		Subbase Modulus (psi)		Subgrade Modulus (psi)	
Month	FWD	Class 9	FWD	Class 9	FWD	Class 9
Mar 13	62000	54536.74	40000	33846.32	32000	35416.19
Apr 16	50200	58473.47	30400	34867.02	27600	35506.45
Aug 17	48100	58989.97	35000	39362.42	29400	35709.64

Pavement surface deflection under 9-kip test load obtained from the geophones attached to the FWD loading plate was used for the damage evaluation of the base/subbase and subgrade layer. The FWD damage indices proposed by Donovan and Tutumluer (2009) does not distinguish between the base and subbase layer. Figure 88 shows the damage of base/subbase and subgrade layer from 2015 to 2017. It can be observed that in 2015 the damage in the base/subbase layer was around 3.5% and the damage was around 15% in the subgrade layer. At the end of 2017, base/subbase damage due to traffic was around 5% while the damage in the subgrade layer was around 19%. From 2015 to 2017, within this three-year period, damage in the base/subbase accumulated at a rate of 0.63% per year and in the subgrade the damage accumulation rate was around 1.33% per year. Therefore, due to the traffic loads, the subgrade is taking more damage compared to the base and subbase layer.

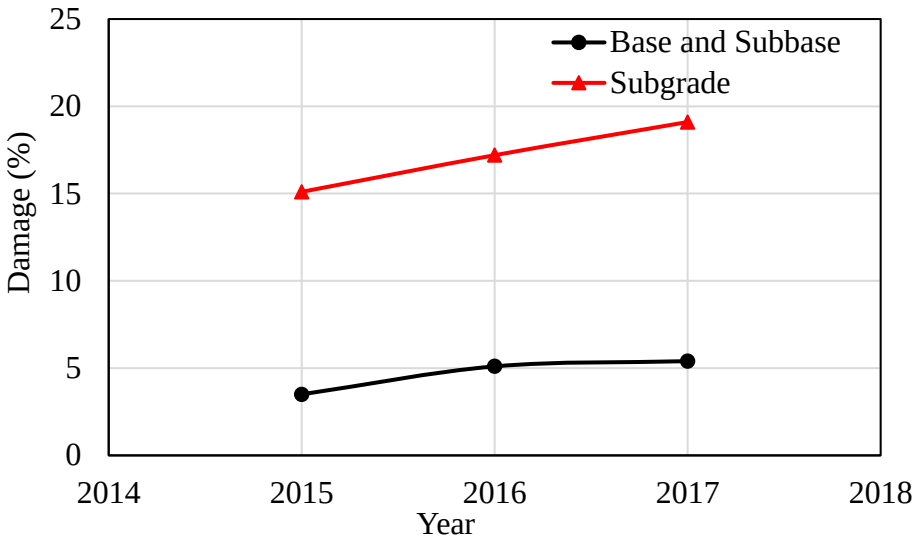

FIGURE 88 Base/Subbase and Subgrade damage index

Using FWD Modulus in Pavement ME Design

Pavement ME Design guide *(5)* is a state-of-the-art tool for designing pavements. It has mainly three inputs: traffic, climate and materials. Inputs for the materials are given at three levels. Level 1 is the user input based on the laboratory testing of the material. However, after the pavement is constructed then its performance is either evaluated by taking cores or non-destructive testing. Taking field cores and testing in the laboratory is time-consuming and labor intensive. This limitation can be overcome using non-destructive testing. Thus, incorporation of the Non-Destructive Test (NDT) tests such as FWD modulus in the pavement ME can be beneficial in continuous performance evaluation. Steps used for incorporation of the FWD modulus in pavement ME is outlined below:

AC Modulus

1) Perform the FWD test in the field. Record the temperature at which the test was conducted.
2) Collect field cores and develop the laboratory master curve *(20)*. After the test is conducted volumetric are measured from the collected cores. In this study, instead of field cores laboratory prepared cores were used.
3) At the field FWD tested temperature and frequency, determine the AC damage using Eq. (23).
4) Once the damage is determined, then fitting parameter α is updated as $\alpha' = (1 - d_j)\alpha$
5) Using the updated $\alpha'$and other parameters obtained in step 2, the field damaged master curve is obtained. This damaged master curve can be given as a level 1 input in the pavement ME design software for AC. Figure 89 shows the undamaged and damaged master curve.

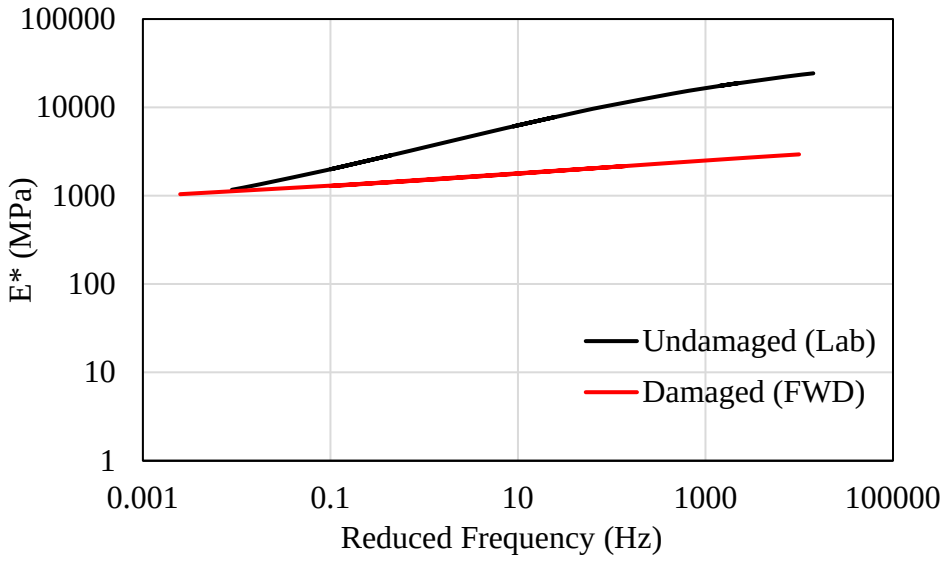

FIGURE 89 Damaged and undamaged master curve

Unbound Layers

For unbound layers, NDT FWD test results are used with a correction factor. For the granular base and subbase layers, the suggested correction factor for M_R/E_R (where, M_R is the laboratory resilient modulus and E_R is the field FWD modulus) is 0.67 and subgrade layer the correction 0.4 *(64)*.

Field obtained damaged FWD modulus for different pavement layers were used in an ME pavement analysis and were compared with the laboratory materials test results. The following results in Table 22 and Table 23 are obtained from the analysis.

TABLE 22 ME default analysis

Distress Type	Distress @ Specified Reliability		Criterion Satisfied?
	Target	Predicted	
Terminal IRI (in/mile)	172.00	86.18	Pass
Permanent deformation - total pavement (in)	0.75	0.03	Pass
AC bottom-up fatigue cracking (% lane area)	25.00	1.45	Pass
AC thermal cracking (ft/mile)	1000.00	84.34	Pass
AC top-down fatigue cracking (ft/mile)	2000.00	256.48	Pass
Permanent deformation - AC only (in)	0.25	0.00	Pass

TABLE 23 ME analysis with field damaged NDT modulus

Distress Type	Distress @ Specified Reliability		Criterion Satisfied?
	Target	Predicted	
Terminal IRI (in/mile)	172.00	191.80	Fail
Permanent deformation - total pavement (in)	0.75	0.47	Pass
AC bottom-up fatigue cracking (% lane area)	25.00	100.00	Fail
AC thermal cracking (ft/mile)	1,000.00	222.89	Pass
AC top-down fatigue cracking (ft/mile)	2000.00	2,923.73	Fail
Permanent deformation - AC only (in)	0.25	0.20	Pass

From Table 22 and Table 23, it can be seen that with default laboratory material test the pavement will last the design life of 20 years. It also shows that within the design life of 20 years no distress will occur in the pavement. However, from the field NDT FWD modulus run, it can be seen that pavement will fail in fatigue cracking.

Remarks

The following concluding remarks can be drawn from this report:

- Using the FWD data, M_R model was developed for the unbound layers. The developed models can predict the modulus of the unbound layers with 85% accuracy under any loading conditions such as traffic.
- FWD deflection data were used to quantify damage in the base and subgrade layer. It was observed that subgrade is damaging at a higher rate compared to the base layer. The base is damaging at a rate of 0.63% per year while subgrade is being damaged at 1.33% per year.
- FWD modulus was incorporated in the ME design. AC damaged modulus were incorporated as level 1 input while moduli of the unbound layers were given input as level 2. A significant difference was observed between the ME default analysis result with laboratory test input and input from the in-situ NDT FWD test.

STRATEGIC LOCATIONS FOR ADDITIONAL WEATHER STATIONS AROUND NEW MEXICO

In New Mexico, only 13 weather station data are available in the pavement ME design software. Table 24 summarizes the weather stations that are currently enlisted in ME climate data files for New Mexico. All of these data files contain old data (updated up to 2006) for a short period of time. Only four data files have data from 1996 to 2006 (10 years), one data file has data from 1997 to 2006 (9 years), three data files contain data from 1998 to 2006 (8 years) and remaining five files contain data from 2000 to 2006 (6 years).

TABLE 24 Summary of existing weather stations in New Mexico

NCDC ID	Name of Weather Station	Latitude	Longitude	Elevation	Date of data
23050	Albuquerque Intl Sun port Airport	35.041	-106.615	5310	1996-07-01
93033	Cavern City Airport	32.333	-104.258	3232	2000-12-01
23051	Clayton Municipal Airpark Airport	36.448	-103.153	4960	1996-07-01
03027	Clines Corners	35.002	-105.662	7086	1998-05-01
23078	Deming Municipal Airport	32.262	-107.720	4301	2000-08-01
23090	Four Corners Regional Airport	36.743	-108.229	5495	1998-01-01
23081	Gallup Municipal Airport	35.514	-108.794	6471	2000-10-01
23054	Las Vegas Municipal Airport	35.654	-105.141	6874	2000-10-01
23052	Raton Muni/Crews Field Apt	36.741	-104.502	6349	1998-09-01
23009	Roswell International Airport	33.307	-104.508	3649	1996-10-01
23049	Santa Fe Municipal Airport	35.616	-106.088	6344	1997-11-01
93045	Truth Or Consequences Airport	33.236	-107.268	4850	1996-10-01
23048	Tucumcari Municipal Airport	35.182	-103.603	4065	2000-09-01

Locations of these weather stations are marked in Figure 90. There are nine weather stations located in the northern New Mexico whereas four stations are located in the southern region.

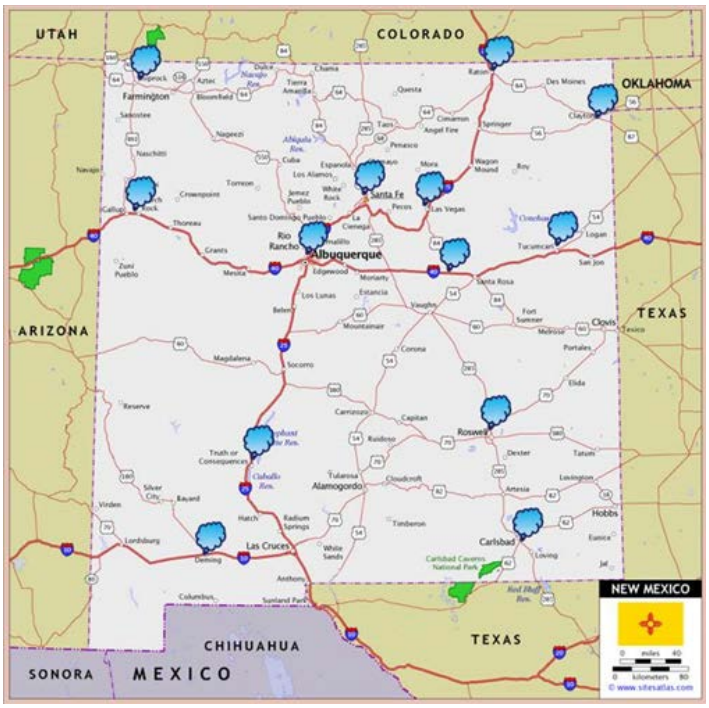

FIGURE 90 Weather Stations in New Mexico that enlisted in AASHTOWare-ME

For a particular project, climate data is obtained from the weather station close to the site. However, if there is no weather station available to a specific area, it generates the climate data by interpolation using a few nearby weather stations' data. To improve the accuracy of the interpolation, more weather stations should be included. New 11 weather stations within New Mexico can be included with the existing 13 weather stations (Table 25). Historic climatic data of these weather stations can be collected from the National Climatic Data Center (NCDC). Groundwater table data can be collected from USGS.

TABLE 25 Additional weather stations of New Mexico that can be added to ME software

NCDC ID	Weather Station	Latitude	Longitude	Elevation	Data since
93097	Alamogordo-White Sands Regional Airport	32.83	-105.99	4200	Jun-07
03034	Double Eagle II Airport	35.14	-106.79	5837	Jun-07
03035	Artesia Municipal Airport	32.85	-104.46	3541	Jun-07
23077	Clovis Municipal Airport	34.43	-103.08	4216	Jun-07
93041	Las Cruces Intl Airport	32.28	-106.91	4454	Jun-07
93091	Los Alamos Airport	35.88	-106.28	7171	Jun-07
93083	Sierra Blanca Regional Airport	33.45	-105.51	6810	Jun-07
93063	Grant County Airport	32.63	-108.16	5373	Jun-07
03012	Taos Regional Airport	36.45	-105.66	7091	Jun-07
23002	Holloman AFB Airport	32.83	-105.99	4200	Jun 07
23008	Cannon AFB Airport	34.38	-103.31	4295	Jun 07

TEMPERATURE MODEL

Measuring temperature variations of asphalt pavement is very important because AC is largely dependent on temperature. Properties of asphalt materials change sharply with temperature. Thermal expansion and contraction due to change in temperature causes fatigue damage in asphalt pavement *(65, 66)*. Transverse top-down cracking can also be seen in asphalt pavement due to the extreme decrease in temperature in a single day *(67)*. Bazlamit and Reza (2005) also showed that hysteresis components of friction, which accounts for the larger part of the total friction force in asphalt pavement, decreases with increasing temperature irrespective of the surface texture.

To evaluate the performance of roadways, transportation agencies perform regular standardized tests, i.e., FWD and setup instrumentation sections. These instrumentation sections generally measure stress-strain and temperature at different layers of asphalt pavement. Placements of these sensors are important to obtain the representative data. To evaluate the roadway performance from the standardized test data, as well as, for modeling and designing of new asphalt pavement, it is important to know the expected average temperature and its location within the asphalt layers. Moreover, it is also important to identify the temperature profile distribution within the pavement section.

Many researchers used a regression model, with atmospheric parameters as input, to calculate the temperatures within the asphalt pavement layers while many of them have also developed a model to calculate the AC surface temperature. Using solar radiation and air temperature as input, Bosscher et al. (1998), Diefenderfer (2002), Diefenderfer et al. (2006), Islam et al. (2015) and Khan et al. (2016) developed regression models to estimate the maximum and minimum pavement surface temperatures. Solaimanian and Kennedy (1993) also developed a model using the maximum air temperature and maximum solar radiation to calculate the maximum pavement surface temperature. A simulation model was developed by Hermansson (2001) to estimate the pavement temperatures for summer condition at certain depths within pavement layers. Wang (2011) developed an algorithm to obtain one-dimensional (1D) temperature profiles in a multilayered pavement system. He used thermal properties of AC, pavement depth and surface temperature as an input for his model. However, this model was validated with a very limited set of data.

The above discussion demonstrates there is no model that predicts AC pavement average temperature from surface temperature. Moreover, there is not much information in the available literature that shows at what depth this average temperature occurs. For this reason, the UNM research team was motivated to develop a model to predict the AC pavement average temperature from surface temperature and find out the depth of this average temperature. Moreover, another model was developed to predict the pavement temperature at 2-inch, 4-inch, 12-inch, 15-inch and 21-inch from the pavement surface based the pavement surface temperature.

The discussion can be summarized as follows:

1. Develop an analytical model to predict the pavement temperature at 2-inch, 4-inch, 12-inch, 15-inch and 21-inch from the pavement surface based the pavement surface temperature. In the developed model, it is assumed that the temperature varies linearly between the depths.

2. Develop a model to calculate the average temperature within the AC layer of the pavement.
3. Find out the location of the average temperature within the AC layer.

Pavement Temperature Profile

I-40 instrumentation section has temperature probes at the surface and at depth 2-inch, 4-inch, 12-inch, 15-inch and 21-inch from the pavement surface. From the weather station environmental parameters, such as air temperature, wind speed, wind direction, solar radiation, rainfall, relative humidity are also being collected. In this study, a model is generated to predict the temperature at the temperature probe locations with only surface temperature as an input.

For the development of the depth-temperature profile, Analysis of Co-Variance (ANCOVA) model is used. The rationale behind is that surface temperature is given input as a continuous variable whereas the depths are given input as a categorical variable. Before starting the model development, it is important to identify whether depth and surface temperature individually varies with the pavement depth temperature profile or does the interaction between depth and surface temperature also affects the pavement depth temperature profile. For the model generation, full one-year data from 2013-2014 is used.

Figure 91 shows the variation of temperature at depth 2-inch, 4-inch, 12-inch, 15-inch and 21-inch from the top of the pavement with the surface temperature. In Figure 91, the depths are represented as ranks. Rank 1 denotes temperature at depth 2 inch inside the pavement from top surface, rank 2 denotes temperature at depth 4 inch inside the pavement from top surface, rank 3 denotes temperature at depth 12 inch inside the pavement from top surface, rank 4 denotes temperature at depth 15 inch inside the pavement from top surface and rank 5 denotes temperature at depth 21 inch inside the pavement from top surface. Figure 91 also shows that surface temperature varies more with the temperature at depth 2-inch, 4-inch and 21-inch from top surface. However, surface temperature varies less with the temperature at depth 12-inch and 15-inch from the top surface. The slopes of the lines in Figure 91 are not equal, therefore, it suggests the interaction of depth and surface temperature may be important in the prediction of the depth temperature profile of the pavement.

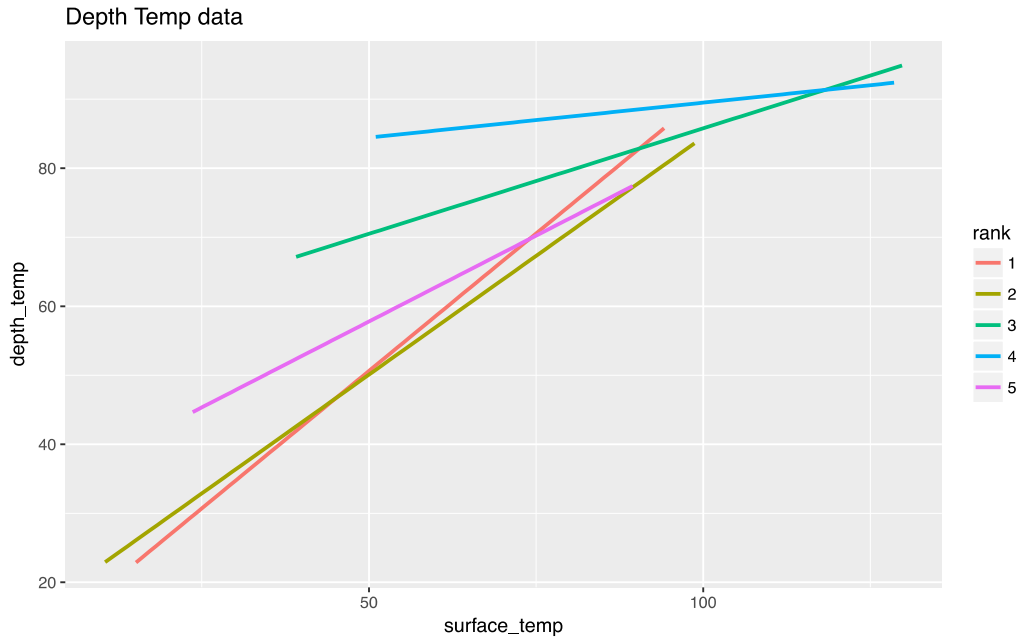

FIGURE 91 Variation of pavement depth temperature profile with surface temperature.

In developing any regression model, it is important to assess the model assumptions. The model assumptions are:

a) No pattern in the residual analysis
b) Equal variance
c) No presence of any highly influential observations from cook's distance and leverage plot
d) The Linearity of the QQ plot to satisfy the normality assumption.

First a simple model with only the main term of depth and surface temperature is developed. The model is:

$$\begin{aligned} &\textit{Temperature at depth} = 26.7 + 0.46 \times \textit{Surface temperature} + 0.41 \times (\boldsymbol{I_2} \\ &= \textit{depth 4 inch}) + 15.6 \times (\boldsymbol{I_3} = \textit{depth 12 inch}) + 20.7 \times (\boldsymbol{I_4} = \textit{depth 15} \\ &\textit{inch}) + 8.2 \times (\boldsymbol{I_5} = \textit{depth 21 inch}) \end{aligned} \tag{64}$$

Now model assumptions of Eq. (64) will be assessed.

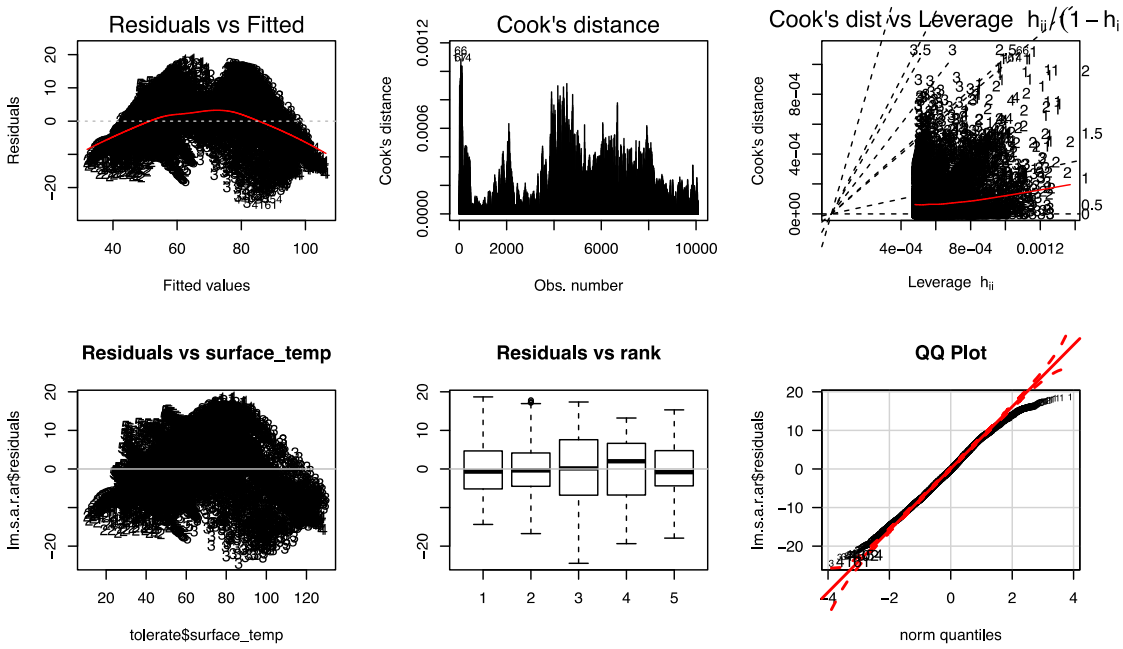

FIGURE 92 Model Assumptions of Eq. (64)

Although residual vs rank and QQ plot satisfies the equal variance and normality assumptions, but the residual vs. fitted curve shows a downward pattern in Figure 92. Moreover, there is some presence of highly influential observations as seen from the cook's distance plot. These suggest a violation of the model assumptions (a) and (c). The value of adjusted R^2 and RMSE (Root Mean Squared Error) of Eq. (64) is not important as the model assumptions are not met.

Now a second model was developed after removing the highly influential observations and including the interaction terms of depth and surface temperature.

$$\begin{aligned} &\textit{Temperature at depth} = 10.792 + 0.796 \times \textit{surface temp} + 4.882 \times (I_2 = \\ &\textit{depth 4 inch}) + 44.776 \times (I_3 = \textit{depth 12 inch}) + 68.589 \times (I_4 = \textit{depth 15} \\ &\textit{inch}) + 22.107 \times (I_5 = \textit{depth 21 inch}) - 0.108 \times \textit{surface temp} \times (I_2 = \textit{depth} \\ &\textit{4 inch}) - 0.494 \times \textit{surface temp} \times (I_3 = \textit{depth 12 inch}) - 0.695 \times \textit{surface} \\ &\textit{temp} \times (I_4 = \textit{depth 15 inch}) - 0.299 \times \textit{surface temp} \times (I_5 = \textit{depth 21 inch}) \end{aligned} \quad (65)$$

Now model assumptions of Eq. (65) will be assessed.

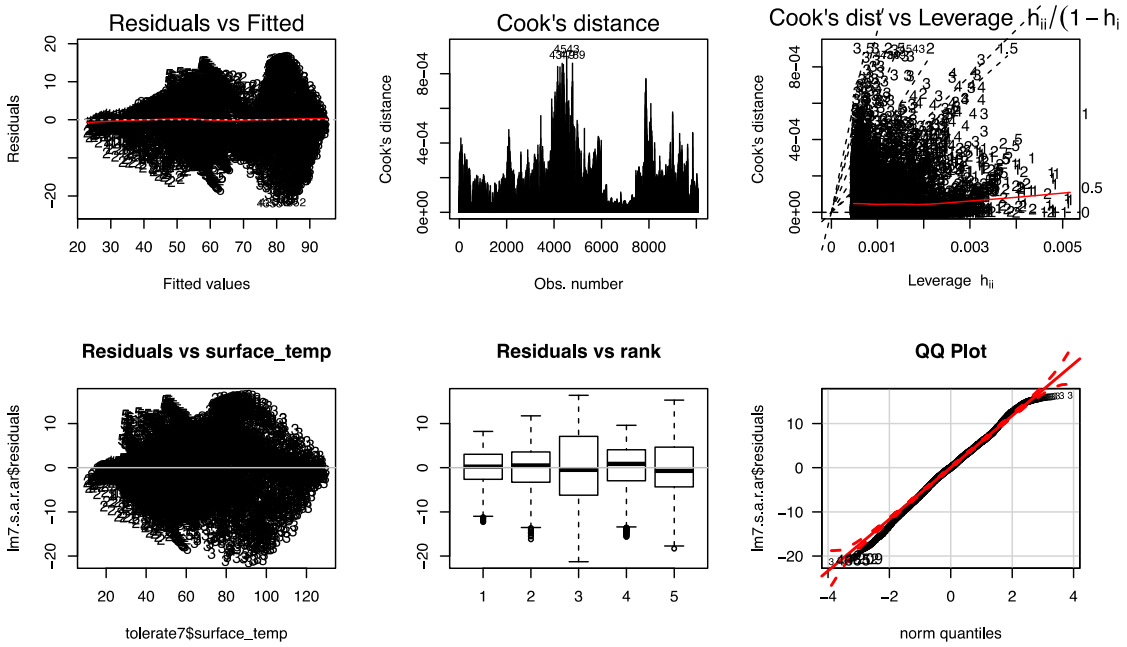

FIGURE 93 Model Assumptions of Eq. (64)

From Figure 93, it is observed that residual vs. fitted does not show any pattern, nor cook's distance plot shows any highly influential observations. QQ plot and residual vs. rank plot also does not show significant variation from the model assumptions. Therefore, we can conclude that Eq. (65) satisfies all the model assumptions and it is an accurate representation of the data. Regression coefficient value (R^2) of Eq. (65) was obtained to be 0.9. This suggests that the model explains 90% variability in the data. All the terms in Eq. (65) has a *p*-value less than 0.05. Therefore, all the terms in the equation are significant to describe the variation in data at 95% confidence interval.

The final equations for temperature at depth 2-inch, 4-inch, 12-inch, 15-inch and 21-inch can be written out in five simple equations as follows:

$$\text{Temperature at 2-inch} = 10.792 + 0.796 \times \text{surface temp} \quad (66)$$

$$\text{Temperature at 4-inch} = 0.674 + 0.688 \times \text{surface temp} \quad (67)$$

$$\text{Temperature at 12-inch} = 25.568 + 0.62 \times \text{surface temp} \quad (68)$$

$$\text{Temperature at 15-inch} = 29.381 + 0.501 \times \text{surface temp} \quad (69)$$

$$\text{Temperature at 21-inch} = 32.899 + 0.497 \times \text{surface temp} \quad (70)$$

Model Validation

The developed regression model was validated using the field data collected from October 2014 to June 2015. For Eq. (66), the Root Mean Squared Error (RMSE) of the predicted and estimated

value was found to be 5.6 °F. In Figure 94, a 45° line passing through the origin was drawn to show the distribution of the measured and predicted values at 2-inch depth.

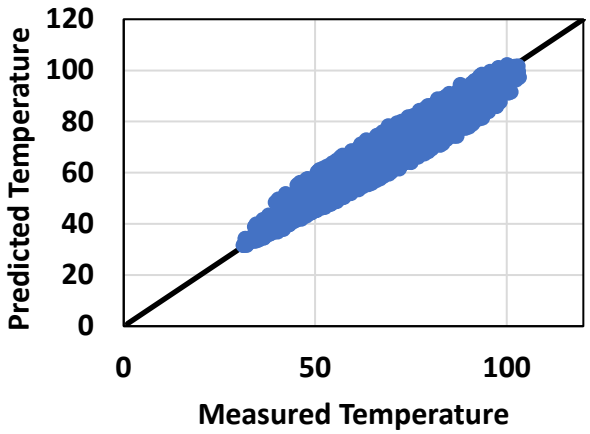

FIGURE 94 Model Validation of Temperature at 2-in

For Eq. (67), the RMSE of the predicted and estimated value was found to be 7.5 °F. In Figure 95, a 45° line passing through the origin was drawn to show the distribution of the measured and predicted values at 4-inch depth.

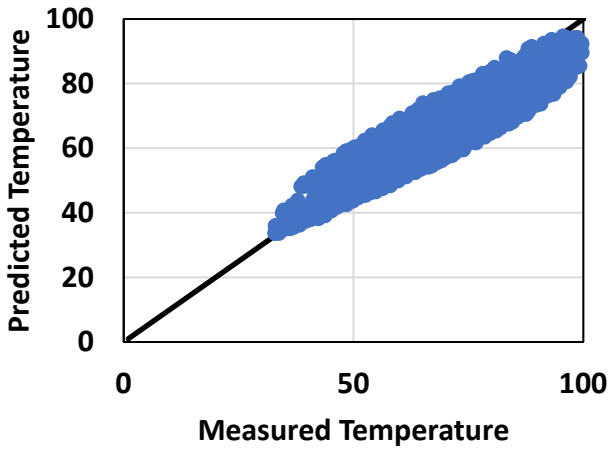

FIGURE 95 Model Validation of Temperature at 4-in

For Eq. (68), the RMSE of the predicted and estimated value was found to be 9.7 °F. In Figure 96, a 45° line passing through the origin was drawn to show the distribution of the measured and predicted values at 12-inch depth.

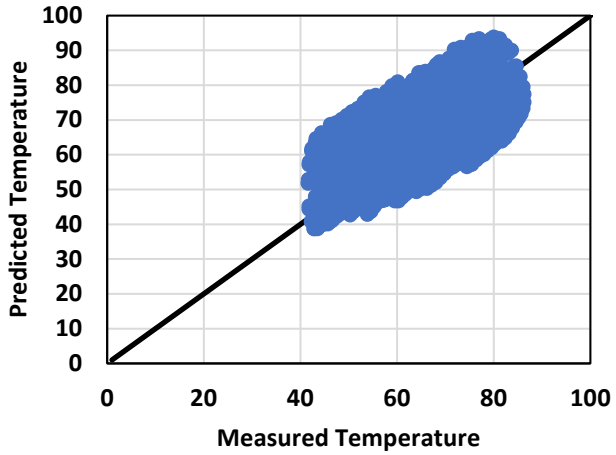

FIGURE 96 Model Validation of Temperature at 12-in

For Eq. (69), the RMSE of the predicted and estimated value was found to be 8.9°F. In Figure 97, a 45° line passing through the origin was drawn to show the distribution of the measured and predicted values at 15-inch depth.

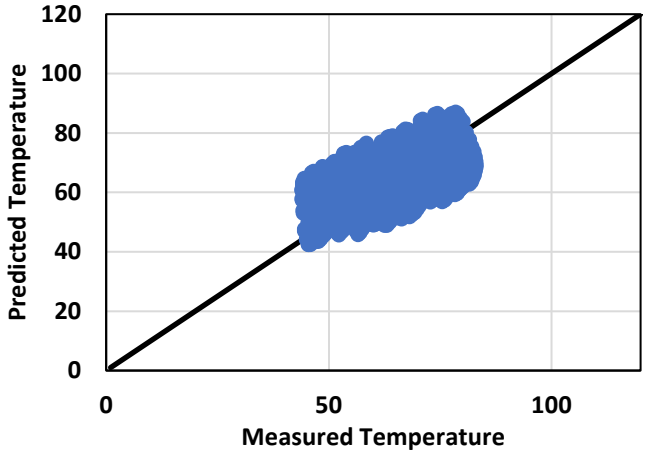

FIGURE 97 Model Validation of Temperature at 15-in

For Eq. (70), the RMSE of the predicted and estimated value was found to be 8.8°F. In Figure 98, a 45° line passing through the origin was drawn to show the distribution of the measured and predicted values at 21-inch depth.

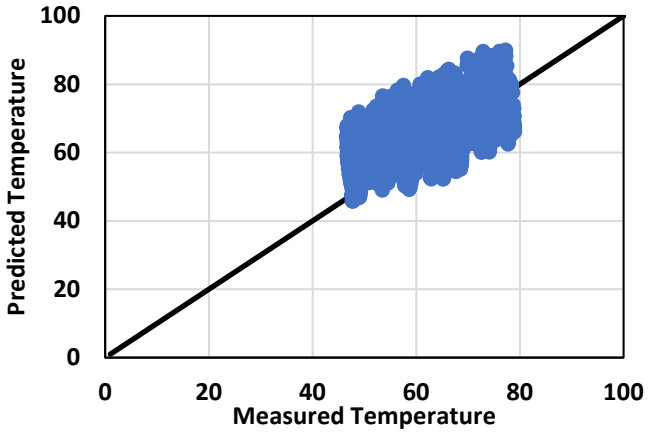

FIGURE 98 Model Validation of Temperature at 21-in

Asphalt's Average Temperature

A regression model was developed to determine the average temperature within the asphalt using pavement surface temperature. Full one-year data from October 2012 to October 2013 was used to develop the regression model using the MATLAB. The developed model is mentioned below:

$$T_{avg} = 11.65 + 0.8T_s \quad (71)$$

where T_{avg} is the average temperature within asphalt pavement layers (°F) and T_s is the AC surface temperature (°F). In this regression model, there were 16762 numbers of observations. The RMSE was found to be 5.68 °F and the coefficient of regression, R^2 value was found to be 0.94, which is very high.

Model Validation

The developed regression model was validated using the field data collected from October 2014 to June 2015. The RMSE of the predicted and estimated value was found to be 4.88 °F, which is negligible. In Figure 99, a 45° line passing through the origin was drawn to show the distribution of the measured and predicted average pavement temperature.

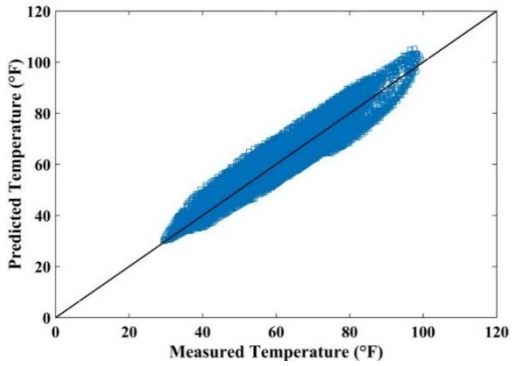

FIGURE 99 Measured and predicted average AC temperatures

One Way Analysis of Variance (ANOVA) test was conducted to further validate the model. The null hypothesis was that the predicted value and measured values are statistically equal. The *p*-value (probability of the null hypothesis be true) from the ANOVA test was found to be 57.3%, which is more than 5%. Therefore, the predicted value and measured values are statistically equal. Figure 100 shows the ANOVA distribution graph. Normality of the dataset is a prerequisite of the ANOVA test. However, this test can be skipped if the data set is very large *(77, 78)*. In addition, in a large sample size, distribution of the data does not affect the outcome *(79)*.

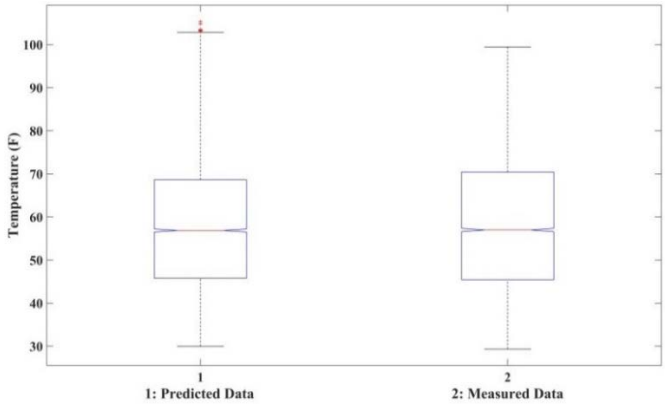

FIGURE 100 ANOVA distribution

Depth of Average Asphalt Temperature

Another study was conducted to calculate the depth within the pavement at which average temperature of the whole pavement structure can be obtained. One-year data from October 2012 to October 2013 were used in the study. From the analysis, it was found that average temperature ranges from just below the asphalt surface up to 8 inches within the pavement layers. Distribution of measured average temperature of pavement layers against their positions (depth) within pavement is shown in Figure 101. The 90th percentile of the average depth within asphalt pavement layers was found to be at 4.20 inches and the mean depth was 2.546 inches for the average temperature within the studied period.

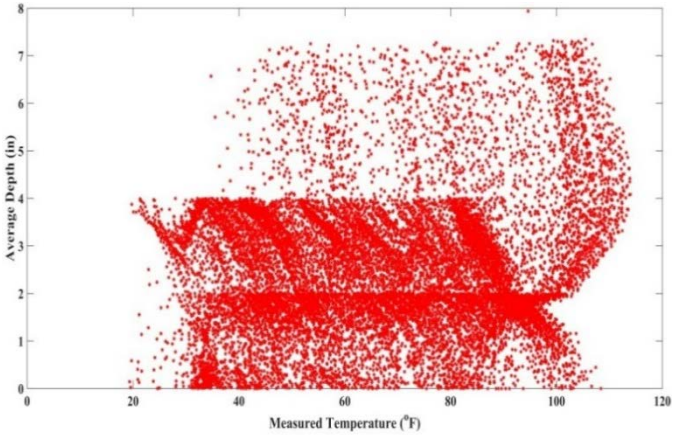

FIGURE 101 Distribution of average temperature along with the pavement depth

Model Validation

The obtained mean depth was validated using the data from October 2014 to June 2015. Average temperature within asphalt pavement layers were compared with the temperature at mean depth (2.546 inches) in this period. Figure 102 shows the distribution between the predicted temperature at the mean depth of 2.546 inches inside the asphalt pavement and the average temperature of the whole asphalt pavement layers. The RMSE between these two temperatures was found to be 5.5 °F.

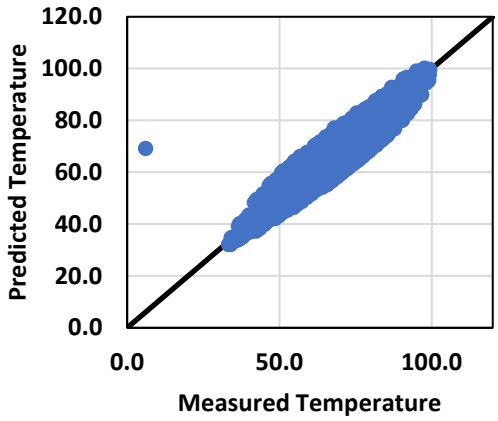

FIGURE 102 Distribution of predicted temperature and measured temperature

Remarks

For this study, two analytical temperature models were developed. One model was developed to generate the temperature profile inside the pavement. Another model determines the average temperature in AC. Both the models were developed using the data collected from the I-40 instrumentation section. The developed model was validated using further temperature data that were not used to develop the equations. It was also found that the mean depth for average temperature within asphalt pavement was at 2.54 inches.

THIS PAGE LEFT BLANK INTENTIONALLY

LABORATORY CHARACTERIZATION OF FIELD SAMPLES

INDIRECT TENSILE TEST ON PASSING LANE AC CORES

In December 2018, a total of 8 cores was collected from the passing lane at the I-40 instrumentation section. Among these 8 cores, 4 cores were collected from the shoulder and 4 were collected from the passing lane. All the cores were debonded in at least at one of the lifts, and some of the cores were both debonded and cracked. Of the 4 passing lane cores, two were cracked and two were debonded only at the first lift with no crack. The top layer AC from the latter cores was used for the indirect tensile test (IDT).

Creep compliance and IDT are the major input for the AASHTOWare ME design guide for low temperature or thermal cracking module. In this study, creep compliance of the top lift AC of the passing lane was determined using the IDT test. Creep compliance is the time-dependent strain of the material under unit stress. This test is conducted according to AASHTO T322-07 *(80)*. Although AASHTO requires the test to be conducted at several temperatures, for this study, the tests were conducted at room temperature, around 25°C. The results from this test were compared with the field sensor obtained creep compliance.

One of the fundamental material properties of the viscoelastic AC is dynamic modulus. It is a required input for ME analysis. This property describes the time and frequency dependent property of the AC. To perform dynamic modulus test on AC according to AASHTO T-342 *(81)*, the sample must be at least 4 inches in height. However, the AC cores collected from the field were only 3.5 inches in height. Furthermore, the sample must be cut from the top and bottom to have a smooth end on both sides, thus, making it very difficult to perform dynamic modulus on the field collected AC samples.

For the IDT test, AC cores were collected from the field. The field collected AC samples were already 6 inches in diameter, however, the samples were cut on both sides to have a thickness of 2 inches After the samples were cut, two LVDTs were attached to the sample in both horizontal and vertical direction and the gage length was 38 mm. Figure 103 shows the IDT sample before the start of the test.

FIGURE 103 IDT sample

Creep compliance is measured as a function of horizontal and vertical displacement, the dimension of the specimen and the static creep load. Creep compliance determination equation from the IDT test is shown in Eq. (72)

$$D(t) = \frac{H \times D \times t}{P \times GL} \times C \tag{72}$$

here, *H* is the horizontal deflection, *D* is the diameter, *t* is the thickness of the sample, *P* is applied load, *GL* is the gage length and *C* is the correction factor for sample bulging.

Once the creep compliance is obtained it can be used to numerically interconvert to the dynamic modulus. Researchers have used IDT creep compliance to obtain the dynamic modulus of the AC *(82, 83)*. Once the prony series parameters are obtained from the creep compliance curve, the dynamic modulus can be obtained using the following equations:

$$D'(\omega) = D_0^P + \sum_{i=1}^{n} \frac{D_i^P}{\omega^2 \tau_i^2 + 1} \tag{73}$$

$$D''(\omega) = \sum_{i=1}^{n} \frac{\omega \tau_i D_i^P}{\omega^2 \tau_i^2 + 1} \tag{74}$$

here ω is angular frequency, D' and D'' are the real and imaginary parts of the complex compliance. Once these parameters are obtained, the dynamic modulus is obtained from Eq. (75):

$$|E^*(\omega)| = \frac{1}{\sqrt{D'(\omega)^2 + D''(\omega)^2}} \tag{75}$$

Once the field creep compliance data is available, then it can be fitted in creep compliance prony series to obtain the creep parameters. After that, numerical interconversion is applied to obtain the dynamic modulus. Figure 104(a) shows the creep compliance curve of the field aged AC collected

in December 2018 and Figure 104(b) shows the field creep compliance curve obtained from the instrumentation sensor. These two curves were fitted to a 7-parameter generalized Kelvin model to obtain creep parameters. The nonlinear least square curve fitting with trust region algorithm was performed in MATLAB. The fitting yielded a coefficient of determination (R^2) value of 0.98 in both instances. It suggests that the fitted model can explain 98% variability in the data. Once the creep compliance parameters (D_g, D_1, D_2, and D_3) and retardation times (τ_1, τ_2, and τ_3) were known, then using Eq. (73) to Eq. (75) dynamic modulus were determined. Detailed equations of this procedure can be obtained elsewhere *(84)*.

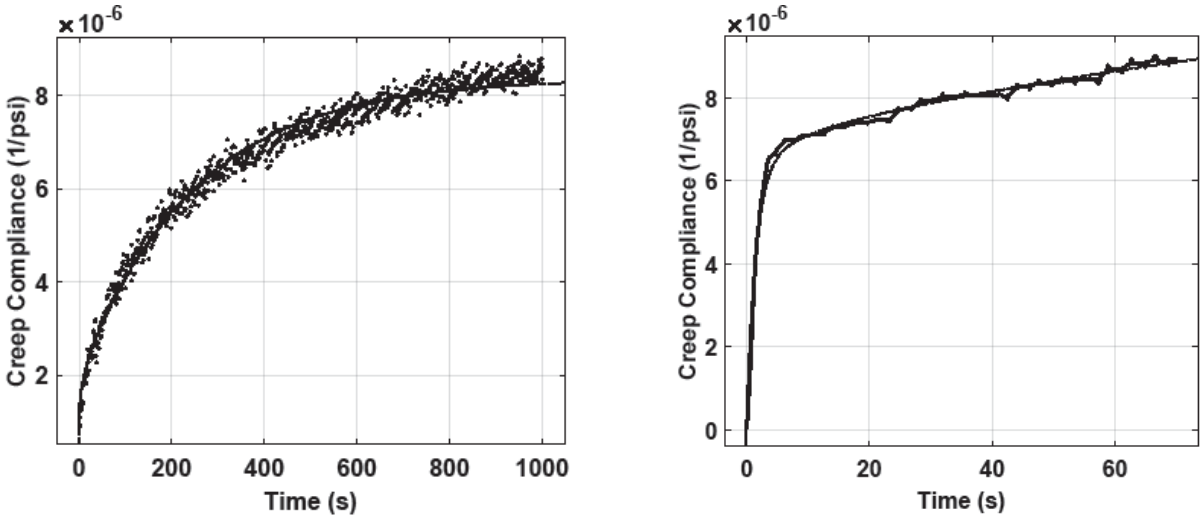

(a) Field sample (b) Instrumentation sensor

FIGURE 104 Creep Compliance obtained from IDT and instrumentation sensor

Table 26 shows the creep parameters obtained from these two methods.

TABLE 26 Creep Parameters

Parameters	IDT	Field Sensor
D_g (1/psi)	4×10^{-7}	3.45×10^{-7}
D_1 (1/psi)	1×10^{-6}	6.019×10^{-6}
D_2 (1/psi)	5.662×10^{-7}	7.036×10^{-7}
D_3 (1/psi)	6.397×10^{-6}	6.093×10^{-6}
τ_1 (sec)	0.5	1.522
τ_2 (sec)	13	10
τ_3 (sec)	250	200

Table 26 shows a good agreement between the creep parameters of AC obtained from the IDT and field sensor. Figure 105 also shows a good agreement between the test methods in terms of dynamic modulus.

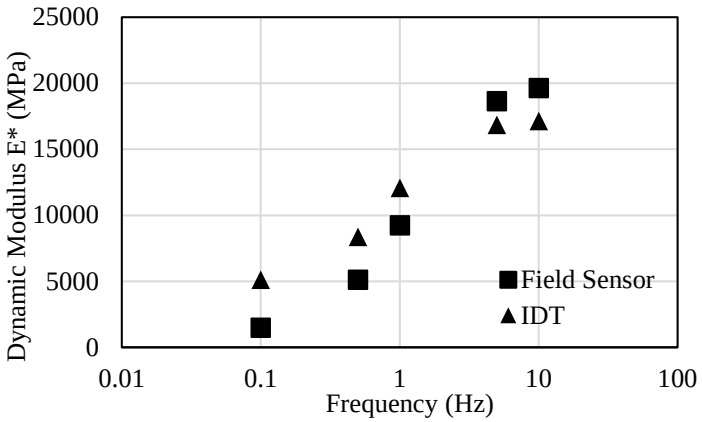

FIGURE 105 Dynamic modulus of AC

Figure 105 and Table 26 shows good agreement between the results of viscoelastic properties of AC obtained from laboratory test and field instrumentation sensor obtained data. This suggests that field sensor obtained data can accurately predict the material properties. This test further validates the data obtained from the instrumentation sensor.

THERMAL STRESS RESTRAINED SPECIMEN TEST

Thermal stress developed in AC is of primary concern in low-temperature region or where day-night temperature cycles change rapidly. Researchers have successfully used the Thermal Stress Restrained Specimen Test (TSRST) test to determine the low-temperature susceptibility of the AC *(85, 86)*. The main type of distress on the collected cores in 2016 and 2018 are delamination and thermal cracking. Most of the cores collected within the above-mentioned time frame from the instrumentation section are from the shoulder. As there is no significant traffic on the shoulder, therefore, it can be said that the distresses, i.e., cracking and delamination, are due to the thermal loading alone. Once it can be clearly said that the distresses are arising from the thermal stresses, then the next question arises: which of these two distresses are occurring first? To answer this question, the TSRST test is conducted on the field collected delaminated samples. To replicate the field tack coat, the delaminated samples are glued together using PG 76-22 binder, as used in the I-40 instrumentation section, as shown in Figure 106.

FIGURE 106 Sample preparation for the TSRST test

In the TSRST test, the sample is restrained at top and bottom from contracting due to the temperature change. This creates tensile stress inside the specimen. When the built-up stress inside the pavement exceeds the limit, the sample fails. From the TSRST test on the field sample, it was observed that the sample failed at the bond between the two AC lifts at around -22°C, which suggests delamination occurs first in the field. Figure 107 shows the sample after the TSRST test.

FIGURE 107 Delamination in the TSRST test

Furthermore, cores collected from the I-40 westbound during SHRP-2 project also showed delamination without cracking in any AC lifts, which is shown in Figure 108.

FIGURE 108 I-40 westbound cores collected during SHRP-2 Project in 2017

PERMEABILITY TEST ON FIELD AC

AC pavements are vulnerable to excessive permeability induced damage. Excessive permeability can induce stripping and cracking in AC due to the increasing amount of pore pressure *(87, 88)*. In this study, permeability was determined through the falling head test on the field collected AC samples. The field AC cores were collected in 2016 and 2018. The coefficient of permeability for laminar flow is determined using a variation of Darcy's law, as shown in Eq. (76).

$$k = 2.303 \frac{aL}{A\Delta t} \log\left(\frac{h_{t0}}{h_{t1}}\right) \quad (76)$$

here, a is the cross-section of the stand pipe, A is the cross-section of the sample, h_{t0} and h_{t1} are the upper and lower water level in the stand pipe after time Δt and L is the sample height.

Figure 109 shows the steps involved in the permeability test. At first, the samples were saturated using a mechanical shaker. Then the samples were coated on the side to reduce/block any sideways movement of water. It is done to simulate the top-down movement of water in field conditions. After that, the sample was placed on the falling head test machine. Figure 109 shows the steps involved in the falling head permeability test on AC. After placement of the sample, the pressure is built inside the chamber to force the 1-D movement of water. During this time, the flow of water in the standpipe is measured for a certain period Δt. After that, using Eq. (76), the coefficient of permeability k is determined.

(a) Coated sample

(b) saturating the sample

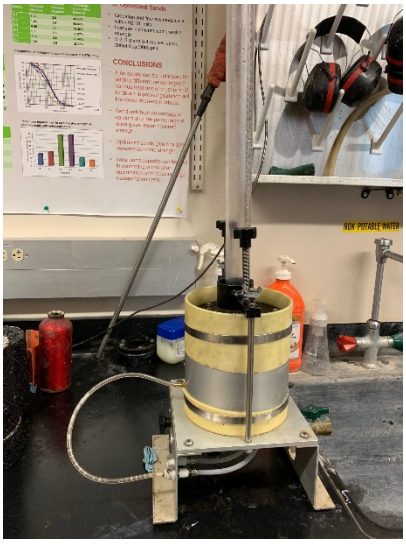

(c) Falling head test

FIGURE 109 Permeability test on field AC sample

Figure 110 shows the coefficient of permeability of the field AC samples obtained in 2016 and 2018. In 2016, the coefficient of permeability of the AC samples was around 135×10^{-5} cm/sec; and after two years, the coefficient of permeability increased to around 160×10^{-5} cm/sec. The increase in permeability may be due to the damage of the AC layer, such as aging. Aging decreases the AC film thickness around the aggregate and continuous temperature cycle change induce microdamage in the AC. These microcracks in the AC increase its permeability and reduces the strength *(89)*.

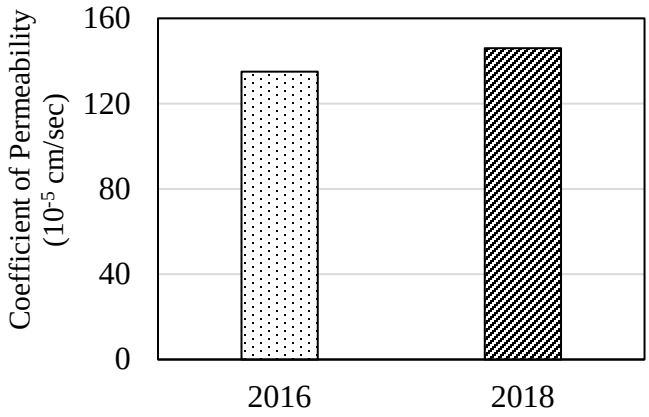

FIGURE 110 Coefficient of Permeability of field AC sample

TEST ON BINDER

Aging of Binder

To determine the extent of filed aging, the binders were extracted from the field collected cores. The cores were collected from the shoulder of the I-40 field instrumentation section. The binders were extracted from the AC cores using ASTM D2172 *(90)* and recovered using ASTM D5404 *(91)*. According to this process, 1500g of AC mixture was placed in a bowl and covered with 600 ml of trichloroethylene. The bowl was left to rest for around 45 minutes and then it was placed and clamped in the centrifuge. The speed of the centrifuge was gradually increased to 3600 rpm and the centrifuge was kept functional until the solvent stopped draining. After that, around 200 ml of trichloroethylene was further added to the centrifuge bowl and the above procedure was repeated at least 3 times. After this, a second centrifuge was used to extract the fines from the solvent. For the last step, a rotary evaporator was used to separate the trichloroethylene from the binder. The steps involved in binder extraction from field cores are shown in Figure 111.

(a) Asphalt mix in Trichloroethylene

(b) Separation of Aggregate

(c) Fines separation through centrifuge

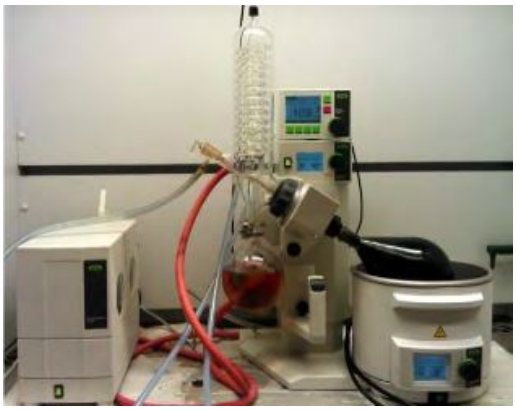

(d) Extraction of binder through rotavapor

(e) Extracted Binder

(f) Rheological testing in DSR

FIGURE 111 Binder Extraction Procedure

After the extraction, unaged and field aged binders were tested in the Dynamic Shear Rheometer (DSR) for rheological properties *(92)*. The comparison between the field aged and unaged binder is shown in Figure 112. From Figure 112, it can be said that the modulus of the field aged binder is relatively higher at the lower frequency compared to the unaged binder. The increment of complex modulus for the field binder is due to the aging effect. Although at lower reduced frequencies, the difference in complex modulus of field aged and unaged binder is higher, but at a reduced frequency greater than 1000 Hz, both the binders have almost same complex modulus. This is due to the viscoelastic nature of the asphalt binder. At lower frequency, when loading time is higher, the viscoelastic part of the binder dominates and the difference between the complex modulus become significant. However, at a higher frequency, when loading time is lower, the elastic part of the binder dominates.

Crossover frequency can be used to have an idea of the extent of aging in the binders extracted from field cored samples. The crossover frequency is the measure of the hardness of the binder. Modulus at the crossover frequency can be defined as the frequency when the loss modulus equals to the storage modulus and phase angle reaches 45°. A lower crossover frequency represents a harden binder and a higher crossover frequency represents a softer binder. For field aged binder, crossover frequency is around 10 Hz and complex modulus around 0.89 MPa, whereas, for unaged binder, the crossover frequency is around 23300 Hz and complex modulus around 12.7 MPa. The rheological index *R* could not be identified as the test was not conducted at a lower temperature than 4°C. However, from the crossover frequency, it can be said that within 4 years the asphalt binder has aged significantly; and crossover frequency and complex modulus has reduced by 2330 and 15 times.

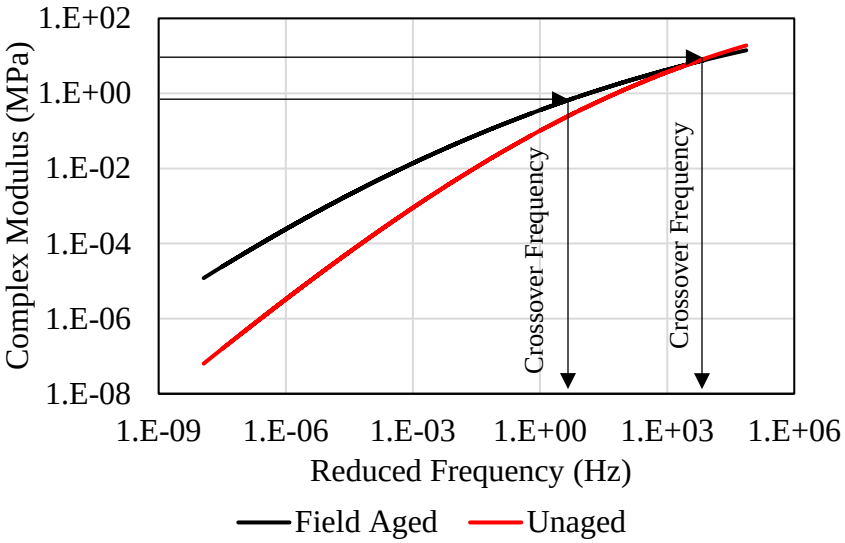

FIGURE 112 Comparison between field aged and unaged asphalt binder

Relaxation Modulus Comparison

Stress relaxation is the ability of a material to reduce stress after application of a constant amount of strain for a certain period of time. Stress relaxation phenomenon can be used to extract the material property of the viscoelastic material like asphalt concrete or asphalt.

In this study, relaxation modulus obtained from the field aged binder and unaged binder were compared. Moreover, this study also compares the relaxation modulus obtained from the field instrumentation sensor response under the constant load from FWD loading plate and field aged extracted binder.

Figure 113 shows the relaxation modulus comparison between unaged and field aged binder. It can be seen from Figure 113 that due to aging binder becomes stiff and it takes a longer time to release stress. For instance, in an unaged binder, the modulus reduces to 71 Pa within 300 seconds whereas, for aged binder, modulus reduces to 71 Pa in 1000 seconds. Therefore, due to four years of field aging, to reduce to the same amount of stress of 71 MPa, 600 seconds more time is required for field aged binder.

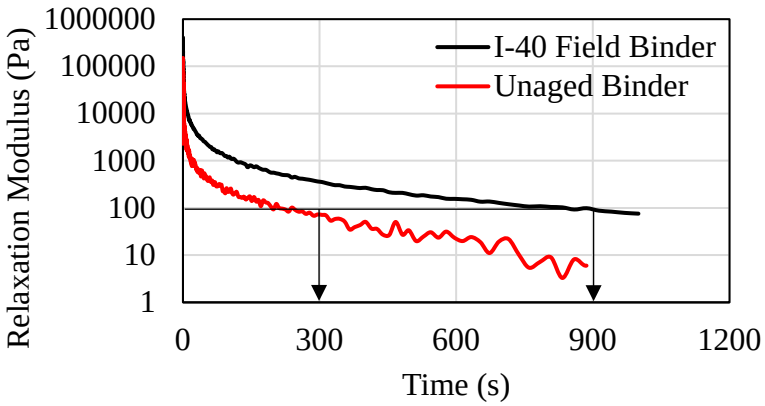

FIGURE 113 Comparison of relaxation modulus of field aged and unaged binder

Figure 114 shows the comparison between the relaxation modulus obtained from the field sensor on AC and field aged binder. It is important to mention that relaxation modulus of AC in the field is obtained by testing in the large scale whereas binder testing in DSR is conducted on a much smaller scale. It can be also observed from Figure 114 that scale of initial relaxation modulus is in the order of 10^6 psi in the field AC; whereas in binder level, the scale is in the order of 10^1.

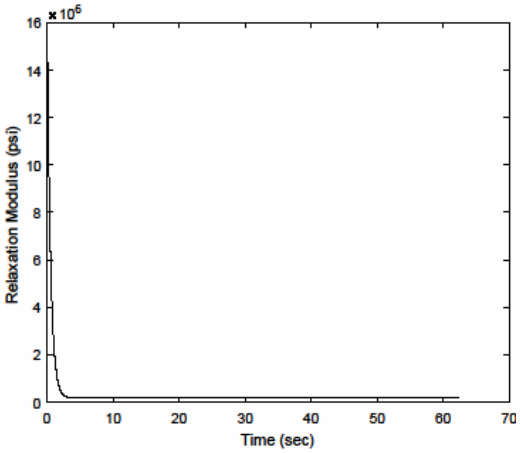

(a) AC from Field Sensor

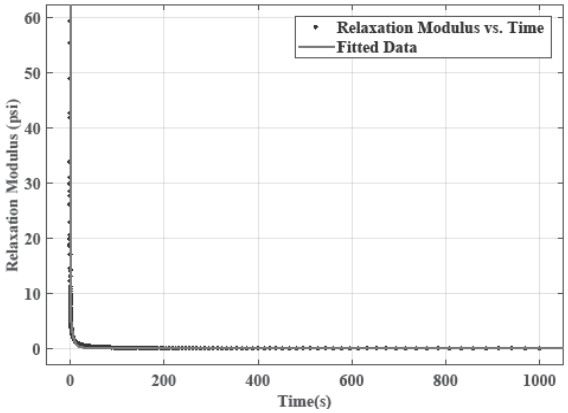

(b) Field Aged Binder

FIGURE 114 Comparison of relaxation modulus of AC in field and field aged binder

Fitting the relaxation modulus, relaxation parameters for both the scales of material, AC and binder, is shown in Table 27. As explained earlier, instantaneous modulus for the AC and binder has a scale difference of around 10^5 psi. Furthermore, a significant difference was observed between other relaxation parameters as well. For instance, due to the pure viscoelastic nature of binder, relaxation time in field aged asphalt binder is much higher compared to the AC.

TABLE 27 Relaxation Modulus Parameters

	Field Aged AC from Sensor	Field Aged Binder from DSR
Instantaneous Modulus (psi)	1.1×10^{6}	86
$\overline{g}_1$	0.99	0.81
$\overline{g}_2$	5.96×10^{-7}	0.18
$\overline{g}_3$	4.92×10^{-8}	0.04
Relaxation time (sec), ρ_1	0.91	0.103
Relaxation time (sec), ρ_2	26	1.55
Relaxation time (sec), ρ_3	80	1000

TEST ON SUBGRADE SOIL

In summer 2018, when AC cores were collected, some subgrade soil samples were collected as well. Collection of the soil sample is shown in Figure 115.

(a) (b)

FIGURE 115 Collection of Soil Sample from I-40 Instrumentation site

Soil samples were collected from three locations. The locations are marked in Figure 116. Soil collection locations are marked in a circle. Two soil samples were collected from Mile Post (MP) 141. One from the shoulder while the other was off the shoulder. The other two soil samples were collected from near MP 140.9 and MP 140.6.

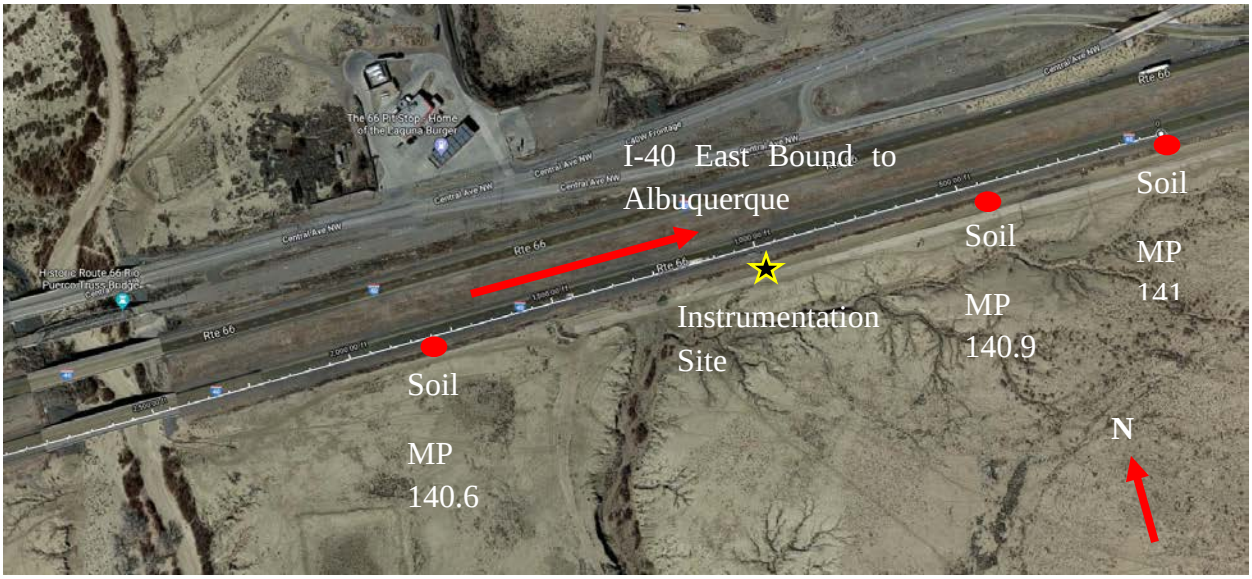

FIGURE 116 Soil Sample collection sites on I-40 Instrumentation section

After collection of the soil samples, field moisture contents were determined, and the values are given in Table 28. The gravimetric moisture contents for the soil near MP 141 were around 4%, and for soil samples near MP 140.6 and MP140.9, gravimetric moisture contents were found to be around 13%. Soil near MP 141 was more sandy and soil near MP 140.6 140.9 were more clayey in nature.

TABLE 28 Field Moisture content

Mile Post	Field Moisture Content (%)
141	5
141 (off Shoulder)	3.4
140.9	12.5
140.6	13

Sieve analysis was conducted on the collected soil samples. The sieve analysis was conducted according to ASTM D6913 *(93)*. Oven drying method was used for sieve analysis. The particle size distribution of the soil near MP 141 is shown in Figure 117. From Figure 117, it can be observed that most of the particle retained on between #4 and #200 sieve. The amount of fines present in the soil were less than 5%.

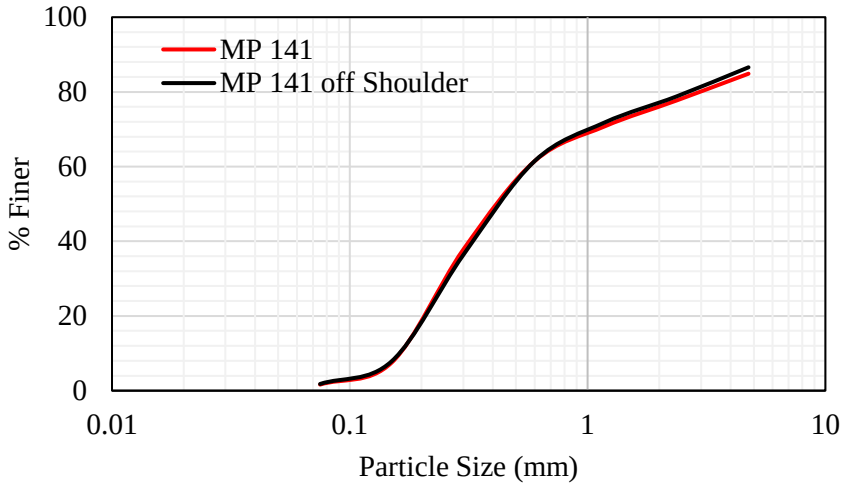

FIGURE 117 Sieve Analysis on the soil from MP 141

However, soil samples collected near MP 140.9 and MP 140.6 could not be sieved. After oven drying the samples were too stiff to break by mortar or hand. Even after sieving most of the large chunk of clays were retained on #4 sieve, as it can be seen on Figure 118. Particles retained on #4 sieve were not aggregates rather they were large chunks of clayey soil. Due to the limitation of the amount of soil samples, repeat sieve analysis was not conducted on the soil samples from MP 140.9 and MP 140.6.

(a) (b)

FIGURE 118 Soil from MP 140.9 and 140.6

Atterberg's limit test *(94)* was conducted on the soil samples collected from MP 141 and MP 140.6. Atterberg's limit test is conducted to determine the nature of the soil. Figure 119 shows the graph to determine the liquid limit (LL) of the soil samples. From Table 29, it can be observed that the soil from MP 141 has a LL of 14, whereas the soil from MP 140.6 has LL of around 33. Furthermore, the plasticity index (PI) of the soil near MP 141 was around 2, whereas soil near 140.6 has a PI of around 24. It suggests that the soil near MP 140.6 is highly plastic and it has high clay content compared to the soil near MP 141. From sieve analysis and Atterberg's limit, the soil near MP 141 is A-2-4 soil. However, as the sieve analysis could not be conducted on the soil near MP 140.6 or MP 140.9, the probable soil classification may be A-2-6 or A-6 soil based on the LL and PI. According to the USGS classification, the soil near MP 140.6 is CL (low plasticity clay).

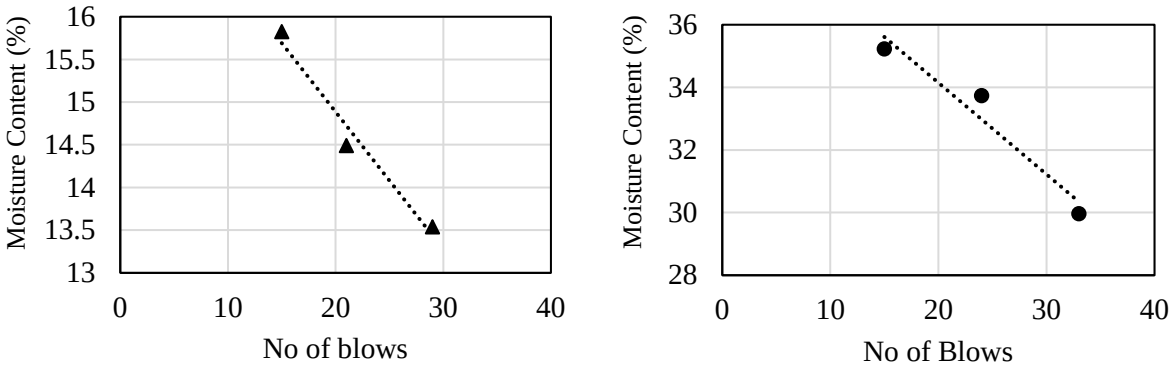

(a) Soil from MP 141 (b) Soil from MP 140.6

FIGURE 119 Liquid limit determination of soil samples

TABLE 29 Atterberg's limit of soil samples

Mile Post	Liquid Limit (%)	Plastic Limit (%)	Plasticity Index (PI)
141	14	12	2
140.6	32.8	9.2	23.6

Modified Proctor test *(95)* was conducted on the soil near MP 140.6 to determine the optimum moisture content. Figure 120 (a) shows the soil sample after removal from the mold and Figure 120 (b) shows the optimum moisture content (OMC) of the soil sample. The OMC of the soil sample near MP 140.6 was found to be around 12% and the density was found to be around 118 lb/ft^3.

(a)

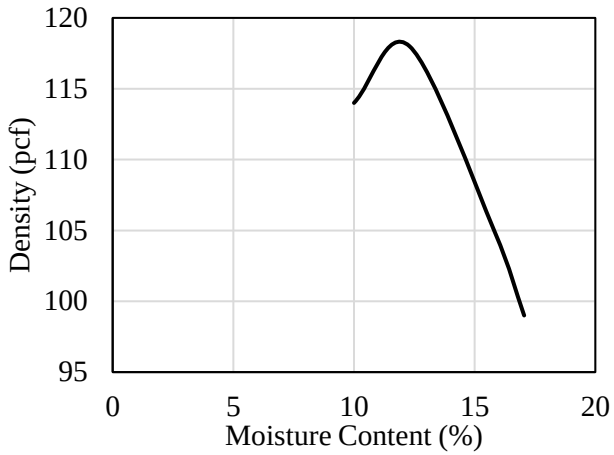

(b)

FIGURE 120 Optimum moisture content of soil near MP 140.6

Remarks

Based on the laboratory tests performed on the field-collected samples, the followings remarks can be made:

1) IDT test was conducted on the field collected AC sample. A good agreement was observed between the field sensor obtained AC creep compliance and dynamic modulus with IDT tested cored specimen.
2) TSRST test on the field cored specimen showed that delamination occurs first than cracking and it also matches with the field observation.
3) In two years, from 2016 to 2018, the coefficient of permeability of the AC samples increased from 135×10^{-5} cm/sec to around 160×10^{-5} cm/sec. The increase in permeability may be due to the damage of the AC layer, such as aging.
4) Rheological analysis of unaged and field aged extracted binder showed that within 4 years the asphalt binder has aged significantly, and crossover frequency and complex modulus had reduced by 2330 and 15 times for the aged binder.

5) Comparing the relaxation modulus for binder and AC, it was observed that scale difference changed the instantaneous modulus by 10^5 fold and relaxation time by 10 fold.
6) Soil test was conducted on the samples collected near MP 141, 140.9 and 140.6. Soil near MP 141 was A-2-4 soil, while soil near MP 140.6 and 140.9 was either A-2-6 or A-6 soil (low plasticity clay according to USGS).

THIS PAGE LEFT BLANK INTENTIONALLY

CONCLUSIONS AND RECOMMENDATIONS

CONCLUSIONS

The main goal of the I-40 instrumentation section was to observe and find a trend in the variation of the pavement performance through embedded sensors. To accomplish this, an instrumentation section was constructed during Phase I of the study with an array of sensors at I-40 near Albuquerque, New Mexico. Pavement performance data were continuously collected during Phase II of the study under traffic and controlled non-destructive FWD test. Based on the field sensor data available so far, these following conclusions can be made:

1) From the embedded strain gage data, it was observed that immediately after the construction, strain values were higher at the bottom of the AC layer and after that, with time, the values started to decrease. The reason for the decrease in AC layer response is mainly due to the damage.
2) With the continuous FWD test performed on the instrumentation section, it was possible to identify the extent of damage in the AC layer. It was found that driving lane AC layer has damaged 11% so far due to the traffic and environmental factors.
3) Combining WIM data, sensor data and FWD test data it was found that around 45% of the total damage in the AC layer was caused due to the class 9 vehicle alone.
4) Although distress, such as cracking, was observed in the passing lane and shoulders but no visible distress was observed in the driving lane. Upon collection of the cores, delamination between the AC lifts was observed in the driving lane. From the analysis of embedded sensor data and FWD deflection basin, it was found that delamination between the AC lifts may have first taken place in the summer of 2015, three years after construction.
5) Pavement response frequency content from FWD test load and actual traffic conditions were compared with the frequency from the ME design software. It was observed that ME design always overpredicts the DF value, which means, ME design overpredicts the dynamic modulus value during the ME analysis.
6) AC viscoelastic properties were obtained directly from the field sensor data. Field sensor obtained dynamic modulus were compared with the dynamic modulus from the IDT test in the laboratory. A good agreement was observed between the field sensor obtained AC creep compliance and dynamic modulus with laboratory IDT tested specimen.
7) FWD modulus was incorporated in the ME design. AC damaged modulus were incorporated as level 1 input while moduli of the unbound layers were given input as level 2. A significant difference was observed between the ME default analysis result with laboratory test input and input from the in-situ NDT FWD test.
8) Damage in the base/subbase accumulated at a rate of 0.63% per year and in the subgrade the damage accumulation rate was around 1.33% per year due to traffic. It suggests that subgrade is taking more damage compared to the base and subbase layer.
9) Rheological analysis of unaged and field aged extracted binder showed that within 4 years the asphalt binder has aged significantly; and complex modulus had reduced by 15 times for the aged binder.

RECOMMENDATIONS FOR FUTURE STUDIES

Based on this study, the following recommendations can be made for future studies:

1) *Continue collecting the stress-strain data from the embedded sensors under moving loads.* From Phase I and Phase II study it was observed that stress-strain and loading frequencies of different layers are changing over time. It was also observed that there is a significant discrepancy among these field sensors obtained data and AASHTOWare ME predicted values. These stress-strain and loading frequency values show variation due to the damage in the pavement layers. Although no significant distresses such as rutting, fatigue or transverse cracking has been observed at the driving lane during the Phase I or Phase II, it is expected that with time these distresses will propagate at the driving lane. Therefore, it is important to observe how the pavement response (stress-strain and loading frequency of different layers) changes not only under aging but also under various distresses.

2) *Perform Non-destructive testing.* Continue performing FWD test on the instrumentation section to observe the changes in layer moduli and stress-strain data. FWD test data can be used to develop field dynamic modulus and pavement performance curve to quantify damage until the distresses show up in the driving lane, which can be valuable to develop a schedule of rehabilitation for flexible pavement across New Mexico.

3) *Calibrate distress models.* As mentioned earlier, AASHTOWare ME distress models are calibrated with the nationally obtained LTPP data. It is important to calibrate these models for the material and climatic condition of New Mexico. One of the tasks of Phase 2 was to calibrate rutting and thermal transverse cracks models of AASHTOWare ME. However, until now in Phase II, no significant distresses were observed in the driving lane. Recently, some distresses have started to appear on passing lane but that is not enough data to perform a calibration of the distress models. Therefore, it is important to continue observing/documenting these distress patterns over the next few years to have sufficient data to perform a meaningful distress model calibration.

4) *Continue collecting weather data.* Weather data from the weather station and temperature data from the temperature probes inside AC can be used to understand aging, low temperature cracking and temperature gradient change. This information can be used for another separate research or to accomplish other tasks of this project.

5) *Continue collecting WIM data.* WIM data analysis has shown that the ME default distribution factors are different from the field observed values. For accurate Pavement ME analysis, it is important to have the correct traffic distribution factors. Furthermore, analysis of WIM data is also required to determine the damage progression of AC layer due to traffic.

REFERENCES

1. Witczak, M. W., D. Andrei, and W. N. Houston. Resilient modulus as function of soil moisture--summary of predictive models. *Development of the 2002 guide for the development of new and rehabilitated pavement structures, NCHRP*, 2000, pp. 1–37.
2. Larson, G., and B. J. Dempsey. *Enhanced integrated climatic model Version 2.0*. 1997.
3. Lytton, R. L., D. E. Pufahl, C. H. Michalak, H. S. Liang, and B. J. Dempsey. An integrated model of the climatic effects on pavements. 1993.
4. Dempsey, B. J., W. A. Herlache, and A. J. Patel. *Climatic-materials-structural pavement analysis program*. 1986.
5. ARA Inc. Guide for the mechanistic-empirical design of new and rehabilitated pavement structures. *Final report, NCHRP Project 1-37A*, 2007.
6. McCartney, J. S., R. P. Selvam, J. King, and A. Khosravi. *Evaluation of the enhanced integrated climatic model for the Arkansas State Highway and Transportation Department*. 2010.
7. Liu, S. J., and R. L. Lytton. *Environmental Effects on Pavement Drainage, Volume IV*. 1985.
8. Dempsey, B. J., and Q. L. Robnett. Influence of precipitation, joints, and sealing on pavement drainage. *Transportation Research Record*, No. 705, 1979.
9. Fredlund, D. G., and A. Xing. Equations for the soil-water characteristic curve. *Canadian Geotechnical Journal*, Vol. 31, No. 4, 1994, pp. 521–532.
10. Witczak, M. W., D. Andrei, and W. N. Houston. Resilient modulus as function of soil moisture. *Development of the 2002 Guide for the Development of New and Rehabilitated Pavement Structures, NCHRP 1-37 A, Tech. Report (Seasonal 1)*, 2000.
11. Huang, Y. H. Pavement analysis and design. 1993.
12. Al-Qadi, I. L., W. Xie, and M. A. Elseifi. Frequency determination from vehicular loading time pulse to predict appropriate complex modulus in MEPDG. *Asphalt Paving Technology-Proceedings*, Vol. 77, 2008, p. 739.
13. Ulloa, A., E. Y. Hajj, R. V Siddharthan, and P. E. Sebaaly. Equivalent loading frequencies for dynamic analysis of asphalt pavements. *Journal of Materials in Civil Engineering*, Vol. 25, No. 9, 2012, pp. 1162–1170.
14. Lau, C. L., T. Scullion, and P. Chan. Modeling of ground-penetrating radar wave propagation in pavement systems. *Transportation Research Record*, Vol. 1355, 1992, pp. 99–107.
15. Mounier, D., H. Di Benedetto, and C. Sauzéat. Determination of bituminous mixtures linear properties using ultrasonic wave propagation. *Construction and Building Materials*, Vol. 36, 2012, pp. 638–647.
16. Jones, R. Surface wave technique for measuring the elastic properties and thickness of roads: Theoretical development. *British Journal of Applied Physics*, Vol. 13, No. 1, 1962, p. 21.
17. Heisey, J. S., I. I. Stokoe, A. H. Meyer, and others. Moduli of pavement systems from spectral analysis of surface waves. *Transportation research record*, No. 852, 1982.
18. Nazarian, S., I. I. Stokoe, and H. Kenneth. Use of surface waves in pavement evaluation. *Transportation research record*, No. 1070, 1986.
19. Ryden, N., and M. A. Mooney. Analysis of surface waves from the light weight deflectometer. *Soil Dynamics and Earthquake Engineering*, Vol. 29, No. 7, 2009, pp. 1134–

1142.
20. Pellinen, T. K., M. W. Witczak, and R. F. Bonaquist. Asphalt mix master curve construction using sigmoidal fitting function with non-linear least squares optimization. In *Recent advances in materials characterization and modeling of pavement systems*, pp. 83–101.
21. AASHTO. Guide for Mechanistic-Emperical Design of New and Rehabilitated Pavement Structures. Vol. NCHRP proj, No. Washington, DC: American Association of State Highway and Transportation Officials, 2004, p. 85.
22. Predictions, F. T. *Adjustment Factors for Asphalt Pavement. Publication No*. 2000.
23. Roberts, F. L., P. S. Kandhal, E. R. Brown, D.-Y. Lee, and T. W. Kennedy. Hot mix asphalt materials, mixture design and construction. 1991.
24. Timm, D. H., and A. L. Priest. Material Properties of the 2003 Test Track Structural Study. 2006.
25. Von Quintus, H. L., C. Rao, L. H. Irwin, and others. *Long-Term Pavement Performance Program determination of in-place elastic layer modulus: backcalculation methodology and procedures.* 2015.
26. Von Quintus, H., and B. Killingsworth. *Analyses Relating to Pavement Material Characterizations and Their Effects*..... McLean, VA United States, 1998.
27. Ayyala, D., H. Lee, H. L. Von Quintus, and others. *Characterizing Existing Asphalt Concrete Layer Damage for Mechanistic Pavement Rehabilitation Design*. 2018.
28. Schafer, R. W. What is a Savitzky-Golay filter?[lecture notes]. *IEEE Signal processing magazine*, Vol. 28, No. 4, 2011, pp. 111–117.
29. Uzan, J. Viscoelastic--viscoplastic model with damage for asphalt concrete. *Journal of materials in civil engineering*, Vol. 17, No. 5, 2005, pp. 528–534.
30. Tashman, L., E. Masad, D. Little, and H. Zbib. A microstructure-based viscoplastic model for asphalt concrete. *International Journal of Plasticity*, Vol. 21, No. 9, 2005, pp. 1659–1685.
31. Al-Qadi, I. L., P. J. Yoo, M. A. Elseifi, and S. Nelson. Creep behavior of hot-mix asphalt due to heavy vehicular tire loading. *Journal of engineering mechanics*, Vol. 135, No. 11, 2009, pp. 1265–1273.
32. Lee, H.-J., and Y. R. Kim. Viscoelastic constitutive model for asphalt concrete under cyclic loading. *Journal of engineering mechanics*, Vol. 124, No. 1, 1998, pp. 32–40.
33. Elseifi, M. A., I. L. Al-Qadi, and P. J. Yoo. Viscoelastic modeling and field validation of flexible pavements. *Journal of engineering mechanics*, Vol. 132, No. 2, 2006, pp. 172–178.
34. Al-Qadi, I. L., A. Loulizi, M. Elseifi, and S. Lahouar. The Virginia Smart Road: The impact of pavement instrumentation on understanding pavement performance. *Journal of the Association of Asphalt Paving Technologists*, Vol. 73, 2004, pp. 427–466.
35. Huang, Y. H. Pavement analysis and design. 2004.
36. Mun, S., and G. Zi. Modeling the viscoelastic function of asphalt concrete using a spectrum method. *Mechanics of Time-Dependent Materials*, Vol. 14, No. 2, 2010, pp. 191–202.
37. Aragão, F. T. S., Y.-R. Kim, J. Lee, and D. H. Allen. Micromechanical model for heterogeneous asphalt concrete mixtures subjected to fracture failure. *Journal of Materials in Civil Engineering*, Vol. 23, No. 1, 2010, pp. 30–38.
38. Faisal, H. M., Z. H. Khan, and R. Tarefder. Modeling Nanoscale Rheological and Mechanical Properties of Thin Film Asphalt Binder. 2016.
39. Allen, R. G., D. N. Little, A. Bhasin, and R. L. Lytton. Identification of the Composite

Relaxation Modulus of Asphalt Binder Using AFM Nanoindentation. *Journal of Materials in Civil Engineering*, Vol. 25, No. 4, 2013, pp. 530–539.
40. Faisal, H. M., and R. A. Tarefder. Modeling nanoindentation creep behavior of asphalt binder. *Advances in Civil Engineering Materials*, Vol. 2, No. 1, 2013, pp. 418–440.
41. Islam, M. R., and R. A. Tarefder. Measuring thermal effect in the structural response of flexible pavement based on field instrumentation. *International Journal of Pavement Research and Technology*, Vol. 6, No. 4, 2013, pp. 274–279.
42. AASHTO Standard TP62. Standard method of test for determining the dynamic modulus and flow number for hot mix asphalt (HMA). *American Association of State Highway and Transportation Officials, Washington, DC*, 2011.
43. Lee, W. C. Y. Estimate of local average power of a mobile radio signal. *IEEE Transactions on Vehicular Technology*, Vol. 34, No. 1, 1985, pp. 22–27.
44. Shafiee, M. H., A. Asefzadeh, L. Hashemian, and A. Bayat. Analysis of Loading Frequency in Flexible Pavement Using Fast Fourier Transform. *International Journal of Pavement Research and Technology*, Vol. 8, No. 6, 2015, pp. 403–409.
45. Elseifi, M. a., I. L. Al-Qadi, and P. J. Yoo. Viscoelastic Modeling and Field Validation of Flexible Pavements. *Journal of Engineering Mechanics*, Vol. 132, No. 2, 2006, pp. 172–178.
46. Appea, A. K. *Validation of FWD testing results at the Virginia Smart Road: Theoretically and by instrument responses*. Virginia Tech, 2003.
47. Chatti, K., Y. Ji, and R. Harichandran. Dynamic Time Domain Backcalculation of Layer Moduli, Damping, and Thicknesses in Flexible Pavements. *Transportation Research Record*, Vol. 1869, No. 1, 2004, pp. 106–116.
48. AASHTO, T. Standard method of test for determining the resilient modulus of soils and aggregate materials. *American Association of State Highway and Transportation Officials, Washington*, Vol. 99, 2003.
49. Rahim, A., and K. P. George. Falling weight deflectometer for estimating subgrade elastic moduli. *Journal of Transportation Engineering*, Vol. 129, No. 1, 2003, pp. 100–107.
50. Fontul, S. Structural Evaluation of Flexible Pavements using Non Destructive Tests. 2009.
51. Xu, B. *Assessing pavement layer condition using FWD deflection data*. North Carolina State University, 2001.
52. Salour, F., and S. Erlingsson. Moisture-sensitive and stress-dependent behavior of unbound pavement materials from in situ falling weight deflectometer tests. *Transportation Research Record: Journal of the Transportation Research Board*, No. 2335, 2013, pp. 121–129.
53. Varma, S., and M. Emin Kutay. Backcalculation of viscoelastic and nonlinear flexible pavement layer properties from falling weight deflections. *International Journal of Pavement Engineering*, Vol. 17, No. 5, 2016, pp. 388–402.
54. Nazzal, M. D., and L. N. Mohammad. Estimation of resilient modulus of subgrade soils using falling weight deflectometer. *Transportation Research Record*, Vol. 2186, No. 1, 2010, pp. 1–10.
55. Von Quintus, H., and B. Killingsworth. *Design pamphlet for the determination of design subgrade in support of the 1993 AASHTO guide for the design of pavement structures*. 1997.
56. Al-Qadi, I. I. L., A. Loulizi, M. Elseifi, and S. Lahouar. The Virginia SMART ROAD: the impact of pavement instrumentation on understanding pavement performance (with discussion). *Journal of the Association of …*, Vol. 73, 2004, pp. 427–465.
57. Baker, H. B., M. R. Buth, and D. A. Van Deusen. *Minnesota road research project: load*

response instrumentation installation and testing procedures. Report MN/PR-94/01, Physical Research, Office of Materials Research and Engineering, Minnesota Department of Transportation, 1994.
58. Al-Qadi, I., and A. Appea. Eight-year field performance of secondary road incorporating geosynthetics at subgrade-base interface. *Transportation Research Record: Journal of the Transportation Research Board*, No. 1849, 2003, pp. 212–220.
59. Donovan, P., and E. Tutumluer. Falling weight deflectometer testing to determine relative damage in asphalt pavement unbound aggregate layers. *Transportation Research Record: Journal of the Transportation Research Board*, No. 2104, 2009, pp. 12–23.
60. Hicks, R. G., and C. L. Monismith. Factors influencing the resilient response of granular materials. *Highway research record*, No. 345, 1971.
61. Uzan, J. Characterization of granular material. *Transportation research record*, Vol. 1022, No. 1, 1985, pp. 52–59.
62. Witczak, M. W., and J. Uzan. The universal airport pavement design system. *Report I of V: granular material characterization, Department of Civil Engineering, University of Maryland, College Park, MD*, 1988.
63. Nicks, J. E., T. Gebrenegus, M. T. Adams, and others. *Strength characterization of open-graded aggregates for structural backfills*. 2015.
64. Pierce, L. M., J. E. Bruinsma, K. D. Smith, M. J. Wade, K. Chatti, and J. M. Vandenbossche. *Using Falling Weight Deflectometer Data with Mechanistic-Empirical Design and Analysis, Volume III: Guidelines for Deflection Testing, Analysis, and Interpretation*. 2017.
65. Islam, M. *Thermal fatigue damage of asphalt pavement*. University of New Mexico, 2015.
66. Tarefder, R. A., and M. R. Islam. *Study and Evaluation of Materials Response in Hot Mix Asphalt Based on Field Instrumentation Phase I: Final report*. Albuquerque, 2015.
67. Islam, M. R., U. A. Mannan, A. Rahman, and R. A. Tarefder. Simplified Thermal Stress Model to Predict Low Temperature Cracks in Flexible Pavement. 2014.
68. Bazlamit, S. M., and F. Reza. Changes in asphalt pavement friction components and adjustment of skid number for temperature. *Journal of Transportation Engineering*, Vol. 131, No. 6, 2005, pp. 470–476.
69. Islam, M. R., S. Ahsan, and R. A. Tarefder. Modeling Temperature Profile of Hot-Mix Asphalt in Flexible Pavement. *International Journal of Pavement Research and Technology*, Vol. 8, No. 1, 2015, p. 47.
70. Bosscher, P., H. Bahia, S. Thomas, and J. Russell. Relationship between pavement temperature and weather data: Wisconsin field study to verify superpave algorithm. *Transportation research record: journal of the transportation research board*, No. 1609, 1998, pp. 1–11.
71. Diefenderfer, B. K. *Moisture content determination and temperature profile modeling of flexible pavement structures*. Virginia Polytechnic Institute and State University, 2002.
72. Diefenderfer, B. K., I. L. Al-Qadi, and S. D. Diefenderfer. Model to predict pavement temperature profile: development and validation. *Journal of Transportation Engineering*, Vol. 132, No. 2, 2006, pp. 162–167.
73. Khan, Z., M. R. Islam, and R. A. Tarefder. Determining the Average Asphalt Temperature of Flexible Pavement. 2016.
74. Solaimanian, M., and T. W. Kennedy. Predicting maximum pavement surface temperature using maximum air temperature and hourly solar radiation. *Transportation Research*

Record, No. 1417, 1993.
75. Hermansson, A. Mathematical model for calculating pavement temperatures: comparisons of calculated and measured temperatures. *Transportation Research Record*, Vol. 80, 2001, pp. 180–188.
76. Wang, D. Analytical approach to predict temperature profile in a multilayered pavement system based on measured surface temperature data. *Journal of Transportation Engineering*, Vol. 138, No. 5, 2011, pp. 674–679.
77. Ghasemi, A., and S. Zahediasl. Normality tests for statistical analysis: a guide for non-statisticians. *International journal of endocrinology and metabolism*, Vol. 10, No. 2, 2012, p. 486.
78. Pallant, J. *SPSS Survival Manual: A Step by Step Guide to Data Analysis Using SPSS for Windows (Versions 10 and 11): SPSS Student Version 11.0 for Windows*. Open University Press Milton Keynes, UK, USA, 2001.
79. Altman, D. G., and J. M. Bland. Statistics notes: the normal distribution. *Bmj*, Vol. 310, No. 6975, 1995, p. 298.
80. AASHTO T322-07. Standard Test Method for Determining the Creep Compliance and Strength of Hot-Mix Asphalt (HMA) Using the Indirect Tensile Test Device. *American Association of State Highway and Transportation Officials*, 2007.
81. AASHTO T342. Determining dynamic modulus of hot-mix asphalt concrete mixtures. *American Association of State Highway and Transportation Officials*, 2011.
82. Kim, Y. R., Y. Seo, M. King, and M. Momen. Dynamic modulus testing of asphalt concrete in indirect tension mode. *Transportation Research Record*, Vol. 1891, No. 1, 2004, pp. 163–173.
83. Lee, H. S., and J. Kim. Determination of viscoelastic Poisson's ratio and creep compliance from the indirect tension test. *Journal of Materials in Civil Engineering*, Vol. 21, No. 8, 2009, pp. 416–425.
84. Khan, Z. H., and R. A. Tarefder. A procedure to convert field sensor data for finite element model inputs and its validation. *Construction and Building Materials*, Vol. 212, 2019, pp. 442–455.
85. Chehab, G. R., and Y. R. Kim. Viscoelastoplastic continuum damage model application to thermal cracking of asphalt concrete. *Journal of materials in civil engineering*, Vol. 17, No. 4, 2005, pp. 384–392.
86. Zubeck, H. K., and T. S. Vinson. Prediction of low-temperature cracking of asphalt concrete mixtures with thermal stress restrained specimen test results. *Transportation Research Record*, Vol. 1545, No. 1, 1996, pp. 50–58.
87. Lottman, R. P. Predicting moisture-induced damage to asphaltic concrete field evaluation. *NCHRP report*, No. 246, 1982.
88. Chen, J.-S., K.-Y. Lin, and S.-Y. Young. Effects of crack width and permeability on moisture-induced damage of pavements. *Journal of Materials in Civil Engineering*, Vol. 16, No. 3, 2004, pp. 276–282.
89. Sengoz, B., and E. Agar. Effect of asphalt film thickness on the moisture sensitivity characteristics of hot-mix asphalt. *Building and environment*, Vol. 42, No. 10, 2007, pp. 3621–3628.
90. ASTM D2172. Standard test methods for quantitative extraction of bitumen from bituminous paving mixtures.
91. ASTM 5404. Standard practice for recovery of asphalt from solution using the rotary

evaporator. 2012.
92. AASHTO 7175. Standard method of test for determining the rheological properties of asphalt binder using a dynamic shear rheometer (DSR). *American Association of state and highway transportation officials*, 2012.
93. ASTM D6913. *Standard test methods for particle-size distribution (gradation) of soils using sieve analysis*. ASTM International, 2017.
94. ASTM D4318-17. *Standard test methods for liquid limit, plastic limit, and plasticity index of soils*. ASTM international, 2010.
95. ASTM D1557-12. *Standard Test Methods for Laboratory Compaction Characteristics of Soil Using Modified Effort (56,000 Ft-lbf/ft3 (2,700 KN-m/m3)) 1*. ASTM international, 2015.

New Mexico Department of Transportation
RESEARCH BUREAU
7500B Pan American Freeway NE
PO Box 94690
Albuquerque, NM 87199-4690
Tel: (505) 841-9145